Luminescence of droplet-etched GaAs quantum dots at varied temperature and in electric and magnetic fields

This dissertation is submitted for the degree of
Doktor der Naturwissenschaften
at the Faculty of Mathematics, Informatics and Natural Sciences
Department of Physics of Universität Hamburg

submitted by
Leonardo Ranasinghe Arachchige

9 August 2022

Gutachter der Dissertation:	Prof. Dr. Wolfgang Hansen Dr. Christian Heyn
Vorgeschlagene Mitglieder der Prüfungskommission:	Prof. Dr. Wolfgang Hansen Dr. Christian Heyn Prof. Dr. Gabriel Bester Prof. Dr. Wolfgang Parak Prof. Dr. Dieter Horns
Datum der Disputation:	18.07.2022
Vorsitzender des Prüfungsausschusses:	Prof. Dr. Dieter Horns
Vorsitzender Fach-Promotionsausschusses Physik:	Prof. Dr. Wolfgang Parak
Leiter des Fachbereichs Physik:	Prof. Dr. Günter Sigl
Dekan der MIN-Fakultät:	Prof. Dr. Heinrich Graener

Declaration on oath

I hereby declare, on oath, that I have written the present dissertation by my own and have not used other than the acknowledged resources and aids.

Eidesstattliche Versicherung

Hiermit versichere ich an Eides statt, die vorliegende Dissertationsschrift selbst verfasst und keine anderen als die angegebenen Hilfsmittel und Quellen benutzt zu haben.

Hamburg, 9 August 2022 Signature/Unterschrift 

Abstract

Semiconductor quantum dots (QDs) are important building blocks for a range of applications, from QD based lasers to quantum cryptography and quantum information processing, to further optoelectronic applications. QDs suitable for these purposes need to fulfil highly demanding criteria in terms of optical quality and versatility. Local droplet etching (LDE) has established as an epitaxial growth method to obtain low-density (about $10^7\,\mathrm{cm}^{-2}$), strain-free, pure and highly uniform QDs which can meet these standards. In the LDE method, which is fully compatible with the conventional molecular beam epitaxy, Al droplets are deposited on an AlGaAs or AlAs surface and perform self-assembled drilling of nanoholes with shape and size that are tunable through the process parameters. The nanoholes can then be filled with GaAs and capped with AlGaAs to form GaAs QDs. The LDE QDs have sharp excitonic lines with linewidth down to 25 µeV, precisely controllable emission wavelength, neutral exciton fine-structure splitting below 5 µeV and a nearly perfect single photon emission, with a minimum of the second order correlation function of 0.01.

The optical properties of the LDE QDs have mostly been studied at liquid helium temperatures. However, for many QD based devices, operation in ambient condition is crucial. Hence, an analysis of the behaviour of the QD photoluminescence (PL) emission at and close to room temperature is here provided. It is shown that the observation of the optical emission from the QDs is hindered by the emission from the GaAs substrate and that a significant loss of intensity by more than four orders of magnitude is observed compared to low temperature luminescence. However, using an optimised sample with an AlGaAs barrier layer thicker than the penetration depth of the photons from a 532 nm green laser, leads to clear QD peaks at high temperatures. Furthermore, when the AlGaAs layer is thin, QD emission at room temperature can still be observed if the QD is excited with a 405 nm blue laser, since it has a reduced optical penetration depth. A model and a fit to the experimental results is presented to understand possible reasons for the intensity loss. This analysis identifies as the main

causes of intensity loss the exciton dissociation in the barrier at $T < 100\,\mathrm{K}$ and the thermal escape of bound excitons from the QD ground-state at $T > 160\,\mathrm{K}$.

Besides the impact of the rise in temperature, this work also covers the influence of applying external electric and magnetic fields on the LDE QDs. In particular, QDs with a cone-shell shape, obtained by drilling nanoholes with Al droplets into AlGaAs instead of AlAs, are here considered, as their peculiar shape makes them highly versatile structures for wavefunction manipulation. In fact, the application of an electric field along the QD growth direction is shown to cause a strong separation between charge carriers, which leads the probability distribution of either the electrons or the holes to take a ring shape, whilst the other charge carrier remains as a dot. The dot to ring transformation can be precisely controlled by the applied gate voltage and has various consequences. One of these, which is here studied both with computations and experiments, is the non-parabolic Stark-shift with a regime of approximately constant exciton emission energy. Furthermore, numerical simulations predict that the exciton recombination lifetime can be increased from nanoseconds up to seconds, as a consequence of the strong charge carrier separation and reduced Coulomb interaction at strong electric fields. The lifetime elongation suggests cone-shell QDs for applications as light storage in the field of quantum information technology.

The formation of quantum rings with adjustable diameter by means of an electric field makes cone-shell QDs interesting also for magnetic field dependent PL measurements. Here, predictions of the behaviour of QD PL under the influence of an external vertical magnetic field are drawn through simulations. The computational studies on the excitonic PL emission predict the possibility of observing Ahronov-Bohm (AB) states in the spectra with the application of a magnetic field of less than 1 T when applying an electric field of $12\,\mathrm{kV/cm}$. However, due to selection rules, only the vanishing of the PL emission and, under certain conditions, its recurrence are expected to be experimentally observed. It is thus also shown that, through the combined effect of the electric and magnetic fields, it is possible to form a hybrid system between a quantum ring and a QD, in which, as a consequence of the varying ground-state magnetic quantum number as function of the magnetic field, the magnetic field can be used to switch on and off the luminescence.

Inhaltsangabe

Halbleiter-Quantenpunkte (quantum dots, QDs) sind wichtige Bausteine für eine Reihe von Anwendungen, von quantenpunktbasierten Lasern über Quantenkryptographie und Quanteninformationsverarbeitung bis hin zu weiteren optoelektronischen Anwendungen. QDs, die für diese Zwecke geeignet sind, müssen sehr anspruchsvolle Kriterien in Bezug auf ihre optische Qualität und Vielseitigkeit erfüllen. Das lokale Tröpfchenätzen hat sich als epitaktische Wachstumsmethode etabliert, mit der sich QDs mit geringer Dichte (etwa $10^7\,\mathrm{cm}^{-2}$), verspannungsfrei, rein und mit abstimmbarer Form herstellen lassen, die diese Anforderungen erfüllen. Bei der lokalen Tröpfchenätzmethode, die mit der herkömmlichen Molekularstrahlepitaxie voll kompatibel ist, werden Al-Tropfen auf einer AlGaAs- oder AlAs-Oberfläche abgeschieden und bohren selbstorganisiert Nanolöcher, deren Form und Größe über die Prozessparameter einstellbar sind. Die Nanolöcher können dann mit GaAs gefüllt und mit AlGaAs abgedeckt werden, um GaAs-QDs zu bilden. Die durch lokales Tröpfchenätzen erhaltenen QDs haben scharfe exzitonische Linien mit einer Linienbreite von weniger als 25 µeV, eine präzise steuerbare Emissionswellenlänge, eine neutrale Exzitonen-Feinstrukturaufspaltung unter 5 µeV und eine nahezu perfekte Einzelphotonenemission mit einem Minimum der Korrelationsfunktion zweiter Ordnung von 0,01.

Die optischen Eigenschaften von QDs, die durch das lokale Tröpfchenätzen erzeugt werden, wurden hauptsächlich bei Temperaturen von flüssigem Helium untersucht. Für viele auf QDs basierende Anwendungen ist jedoch der Betrieb bei Raumtemperatur entscheidend. Daher wird hier eine Analyse des Verhaltens der Photolumineszenzemission von QDs bei und in der Nähe von Raumtemperatur durchgeführt. Es wird gezeigt, dass die Beobachtung der optischen Emission der QDs durch die Emission des GaAs-Substrats behindert wird und dass ein erheblicher Intensitätsverlust von mehr als vier Größenordnungen im Vergleich zur Lumineszenz bei niedrigen Temperaturen zu beobachten ist. Die Verwendung einer optimierten Probe mit einer AlGaAs-Sperrschicht, die

dicker ist als die Eindringtiefe der Photonen eines grünen 532 nm-Lasers, führt jedoch zu deutlichen QD-Linien auch bei hohen Temperaturen. Darüber hinaus kann bei einer dünnen AlGaAs-Schicht eine QD-Emission bei Raumtemperatur beobachtet werden, wenn der QD mit einem blauen 405 nm-Laser angeregt wird, da dieser eine geringere optische Eindringtiefe hat. Es wird ein Modell und eine Anpassung an die experimentellen Ergebnisse vorgestellt, um mögliche Gründe für den Intensitätsverlust zu verstehen. Diese Analyse identifiziert als Hauptursachen für den Intensitätsverlust die Dissoziation von Exzitonen in der Barriere bei $T < 100\,\mathrm{K}$ und das thermische Entweichen von gebundenen Exzitonen aus dem Grundzustand des QD bei $T > 160\,\mathrm{K}$.

Neben der Auswirkung des Temperaturanstiegs wird in dieser Arbeit auch der Einfluss der Anwendung externer elektrischer und magnetischer Felder auf die Tröpfchengeätzten -QD behandelt. Insbesondere werden hier QDs mit einer Kegelschalenform betrachtet, die durch Bohren von Nanolöchern mit Al-Tropfen in AlGaAs anstelle von AlAs erhalten wurden, da ihre besondere Form sie zu äußerst vielseitigen Strukturen für die Wellenfunktionsmanipulation macht. Es wird gezeigt, dass das Anlegen eines elektrischen Feldes entlang der QD-Wachstumsrichtung eine starke Trennung zwischen den Ladungsträgern bewirkt, was dazu führt, dass die Wahrscheinlichkeitsverteilung entweder der Elektronen oder der Löcher eine Ringform annimmt, während der andere Ladungsträger als Punkt bestehen bleibt. Die Umwandlung vom Punkt zum Ring kann durch die angelegte Gatespannung genau gesteuert werden und hat verschiedene Konsequenzen. Eine davon, die hier sowohl mit Berechnungen als auch mit Experimenten untersucht wird, ist die nichtparabolische Stark-Verschiebung mit einem Regime annähernd konstanter Exzitonen-Emissionsenergie. Darüber hinaus sagen numerische Simulationen voraus, dass die Rekombinationslebensdauer der Exzitonen von Nanosekunden bis zu Sekunden erhöht werden kann, was auf die starke Ladungsträgertrennung und die reduzierte Coulomb-Wechselwirkung bei starken elektrischen Feldern zurückzuführen ist. Durch die Verlängerung der Lebensdauer können die Kegelschalen-QDs möglicherweise als Lichtspeicher in der Quanteninformationstechnologie eingesetzt werden.

Die Bildung von Quantenringen mit einstellbarem Durchmesser durch ein elektrisches Feld macht Kegelschalen-QDs auch für magnetfeldabhängige Photolumineszenzmessungen interessant. Hier werden Vorhersagen über das Verhalten von

QD PL unter dem Einfluss eines externen vertikalen Magnetfeldes durch Simulationen getroffen. Die rechnerischen Untersuchungen zur exzitonischen Photolumineszenzemission sagen die Möglichkeit voraus, Ahronov-Bohm-Zustände in den Spektren bei der Anwendung eines Magnetfeldes von weniger als 1 T bei einem elektrischen Feld von 12 kV/cm zu beobachten. Aufgrund von Selektionsregeln wird voraussichtlich jedoch nur das Verschwinden der PL-Emission und, unter bestimmten Bedingungen, ihr Wiederauftreten experimentell beobachtet werden. Es wird also auch gezeigt, dass durch die kombinierte Wirkung von elektrischem und magnetischem Feld ein Hybridsystem zwischen einem Quantenring und einem QD gebildet werden kann, in dem als Folge der sich ändernden magnetischen Grundzustandsquantenzahl als Funktion des Magnetfeldes das Magnetfeld zum Ein- und Ausschalten der Lumineszenz genutzt werden kann. Auch dieser Effekt kann sich zum Speichern von Licht in der Quanteninformationstechnologie eignen.

Contents

Chapter 1

Introduction

Semiconductor quantum dots (QDs) are systems with a three dimensional (3D) confinement where the dimensions are in the range of nanometers. The quantum confinement, resulting from the size on each direction being smaller than the de Broglie wavelength of slow electrons, results in unique physical properties, which made QDs a central topic in nanotechnology. In particular, current research interest is mainly driven by QDs optical properties, because of the attractive and broad variety of potential applications, such as low threshold lasing [1], solar cells [2, 3], optical amplifiers [4] and single [5, 6] and entangled photon emission [7, 8] for quantum information processing and quantum cryptography [9, 10].

Research on QDs dates back to the '80s, starting from the pioneering studies of A. Ekimov, who discovered, in 1981, the presence of nanocrystals of CdS, CuBr, CuCl and CdSe in glass matrices. With the help of the theoretician A. Efros, in 1985, Ekimov demonstrated the influence of QDs' size on their optical properties [11]. Independent research was carried also by L. Brus on CdS colloids: by controlling the size of the colloids, he was able to produce nanocrystals with minimum diameter of 4.5 nm and observed them to exhibit largely blue-shifted optical absorption spectra compared to the bulk material [12]. From the discovery of nanocrystals, referred to as quantum dots from 1988, a term coined by M. Reed [13], the scientific community has been widely interested in exploring their physical properties.

Throughout the '90s, the research focus was mainly on electronic properties, such as Coulomb blockade, which can be observed in QDs due to the electrons being strongly confined, thus causing a strong Coulomb repulsion that refrains the addition of further electrons. Many other remarkable results on QD transport properties were achieved by using gate-defined QDs. QDs obtained with this approach are however not functional for optical studies since the confinement of electrons and holes is not simultaneous but rather exclusive,

the confined carrier type depending on the applied voltage that leads to the confinement.

Optical properties were in general difficult to study also with the other techniques available at the time because of the samples' low optical quality. During the '90s, at first, the most common approach to fabricate QDs with simultaneously confined electrons and holes, was by patterning quantum wells, nanometer thick semiconductor sheets, through various lithographic techniques. These include optical lithography, based on ultraviolet optics and on eximer lasers, X-ray lithography and electron beam and ion beam lithography. Lithography allows control of the QDs' spatial arrangements, which makes this technique still attractive. However, the structures' feature sizes and size fluctuations generally exceed desirable values [14]. Moreover, the processes required after lithography, such as etching, are detrimental to the optical quality of QDs. In fact, etching causes damage and charged states at the surface, which in turn causes sidewall depletion, often on large length scales, leading to confinement by electric fields rather than structural confinement, as needed for simultaneous confinement of electrons and holes.

Only when molecular beam epitaxy (MBE) was developed and applied for the fabrication of QDs was it possible to substantially improve and better explore their optical properties. In 1994, the electronic shell-structure of InGaAs QDs was revealed through capacitance and IR spectroscopy [15] and the first single-dot photoluminescence spectra were evidenced from InAs QDs [16]. These first results on single QDs were obtained for dots fabricated by self-assembly mechanism through Stranski-Krastanov (SK) growth mode, which led to improved sample purity and high optical quality. In the same year, natural QDs obtained by local thickness fluctuations at the interface of MBE grown GaAs/AlGaAs quantum wells, were studied through low-temperature near-field spectroscopy [17]. Using a fiber tip placed closed to the sample, excitons were formed and the luminescence arising from their recombination was collected with a lens. A few years later, further studies on natural GaAs QDs, formed in GaAs/AlGaAs quantum wells due to thickness fluctuations, reported direct observation of single localised excitons through photoluminescence [18–21]. Although natural QDs offered the narrowest emission and absorption linewidth achievable at the time [20], they allowed only small confinement energies [22]. Furthermore, all the approaches described, resulted in samples with high QD density and thus spectroscopy of single QDs needed further sample preparation by structuring their surfaces through metallic masks or lithography [23]. A crucial step-forward was obtained in 2004 by optimising the process parameters during and after the SK growth in the MBE, making possible to obtain low-density quantum dots with large confinement energies and light emission in the working range of sensible Si-detectors and Ti:sapphire lasers and thus suitable for coherent optical investigation [22, 24].

From the implementation of self-assembly methods, the major focus of QD research shifted from QDs' electrical properties to their optical properties, because of the wide range of attractive applications and, in the last two decades, considerable effort was put into the optimisation of the fabrication process [25–29]. SK growth is now a well-established method and its success, especially with In(Ga)As QDs, made it the most widely used technique for the production of QDs for device applications [30–32]. SK growth is based on strain induction on lattice mismatched heteroepitaxy. As an example, considering the most common choices of material combinations, InGaAs QDs are grown on GaAs(001) substrate and capped with a GaAs layer. The growth is obtained using InAs, which has a lattice constant about 7% larger than GaAs [33]. The growth starts from a layer-by-layer deposition of In(Ga)As, forming an epitaxial layer referred to as wetting layer (WL). When the WL reaches a critical thickness, the accumulated strain energy in the epilayer due to the mismatch between WL and substrate material, changes the surface morphology to minimise the total layer energy and forms 3D islands. With the correct growth conditions, the islands can result in QDs after being overgrown with GaAs.

Despite having being at the basis of milestone results, both in fundamental and technological areas, SK QDs have various unavoidable limitations and disadvantages: the QDs are connected to each other by the 2D WL; built-in direction-dependent polarisation fields are induced by residual strain [34]; the island shapes, irrespective of the materials, are dependent on the energetically favoured facets and are limited to pyramid and dome-shapes [35]; strong limitations are also present on the QD size [36]; during growth and capping, the QDs are affected by unintentional strain-enhanced intermixing with the surface material [37] and their composition is thus poorly controlled, with up to 80% of substrate material present in the bottom layer of the QDs [38, 39]; the QD surface density and structure are difficult to be manipulated separately, and the emission energy range attainable through SK QDs is constrained by the limited material combinations that can be used [40].

The need for QDs with specific emission energies or optical and structural properties, has driven research on possible optimisations or alternatives to SK growth. Thanks to its great versatility in the QD shape control and the possibility to use materials with the same lattice constants, droplet epitaxy (DE), a strain-free bottom-up fabrication approach, has recently attracted increasing interest. DE can be used to obtain QDs of a large variety of materials but the most common QDs are GaAs QDs in an AlGaAs barrier [41]. Using this as an example, firstly, Ga is deposited on an AlGaAs layer, with metal-stabilised surface. Regardless of the lattice mismatch, further deposition of group III metal adatoms causes the spontaneous formation of Ga droplets in Volmer-Weber growth mode, due to either As desorption or

an excess of deposited metal [42]. Subsequently, at an As pressure about 10 times higher compared to usual GaAs growth, the droplet crystallises at the interface with the substrate. The crystallisation starts from a ring formation at the droplet edge, which increases in size, closes and eventually evolves into a pyramid shaped nanostructure [43]. The nanostructures are then covered by AlGaAs, thus obtaining optically active strain-free QDs. For other group III-V semiconductors, the process is analogous with different temperatures associated with element-dependent diffusivity and binding energies. DE technique has many advantages with respect to SK growth method: the WL can be controlled or completely removed by modifying the surface composition and reconstruction before droplet formation [44]; there is no strain-induced built-in polarisation field; by controlling the process parameters, a large variety of shapes can be obtained, from compact islands to hollow structures, such as single rings and discs; the QD size and aspect ratio can be directly adjusted within a relatively wide range [40]; the material interdiffusion at the interface between QD and barrier is very limited and thus the QDs material composition can be well-controlled and the nanostructures maintain their morphology after capping [45]; QD surface density and structure can be tuned independently; a large variety of semiconductor materials can be used, such as InSb/CdTe [46], In(Ga)As/GaAs [47], GaAs/Si [48], GaSb/GaAs [49] and GaN/AlGaN [50], hence widening the range of possible emission energies.

Despite being able to overcome many of the major issues presented by the SK growth method, DE is not free from drawbacks, which are mainly related to the low temperature used on (001) substrates during the annealing process, when the metal droplets crystallise. Low temperatures, necessary to avoid 2D growth, cause DE QDs to be of poor material and optical quality. The issue can be partially solved by sophisticated in-situ and ex-situ annealing strategies [47, 51, 52] but effects associated with the presence of defects are still an impediment to the use of DE QDs for quantum applications.

These limitations are overcome by a recently developed technique, the local droplet etching (LDE)[53], which leads to highly pure QDs, with excellent optical qualities. The LDE process, similarly to DE, starts from the deposition of droplets onto a III-V semiconductor, usually AlGaAs. A local etching step follows, in which the droplets anneal, at relatively high temperatures and under low group V flux [54], causing the substrate material underneath the droplets to be etched. The droplet material is then removed by spreading over the substrate surface as a 2D layer and nanoholes are formed, surrounded by a ring-shaped crest [55, 56]. QDs are then obtained by filling the nanohole, usually with GaAs, and depositing a layer of the barrier material. The amount of filling material can be easily controlled, directly affecting the QD emission energy. The shape of the QDs can also be

finely manipulated by adjusting the growth parameter before and during the formation of the nanoholes [57]. Furthermore, besides having excellent optical qualities resulting from the high growth temperatures, the strain-free LDE QDs also feature high symmetry since they are constrained into the nanohole, making them attractive sources of entangled photon pairs [58]. The QDs can be also conveniently localised by the hillocks on the capping layer, which can be accentuated by growth and overgrowth conditions. The hillocks can be useful, for example, as markers for the growth of further nanostructures, such as plasmonic nanoantennas [59].

This thesis focuses on the optical properties of LDE QDs with different structural properties and under different external conditions, namely at varying temperatures and under the influence of externally applied electric and magnetic fields. In the next chapter (ch. 2), the characteristics of the MBE and the various growth modes are first outlined, followed by a detailed overview of the LDE method, with a focus on its use for the formation of QDs. In ch. 3, a theoretical background relevant to this work is provided and includes an introduction to confined nanostructures and the basic theory on QD PL and how it is modified by temperature change and application of external electric and magnetic fields. In ch. 4, the experimental and computational methods used are described. The description include sample fabrication, preparation and contacting of the gates, PL set-up, morphological characterisation of the samples and simulation methods. To this follow the results. Firstly, in ch. 5, three types of QD samples are studied at room temperature and the influence of the laser energy is also discussed. Secondly, in ch. 6, the influence of an external electric field applied in the growth direction is studied on QDs with a cone-shell shape (or V shape). Initially, simulation results are given in the single particle frame approximation and under consideration of Coulomb interaction, followed by experimental results for samples with different QD sizes and at different laser powers. Thirdly, in ch. 7, the effect of a magnetic field on QDs with the same cone-shell shape, in conjunction with an electric field, is discussed through simulations, with and without considering Coulomb interaction. In ch. 8, all the results are briefly summarised and possible improvements and suggestions for future work are given.

Chapter 2

Local droplet etching for QD fabrication

The QD samples studied in this work are fabricated by MBE through the local droplet etching (LDE) growth method. In this chapter, the MBE characteristics, operation and growth modes are briefly outlined, followed by an in-depth description of the LDE technique for the fabrication of QDs.

2.1 Molecular beam epitaxy

Various physical vapour deposition methods (PVD) are available for the growth of thin films. Some examples are electron-beam and thermal evaporation processes and sputtering methods, such as AC, DC, magnetron and pulsed laser sputtering. Among the many PVD methods, MBE distinguishes itself for the slow deposition rate in ultra-high-vacuum (UHV), which leads to good thickness control, sharp monoatomic interfaces and negligible dopant distribution. Furthermore, the growth rate is kinetically controlled and it is possible to have in-situ cleaning by low-energy sputtering with ion beam of an inert gas or by heating. Additionally, MBE allows a multitude of in-situ control and analysis methods, such as monitoring the growth with reflection high-energy electron diffraction (RHEED). In this section, these characteristics of the MBE are discussed in details.

The MBE is a technique that enables the epitaxial growth of thin layers of crystalline materials on a heated surface. The growth process takes place in the growth chamber in high or UHV condition (10^{-8}–10^{-12} Torr). Because of the very low pressure, the materials inside the chamber have a mean free path larger than the size of the substrate chamber itself, leading to the arrival of the new material without interaction inside the vacuum. Furthermore, the low pressure in combination with high process temperatures and thus low sticking coefficient of critical gases, provides the highest achievable purity of the grown layer. The

MBE growth chamber (fig. 2.1) can be divided into 3 sections, in which different physical phenomena occur: in the first, molecular beams are generated by evaporation of high purity materials inside individual effusion cells; in the second section, the molecular beams of the evaporated materials travel towards a heated substrate; in the third and last section, the beam reaches the substrate and, once on it, the atoms or molecules move until an atomic site is found for chemical bonding. The flux of atoms or molecules and, consequently, the growth rate, can be kinetically controlled by precisely adjusting the temperature of each effusion cell and the beam can also be interrupted using cell shutters. Due to the different temperatures of the substrate atoms and the incident new ones, the MBE growth occurs in thermodynamic non-equilibrium conditions and hence, it is mainly determined by the kinetic processes resulting from the reactions between the atoms of the beam and the surface. Growth in a MBE chamber, thanks to the UHV operation conditions, benefits from the possibility to in-situ monitor the surface morphology during the growth of successive layers through RHEED. In this technique, a beam of high-energy electrons is shot at the sample surface at a glancing angle and detected by a phosphorus screen after being diffracted by the sample crystal structure, impinge on the screen. The intensity and profile of the resulting diffraction pattern gives information about the changing surface morphology.

Depending on the materials used, three growth modes can be identified; these are summarised in fig. 2.2. Which growth mode takes place is determined by the binding energy to the surface (E_S) and the lateral binding energy to the neighbouring atoms of the deposited adatom (E_N). When $E_S > E_N$, the Frank-van der Merwe (or layer-by-layer) growth mode

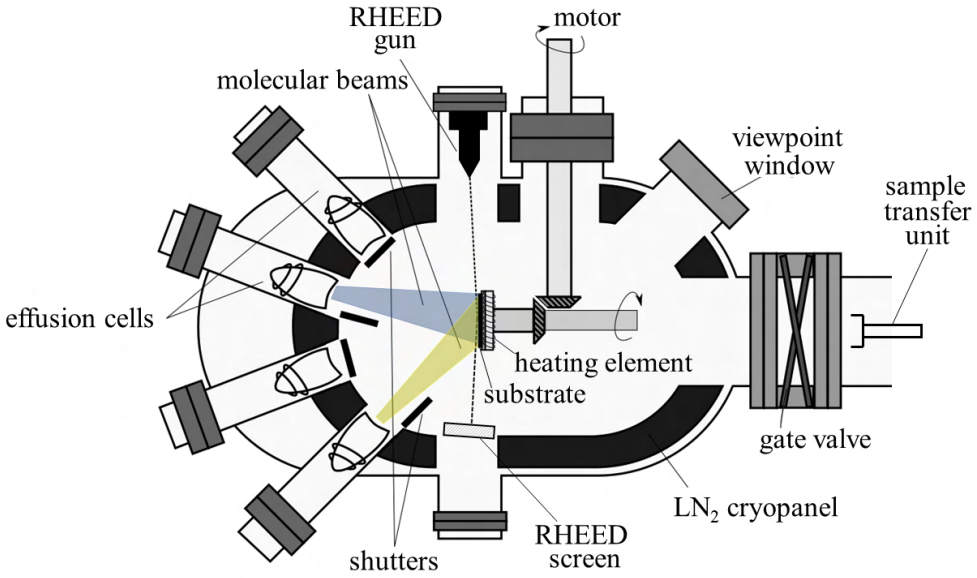

Figure 2.1: Simple diagram of an MBE chamber [60]; the main components are indicated.

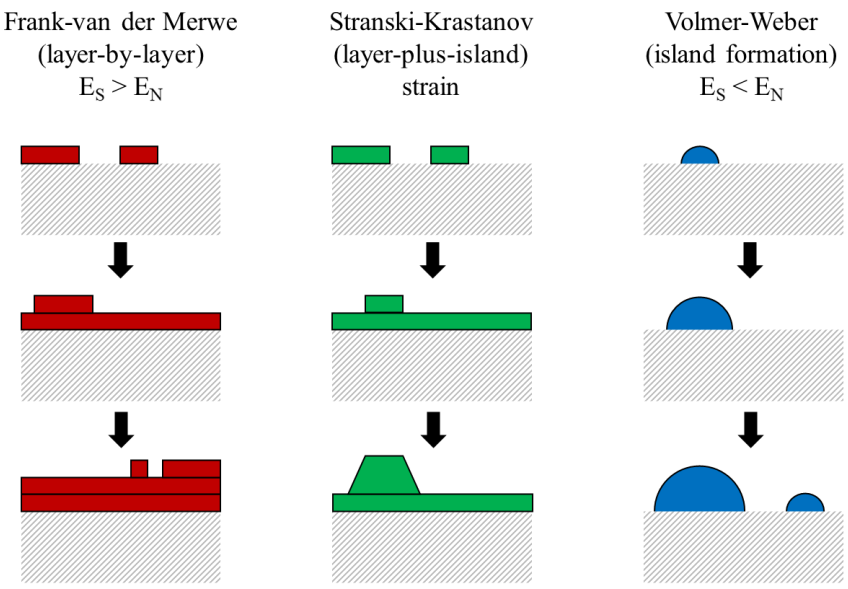

Figure 2.2: Thin film growth modes obtained for different binding energy of the adatoms to the surface (E_S) and to neighbouring adatoms (E_N); the intermediate regime obtained due to strain is also included (Stranski-Krastanov).

is obtained [61]; due to the preferential attachment to the surface site, ideally fully-formed atomic 2D layers are grown before the successive layer growth starts, leading to smooth layers and interfaces [62]. On the contrary, if $E_S < E_N$, the Volmer Weber (or island formation) growth mode is obtained [63]; in this case, the adatoms tend to attach to each other forming 3D adatom clusters, or islands. An intermediate growth mode is the Stranski-Krastanov (or layer-plus-island) growth mode, in which both 2D layers and 3D islands are formed. As previously introduced, this growth mode is strain-induced and the transition from layer-by-layer to island formation depends on the physical and chemical properties, such as lattice constants and surface energies, of the grown thin film and the substrate [64]. As mentioned, the fabrication of self-assembled strain-induced QDs, like InAs QDs on GaAs substrate, bases on this growth mode and has a typical island density of $10^{10}\,\mathrm{cm}^{-2}$ and around 30 nm diameter [65].

2.2 Local droplet etching (LDE)

The QDs of the present work are grown by filling self-assembled nanoholes obtained by the recently developed local droplet etching method, without the need of any lithographic step. LDE is fully compatible with standard solid-source MBE equipment. The nanoholes can be fabricated on GaAs [54], AlGaAs [66, 67] and AlAs [68] using, as etching material, Ga [54, 69], Al [55, 68], In or InGa [70]. The nanohole fabrication starts with the growth of a

buffer layer of the desired material. After that, the As effusion cell is closed, obtaining an As flux approximately 100 times lower than the usual conditions during GaAs growth. For this technique, a valved group-V source is essential for fast reduction of the beam pressure. The reduced flux is crucial for droplet formation [69]. Then, the droplet material is deposited, with a coverage of 1-3 monolayers (ML), by opening the etching material effusion cell, and droplets are generated in Volmer-Weber mode [71] (fig. 2.3a and b and fig. 2.4a). A 180 s post-growth annealing step follows, in which the droplets convert into nanoholes. During this step, the As diffuses from the substrate into the liquid droplets due to the concentration gradient (fig. 2.3c and fig. 2.4b). This causes the substrate right underneath the droplets to liquefy and the As concentration in the droplets to increase. As a consequence of the higher As content, the droplet material crystallises with the extra As at the boarder of the droplets, forming a ring-shaped wall surrounding the hole opening [56] (fig. 2.3d). At this point, the remaining liquid material is removed. It is assumed [73] that the droplet material escapes from the droplet, spreads over substrate surface, and forms there a planar layer together with background As. For the removal, the presence of a small As background, provided by a small As flux or by the topmost As-terminated surface as a reservoir [72], is crucial. In fact, without it, detached droplet material re-attaches and the liquid droplets are conserved [74]. With the correct As background, the detached material crystallises on

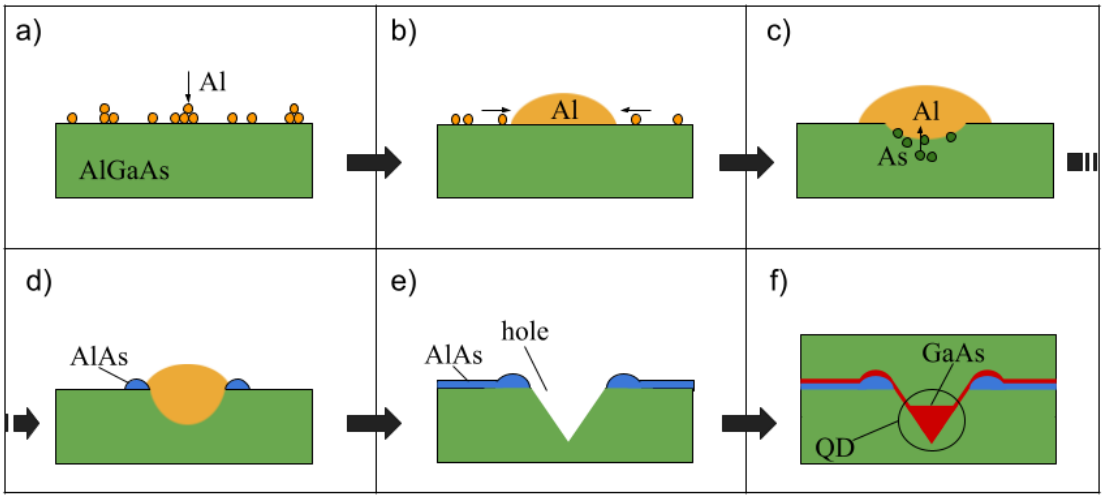

Figure 2.3: Steps to obtain QDs through LDE using Al as etching material. (a) Deposition of the droplet material Al; (b) formation of Al droplets in Volmer-Weber mode; (c) As diffusion from the substrate into the liquid droplets and liquefaction of the substrate material underneath the droplets; (d) droplet material crystallisation forming AlAs walls; (e) removal of the liquid material and nanohole formation; (f) filling of the nanohole with GaAs and capping with AlGaAs for the formation of QDs.

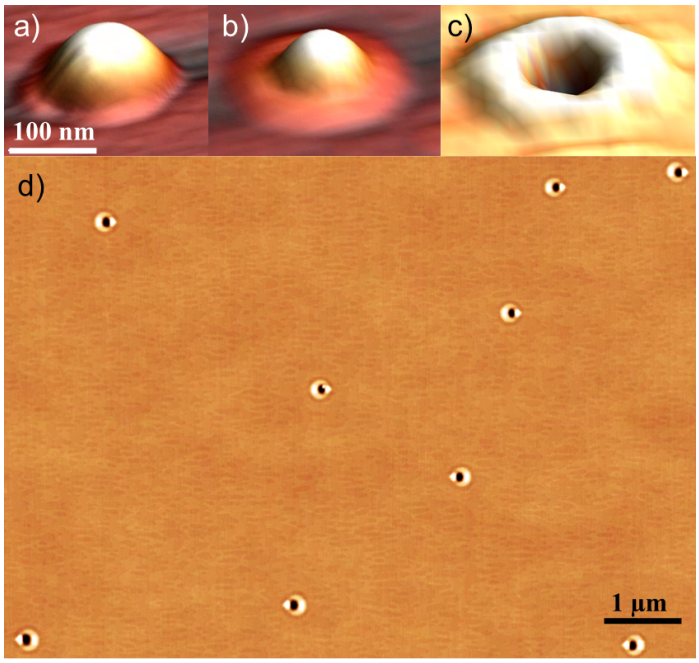

Figure 2.4: (a) AFM image taken after the deposition of a Ga droplet on an AlGaAs surface, (b) the transformation of the droplet into a nanohole with size reduction by escape of atoms, liquefaction of the substrate underneath the droplets caused by diffusion of As from the substrate into the droplet and (c) the GaAs wall formation [55]. (d) Large are AFM image of an AlGaAs surface showing low density nanoholes with AlAs walls after LDE with Al [72].

the substrate surface along with the As. The nanoholes are thus obtained (fig. 2.3e and fig. 2.4c and d). The characteristics of the LDE nanoholes, such as size, shape and density, can be adjusted by properly choosing the droplet and substrate materials and by tuning the process parameters. In particular, the main parameters to be regulated are the arsenic flux, the etching material coverage and the process temperature [75].

2.2.1 LDE quantum dots

By using LDE nanoholes as template, QDs and other versatile nanostructures can be obtained. To create QDs, the nanoholes are partially filled in a growth-interrupted manner, with a discrete number of short pulses alternated with breaks, allowing for a more uniform material deposition.

The QD shape and size along the xy direction is determined by the nanohole shape and the size along the z direction by the amount of deposited filling material inside the hole. A capping layer is then deposited to act as barrier material (fig. 2.3f). Depending on the thickness of the capping material, hills are visible above the buried QDs in atomic force microscopy

(AFM) images and can be used as markers to determine the QD position. Moreover, for further AFM investigations of the nanohole or the QD morphology, an additional LDE process, followed by a filling step (if needed), can be performed with the same parameters used in the previous layer. An AFM image taken for estimating the nanohole density (and thus the QD density) is shown in fig. 2.4d.

A precise estimation of the QD shape and size is important for the development of the simulation model explained in the next chapters. The nanohole shape, and thus the shape of the QD bottom part, depend on the droplet material and the temperature during the nanohole drilling phase. When Al droplets are deposited on AlGaAs, the angle α between the plane surface and the side facet of the resulting nanohole is between 15° and 35° [76] (fig. 2.5a, top). The depth d from the highest point of the AlAs ring to the bottom of the nanohole is controlled by the temperature T at which the Al droplets are deposited and can vary from 10 nm for $T = 600\,°C$ to 125 nm for $T = 680\,°C$ [75, 78]. The shape of the top part of the QDs is determined by capillarity. The QDs resulting from filling these nanoholes have a cone-shell shape, as shown by the AFM image (fig. 2.5a, bottom).

When the Al droplets are deposited on an AlAs layer instead of directly on the AlGaAs,

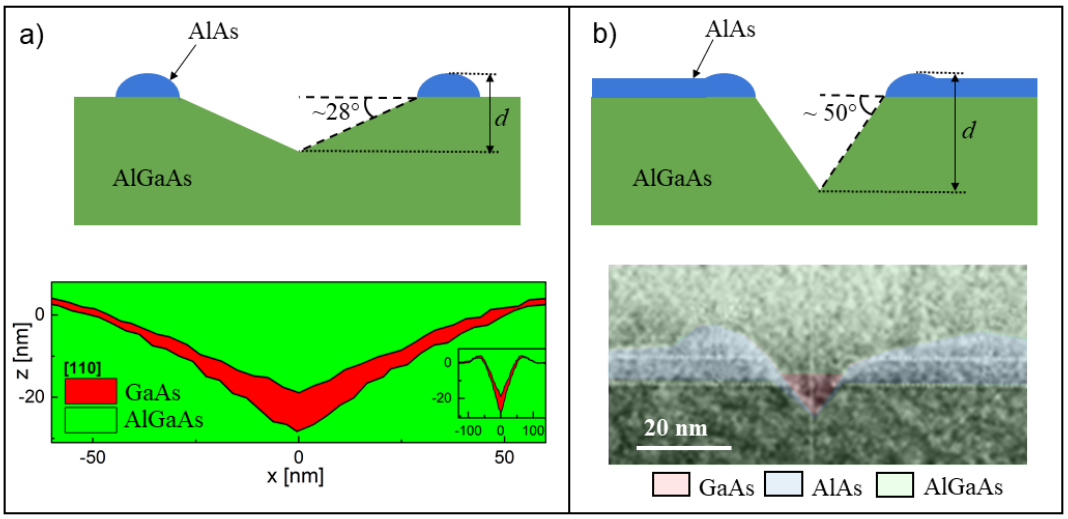

Figure 2.5: (a) Schematic of the nanohole obtained by local droplet etching with Al droplets on AlGaAs (top), with the angle α and the hole depth d indicated, and corresponding QD image (bottom) obtained by combining AFM images taken from different samples after the nanohole formation and after the GaAs filling step, respectively. (b) Schematic of the nanohole obtained by local droplet etching with Al droplets on AlAs (top) and TEM image of the corresponding QD (bottom) [77]. The colours are as guide for the eyes, the real image is in grey scale.

the facet-angle is $\alpha \simeq 50^\circ$ and the resulting QDs are cone-shaped (fig. 2.5b, top). Due to the fast oxidation of the AlAs layer, AFM images of these QDs in air are not reliable and hence transmission electron microscopy (TEM) is used to study the QD morphology. An example of a QD obtained by LDE using Al on AlAs at $T = 650\,^\circ\mathrm{C}$ is shown in fig. 2.5b, bottom [77].

Chapter 3

Theoretical background

This chapter covers the most important theoretical aspects needed to understand and interpret the results discussed in the thesis. Following a brief general overview on QDs' characteristics, the main focus is turned onto their optical properties. In particular, the influence of temperature, electric field and magnetic field on the optical properties is illustrated.

3.1 Confined nanostructures

MBE and other epitaxial techniques allow the deposition, with atomic precision, of thin films of semiconductors. Of particular interest are heteroepitaxial processes, through which materials of different bandgap are deposited on top of each other, thus obtaining semiconductor heterostructures. When a thin layer of a semiconductor with bandgap $E_g^{(1)}$ is embedded in a semiconductor with bandgap $E_g^{(2)} > E_g^{(1)}$, a potential well with width equal to the thickness L_z of the embedded semiconductor is obtained due to the difference in bandgaps between the two materials. If L_z is smaller than the de Broglie wavelength of the charge carriers in the embedded semiconductor, the carriers are quantum confined in the potential well, as opposed to the bulk semiconductor where the carriers are represented by Bloch waves expanding over the entire crystal. The described structure in which the carriers are free to move in two dimensions and confined in one (the direction perpendicular to the plane), is referred to as quantum well (QW). A structure confined in two dimensions is denoted as quantum wire, whilst when the spatial confinement occurs in all the three dimensions, a QD is obtained. It is important to note that, in the case of a QD, where the surface to volume ratio is maximised, a pure defect free interface between the epitaxial layers is crucial for the optical survival of the nanostructure.

The remarkable properties exhibited by low-dimensional quantum systems are often a consequence of the different functional forms of the density of states ρ. In the bulk material, $\rho(E)_{3D} \propto E^{1/2}$, in a QW $\rho(E)_{2D} = const$ (independent of the energy), in a quantum wire

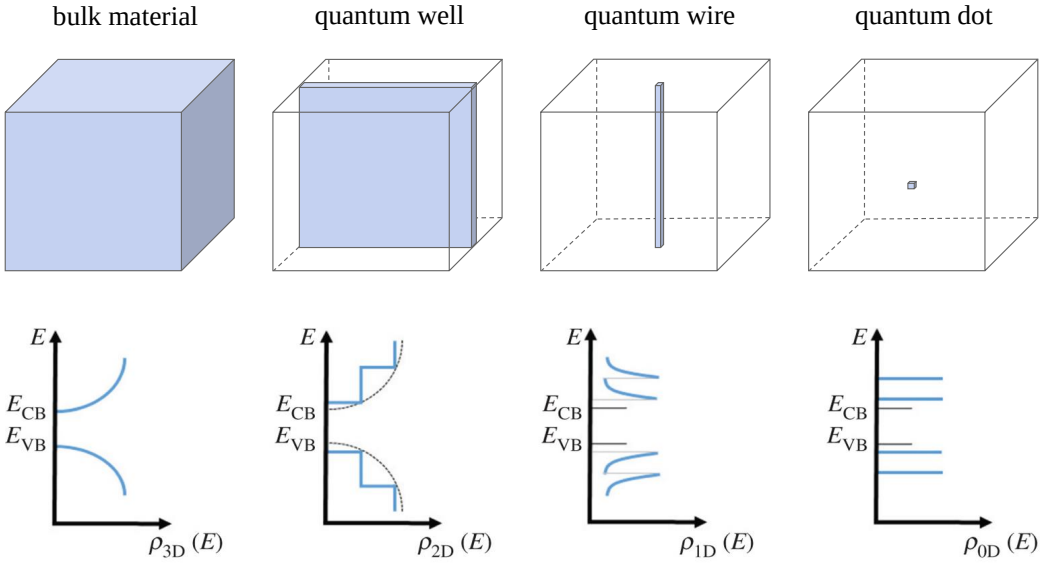

Figure 3.1: Upper row: simple schematic of bulk material and spatially confined systems. Lower row: corresponding density of states ρ as function of the energy, for both electrons (above the bandgap) and holes (below the bandgap); E_{CB} and E_{VB} are the conduction and valence bands respectively

$\rho(E)_{1D} \propto E^{-1/2}$ and in a QD $\rho(E)_{0D} \propto \delta(E)$. Similar arguments hold for both electrons and holes. Furthermore, with a more detailed analysis of the density of states, it can be noted that the energy gap between electron and hole states increases with reducing dimensionality, as a consequence of the stronger confinement. The dependence of ρ on the energy for the bulk and the various confined systems is shown in fig. 3.1, for both electrons and holes. In the case of the QD, ρ is represented by a δ-function, unlike the densities of state of the other solid-state systems, which are continuous functions of E. In thermal equilibrium, the average occupation of energy states with charge carriers is given by the integral of the product between the Fermi distribution and ρ. An outcome of the QD ρ behaviour is that the recombination of electrons and holes in a QD results in discrete transition energies, resembling an atom.

The electronic structure of a QD can be described as a function of the effective mass of the charge carriers and is strongly dependent on the form of the confining potential which results from the QD morphology[1]. The QD size is one parameter that affects the potential:

[1]Diagrams and discussions throughout this thesis assume the envelope function approximation. According to the Bloch theorem, the wavefunctions of electrons and holes in a crystal are given by the product of a oscillating orbital-like wavefunction and a periodic envelope function (plane wave). Within the envelope function approximation, only the linear combination of the plane waves is considered. This has implications also in the optical selection rules, as described in ch. 7. Further details can be found in text books [79].

with decreasing QD size, the confinement energy becomes larger and, as a consequence, so does also the spacing between the energy levels. The shape of the QD also affects the confinement potential as it determines the spatial position and shape of the electron and hole wavefunctions, and thus the wavefunction overlap which is directly related to the recombination lifetimes, as will be described later. Furthermore, the symmetry of the QD shape, and hence of the confinement potential, is linked to the electronic state degeneracy: generally, an asymmetric confinement potential causes the splitting of degenerate states. The material composition of the QD also defines the bandgap energy, which influences the spacing between the electron and hole energy levels and the height of the potential well. Moreover, if the lattice constants of the QD and barrier material are different, strain fields are present in the vicinity of the QD, affecting the conduction and valence band. Other consequences of the strain are symmetry reduction due to piezoelectric fields and degeneracy lifting of the highest valence bands. In this thesis, only GaAs QDs in an AlGaAs barrier are considered. Since GaAs and AlGaAs have almost identical lattice constants, the influence of strain on the QD confinement potential can be neglected.

3.2 QD photoluminescence (PL)

Electrons and holes in a QD, due to the interaction between particles of opposite charge, form quasi-particles called excitons (X), the energy of which can be obtained by the Hamiltonian

$$H_X = H_e + H_h + H_C \tag{3.1}$$

where H_e and H_h are the single particle Hamiltonians and H_C is the Hamiltonian describing the Coulomb interaction between the two charge carriers. The total energy of an exciton is less than the sum of the energies of the single particles due to the attractive force between them. The difference in energy is given by the binding energy E_B. Besides X, additional excitonic complexes can be obtained in the QD, depending on the number of carriers involved in the formation of the exciton complex. Some examples are shown in fig. 3.2. These are a biexciton (XX), obtained with two electrons and two holes in the ground state, a positive trion (X^+) with one electron and two holes, a negative trion (X^-) with one hole and two electrons, a doubly positively charged exciton (X^{++}) and a doubly negatively charged exciton (X^{--}). Due to their close proximity inside a QD, charge carriers are affected by each other. For example, the energy of an exciton and the energy of a biexciton, composed of two excitons, differ by the biexciton binding energy, due to the higher number of Coulomb interactions between the four charge carriers forming a biexciton. The Coulomb energy is

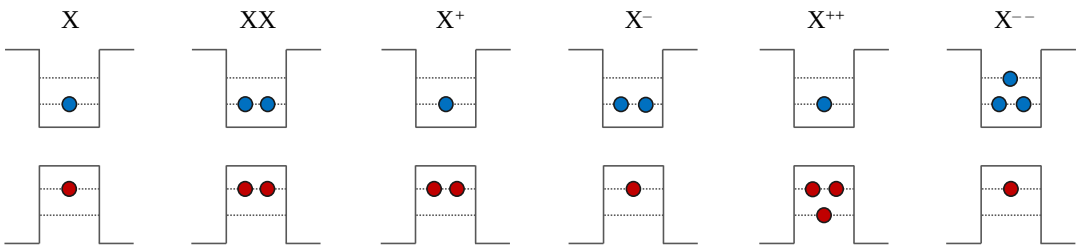

Figure 3.2: Schematic of various configurations of electrons (blue) and holes (red) in a QD: exciton (X), biexciton (XX), positive trion (X^+), negative trion (X^-), doubly positively charged exciton (X^{++}) and doubly negatively charged exciton (X^{--}).

given by the Coulomb integral

$$C_{ij} = \int\int \frac{e^2}{4\pi\epsilon_r\epsilon_0} \frac{|\Psi_i(\vec{r}_i)|^2 |\Psi_j(\vec{r}_j)|^2}{|\vec{r}_i - \vec{r}_j|} d\vec{r}_i d\vec{r}_j \tag{3.2}$$

where the indeces $i, j = e$ and h for electron and hole respectively, e is the electron charge, ϵ_r and ϵ_0 the relative and vacuum permittivity respectively, Ψ the carrier wavefunction and $\vec{r}$ the carrier vector position. The exciton energy is

$$E_X = E_e + E_h + C_{eh} \tag{3.3}$$

and the biexciton energy is

$$E_{XX} = 2E_e + 2E_h + C_{ee} + 4C_{eh} + C_{hh}. \tag{3.4}$$

It should be noted that eqs. (3.3) and (3.4) are not complete, since an additional contribution, the exchange interaction, needs to be considered in the Coulomb interaction when taking into account the fermionic nature of electrons and holes forming the excitonic complexes. When two identical particles a and b are exchanged with respect to both spatial and spin coordinates, the total wavefunction $\Psi_{ab} = \psi_a \times \psi_b$ remains either unchanged for bosons ($\Psi_{ab} = \Psi_{ba}$) or, as a consequence of Pauli exclusion principle, changes in sign for fermions ($\Psi_{ab} = -\Psi_{ba}$). Taking into account the fermionic nature of the electrons, the many-electron states must hence be antisymmetric with respect to particle interchange. Given the precondition of anti-symmetric basis functions, the exchange interaction can be considered as a spin-spin interaction between the participating particles [80, 81]. The exciton level is then composed of a multiplet of states, of which each degenerate state associated to different spin configurations of the charge carriers is lifted via the exchange interaction.

For zinc-blende materials, such as GaAs, the exciton ground state is six-fold degenerate at the Γ point [82], with two possible electron spin configurations $\left|s^{(e)}, m_s^{(e)}\right\rangle = \left|\frac{1}{2}, \frac{1}{2}\right\rangle$ and $\left|\frac{1}{2}, -\frac{1}{2}\right\rangle$ and four hole spin configurations $\left|s^{(hh)}, m_s^{(hh)}\right\rangle = \left|\frac{3}{2}, \frac{3}{2}\right\rangle$ and $\left|\frac{3}{2}, -\frac{3}{2}\right\rangle$ (heavy holes) and $\left|s^{(lh)}, m_s^{(lh)}\right\rangle = \left|\frac{3}{2}, \frac{1}{2}\right\rangle$ and $\left|\frac{3}{2}, -\frac{1}{2}\right\rangle$ (light holes), where s and m_s are the spin quantum number and the spin magnetic quantum number (or the z component of s), respectively. The split-off holes, with states $\left|s^{(soh)}, m_s^{(soh)}\right\rangle = \left|\frac{1}{2}, \frac{1}{2}\right\rangle$ and $\left|\frac{1}{2}, -\frac{1}{2}\right\rangle$, due to spin-orbit coupling, are energetically far enough from the valence band edge to be neglected in good approximation in GaAs. Furthermore, in QDs, the hole ground states is of heavy hole character with a probability of more than 96% [83], thus, from this point, light holes will be neglected and, in the following, the term hole will refer to a heavy hole. The exciton spin states are then four-fold degenerate: $|1\rangle$, $|-1\rangle$, $|2\rangle$ and $|-2\rangle$. Only the excitons in the former two states can absorb and emit photons with spin ± 1 and thus these excitonic states are called bright, whilst the latter two states are called dark states.

The degeneracy of the exciton ground state multiplet is lifted by two contributions: the exchange interaction (fig. 3.3), with the consequent coupling of electron and hole spins, and the electron and hole Zeeman interaction in the presence of a magnetic field B [81, 84]. The isotropic exchange interaction causes the splitting between bright and dark states independently of the QD shape. Moreover, in an asymmetric QD, where the confinement

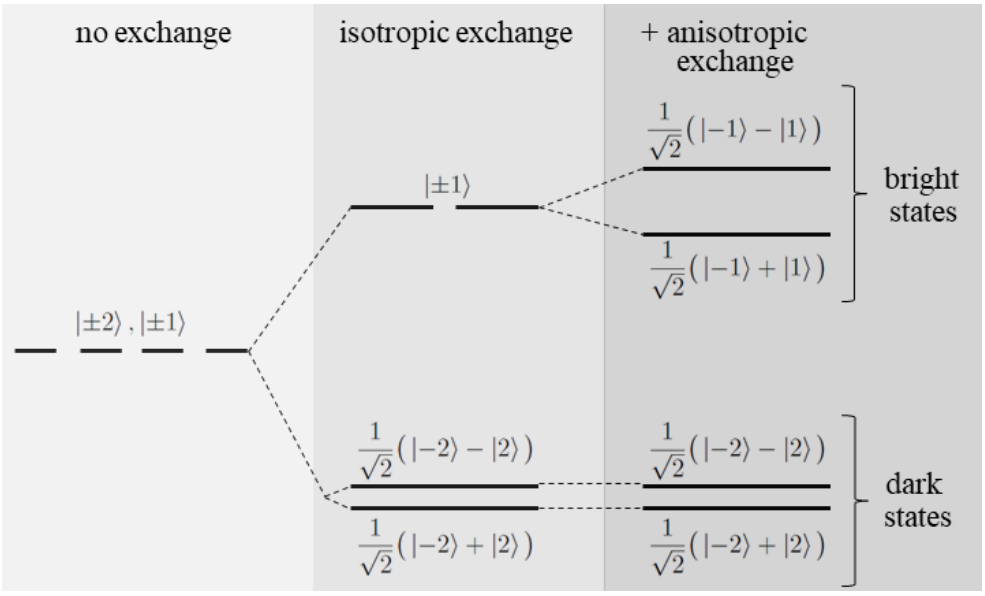

Figure 3.3: Schematic of the lowest energy exciton states in QDs, from left to right, without exchange interaction, with isotropic exchange interaction and with additional anisotropic exchange interaction. The number of degenerate states are indicated by the number of dashes [80].

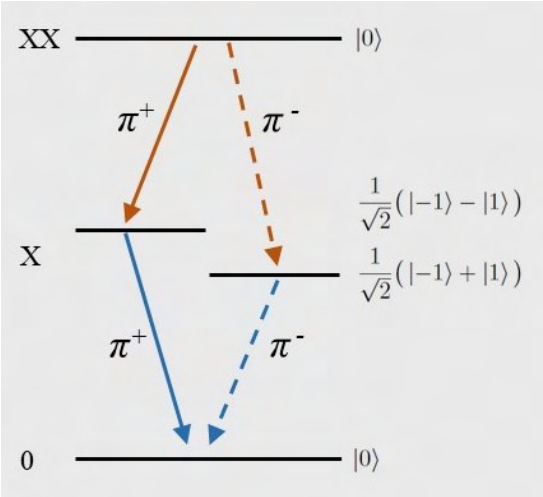

Figure 3.4: Schematic of the transitions for the XX $\rightarrow$ X $\rightarrow$ 0 cascade. Lifted degeneracy of the exciton bright states is indicated, with π^+ and π^- corresponding to linearly (and orthogonally) polarised light [80].

potential is not isotropic on the growth plane, the exchange interaction also causes an intermixing between the bright states or between the dark states (or both, depending on the QD shape), removing the degeneracy and leading to the bright states $\frac{1}{\sqrt{2}}\big(|-1\rangle \pm |1\rangle\big)$ and the dark states $\frac{1}{\sqrt{2}}\big(|-2\rangle \pm |2\rangle\big)$ [81]. Experimentally, the lifted degeneracy between the two bright states is reflected in the spectral transition lines by the fine structure splitting (FSS) (fig. 3.4) [85]. The FSS is interesting for applications in quantum communication since a large FSS can prevent the generation of entangled photons [7, 8, 58]. In the absense of B, the FSS is an indication of the asymmetry of the nanostructure. In the presence of B, the FSS is extended by the Zeeman interaction between B and the electron and hole spins [86].

In an asymmetric QD, a further consequence of the excitons being in bright states made of a superposition of $|-1\rangle$ and $|1\rangle$ states, is that the photon resulting from the recombination is in a superposition of left and right circular polarization. Hence, the emitted light is linearly polarized perpendicularly and in parallel to the anisotrophy axis [85, 86].

The biexciton shows a FSS identical to that of the exciton. This is because the biexciton is a spin-singlet state, as the two electrons and the two holes occupy closed shells. Therefore, the biexciton is subject to neither exchange nor Zeeman interaction splitting [86–88]. The biexciton has then two possible decay paths into one of the two non-degenerate bright states of the exciton, thus its spectral FSS and the emitted light polarization are completely determined by the excitonic ones.

3.2.1 Recombination statistics

The assignment of the recombination peaks presented in this work (ch. 5 and ch. 6) is based on power dependent PL measurements. The behaviour of recombination rates of different excitonic complexes depend on the excitation rate R, which can be estimated using the simple rate model described in the following.

For the experiments performed in this work, the excitons are generated in the AlGaAs barrier material by illumination, so R represents the relaxation rate into the QD s-shell and is assumed to be proportional to the laser excitation power P_E:

$$R = c_E P_E \tag{3.5}$$

where the proportionality constant c_E is the excitation efficiency. For the scope of this thesis, it is assumed that, to each electron excited into the conduction band a hole is obtained in the valence band, and an exciton is generated, with no formation of free charge carriers in the process. Hence, only neutral X and XX are considered. Moreover, dark states are here neglected. Hence, it is assumed that the QD can be in one of these three states: empty, occupied with one exciton or occupied with two excitons. The corresponding occupation probabilities are N_0, N_X and N_{XX} respectively.

Since the formation of a XX takes place when a QD is already occupied by an X, the probability of the XX formation is N_X, divided by half to account for Pauli exclusion principle. The XX decay time, with subsequent formation of an X, takes a time τ_{XX}. This process is summarised by the following rate equation:

$$\frac{dN_{XX}}{dt} = \frac{N_X R}{2} - \frac{N_{XX}}{\tau_{XX}}. \tag{3.6}$$

The formation of an X can occur either from the removal of an empty state by excitation, with occupation probability $N_0 = 1 - N_X - N_{XX}$, or following the recombination of one of the two excitons forming a XX. The X is destructed after its recombination lifetime τ_X or whenever a XX is formed by excitation, thus yielding for the X the following rate equation:

$$\frac{dN_X}{dt} = \Big(N_0 - \frac{N_X}{2}\Big)R + \frac{N_{XX}}{\tau_{XX}} - \frac{N_X}{\tau_X}. \tag{3.7}$$

The decay or the formation of an X respectively creates or removes an empty QD state, which can be described by the rate equation

$$\frac{dN_0}{dt} = \frac{N_X}{\tau_X} - N_0 R. \tag{3.8}$$

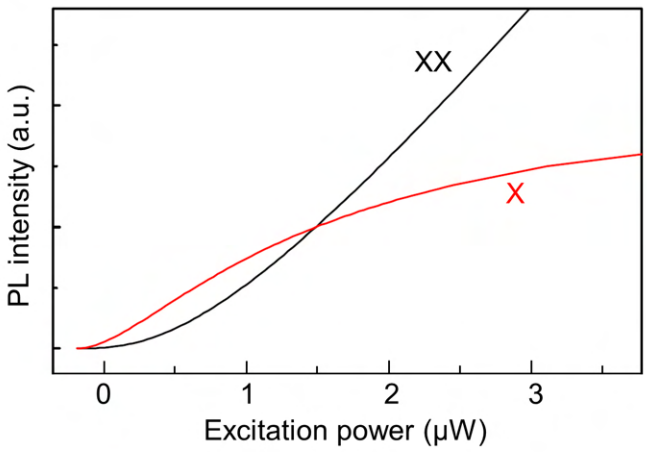

Figure 3.5: Expected exciton X and biexciton XX PL peak intensity dependence on the excitation power, calculated using a simple rate model.

The model is consistent with the balance equation at continuous illumination:

$$\sum_{i=0,X,XX} \frac{dN_i}{dt} = 0. \tag{3.9}$$

Solving the X and XX rate equations (eq. 3.7 and eq. 3.6) and calculating the results in equilibrium (i.e. for $t \to \infty$), the dot occupation probabilities as function of R, for continuous wave excitation, are obtained and are given by

$$\lim_{t\to\infty} N_X = \frac{2\tau_X R}{\tau_X \tau_{XX} R^2 + \tau_X R + 2} \tag{3.10}$$

and

$$\lim_{t\to\infty} N_{XX} = \frac{\tau_X \tau_{XX} R^2}{\tau_X \tau_{XX} R^2 + \tau_X R + 2}. \tag{3.11}$$

To calculate the X and XX generation rates in the limits $\lim_{t\to\infty} N_X$ and $\lim_{t\to\infty} N_{XX}$, lifetime values given in the literature [89], $\tau_X = 394\,\text{ps}$ and $\tau_{XX} = 426\,\text{ps}$, are used as an example. Assuming that these creation rates are proportional to the corresponding emission intensities, the expected PL intensities of the X and XX recombinations are computed and shown in fig. 3.5 [90] (red and black lines respectively). From the model, the X PL emission is expected to dominate at low excitation power and to then saturate when P_E is further increased. As the X peak saturates, the XX peak is expected to surpass the X peak intensity and to further increase as P_E increases.

3.2.2 Temperature influence

A major part of this work is the study of the temperature dependent QD PL emission. A specific and detailed analysis of the characteristics of the PL spectra at high temperatures,

including room temperature T_R, and their intensity loss as opposed to the spectra at low temperature is outlined in the relevant chapter (ch. 5). Here, a more general background theory on the influence of temperature on the PL emission is provided to better understand the upcoming analysis.

One important effect of the rising temperature on bulk semiconductors is the shrinkage of the material bandgap. This is caused by the atomic vibration becoming stronger as the temperature increases, which in turn increases the interatomic spacing [91]. The variation of the bandgap energy as function of the temperature is described by the Varshni relation [92]

$$E_g(T) = E_g(0) - \frac{\alpha T^2}{T + \beta}, \tag{3.12}$$

where $E_g(T)$ is the material bandgap energy at temperature T and, for GaAs, $E_g(0) = 1.518\,\text{eV}$ and the fitting parameters are $\alpha = (4.9 \pm 0.2) \times 10^{-4}\,\text{K}$ and $\beta = (203 \pm 8)\,\text{K}$ [93]. The bandgap energy shift causes also the QD PL emission to redshift with increasing temperature [94].

Besides the shift in bandgap energy, another consequence of rising the temperature is the broadening of the QD PL peak linewidth. This is caused by mainly two mechanism. One is the exciton-acoustic phonon coupling of the lattice relaxation treatment: the possible recombination of the coupled exciton-phonon state and change in the phonon occupation numbers gives rise to a broad background, consisting in the exciton-phonon side-bands, surrounding the single dot emission line (zero-phonon line) [95, 96]. The second mechanism causing the broadening of the PL peak is the scattering of charge carriers with acoustic and optical phonons [94, 97].

Increasing the temperature, another effect on the QD PL spectra is the reduction of the emission intensity. This phenomenon is described in details in ch. 5 through a rate model.

3.2.3 Electric field influence

Despite the high crystal purity achieved using MBE and specifically by the LDE method, the real crystal is never completely free of defects, such as doping atoms, interstitial defects, vacancies or dislocations. Charges in those can induce an electric field in the vicinity of a QD, affecting its transition energies and causing a broadening of the PL peaks [98].

Besides these unwanted sources, an intentional electric field can also be externally applied and controlled by means of gate electrodes to study the electric field dependent QD PL emission. One of the focuses of this thesis is indeed the analysis of QD PL spectra under

an externally applied uniform electric field F.

When an external F is applied, the electronic bands of the QDs bend and the electron and hole are shifted in opposite directions. In a type-I quantum well this causes a shift of the electron and hole wavefunction positions and thus of the emitted energy. In analogy to atomic physics, this effect is called quantum confined Stark effect (or Stark shift). In more detail, the Stark shift is determined by the three following different effects: as F increases, both the electrons and the holes are pushed according to their charge. This increases the distance d_{eh} between the charge carriers' wavefunction center of mass. Assuming a linear dependence $d_{eh}(F) = d_0 + \beta F$, where $d_0 = d_{eh}(F = 0)$ and β is the polarizability of the QD, the shift of the emission energy in the point charge approximation is

$$\Delta E = E(F) - E(F = 0) = -d_{eh}F = -\mu F - \beta F^2 \tag{3.13}$$

where $\mu = d_0$ is the built-in permanent excitonic dipole moment, oriented along the growth direction [99]. This effect lowers the recombination energy of a QD (fig. 3.6). Furthermore, the exciton binding energy is reduced due to the increased spatial separation between electrons and holes, which leads to an increase in the exciton energy and thus to a blue shift of the corresponding transition energy. The wavefunction overlap is reduced and thus also the time averaged PL intensity, since the oscillator strength, and hence the probability of the corresponding transition, decrease. For large F, the first effect (red-shift) dominates over the second one (blue shift) and thus a red-shift ΔE of the PL emission energy is observed

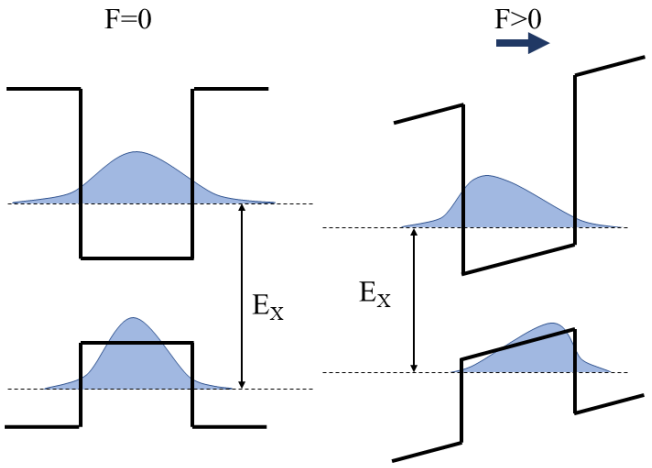

Figure 3.6: Schematic of a QD band diagram and the ground state electron and hole wavefunctions, with (left) and without external electric field F. The exciton energy E_X is indicated to show its reduction as a consequence of the band bending and QD shift, both caused by F.

with increasing F. For small F, the reduction of the exciton binding energy can compensate the red-shift.

3.2.4 Magnetic field influence

A magnetic field B applied to a QD strongly influences its PL emission, as is demonstrated in the simulations outlined in ch. 7. The effects arising from the interaction between B and the charge carriers can be analysed from different levels of complexity. This section gives a theoretical background through a simplified approach in the effective mass approximation and only illustrates the phenomena relevant for the understanding of the simulation results in ch. 7, since a more complex description is beyond the scope of this thesis.

The exciton Hamiltonian H_X is given by eq. 3.1, where the last term H_C, in Cartesian coordinates and within the mentioned approximation framework, is

$$H_C = -\frac{e^2}{4\pi\epsilon\epsilon_0|\vec{r}_e - \vec{r}_h|}. \tag{3.14}$$

The general form of the single particle Hamiltonian H_j ($j = e$ for electrons and h for holes with associated charge $q_e = -e$ and $q_h = e$ respectively) when an external magnetic field B and, for completeness, an external electric field F are applied, reads:

$$H_j = \frac{1}{2m_j^*}\left(i\hbar\vec{\nabla}_j + q_j\vec{A}_j\right)^2 - q_jFz + V_j(\vec{r}) \tag{3.15}$$

where $\vec{\nabla}_j$ is the gradient operator and $\vec{A}_j = -\frac{1}{2}\vec{r}_j \times \vec{B}$ is the vector potential used to describe B. Adopting the Coulomb gauge condition, $\vec{A}_j$ must satisfy $\vec{\nabla}_j \cdot \vec{A}_j = 0$. Then eq. 3.15 becomes

$$H_j = -\frac{\hbar^2}{2m_j^*}\vec{\nabla}_j^2 + \frac{i\hbar q_j}{m_j^*}\vec{A}_j \cdot \vec{\nabla}_j + \frac{q_j^2}{2m_j^*}\vec{A}_j^2 - q_jFz + V_j(\vec{r}). \tag{3.16}$$

In this thesis, B is always only applied in the growth direction z hence $\vec{B} = (0, 0, B)$. Defining $\vec{r} = x\hat{x} + y\hat{y} + z\hat{z}$, where $\hat{i}$ are unit vectors, the following is obtained: $\vec{r} \times \vec{B} = B(y\hat{x} - x\hat{y})$. From this result and given $\vec{\nabla}_j = \hat{x}\frac{\partial}{\partial x} + \hat{y}\frac{\partial}{\partial y} + \hat{z}\frac{\partial}{\partial z}$, the second and the third terms of eq. 3.16 can be rewritten as function of B, x and y, giving

$$H_j = -\frac{\hbar^2}{2m_j^*}\vec{\nabla}_j^2 - \frac{i\hbar q_j B}{2m_j^*}\left(y\frac{\partial}{\partial x} - x\frac{\partial}{\partial y}\right) + \frac{q_j^2B^2}{8m_j^*}(x^2 + y^2) - q_jFz + V_j(\vec{r}). \tag{3.17}$$

Using the definition of momentum operator $\mathbf{p} = -i\hbar\vec{\nabla}$ and orbital angular momentum operator $\mathbf{L} = (\mathbf{L_x}, \mathbf{L_y}, \mathbf{L_z}) = -i\hbar(\vec{r} \times \vec{\nabla})$, eq. 3.17 can be also written more neatly in terms of operators as

$$H_j = \frac{\mathbf{p}_j^2}{2m_j^*} + \frac{q_jB\mathbf{L_z}}{2m_j^*} + \frac{q_j^2B^2}{8m_j^*}(x^2 + y^2) - q_jFz + V_j(\vec{r}). \tag{3.18}$$

3.2.4.1 Fock-Darwin model

The energy spectrum of a flat QD ($n_z = 0$), where the confinement potential $V_j = \frac{1}{2} m_j^* \omega_{j,0}^2 r^2$ is parabolic and radially symmetric in polar coordinates, is described by the Fock-Darwin model [100]. Rewriting eq. 3.17 in polar coordinates, and omitting the term associated to the electric field, gives

$$H_j = -\frac{\hbar^2}{2m_j^*}\left(\frac{\partial^2}{\partial r^2} + \frac{1}{r}\frac{\partial}{\partial r} + \frac{1}{r^2}\frac{\partial^2}{\partial \theta^2}\right) - \frac{i\hbar q_j B}{2m_j^*}\frac{\partial}{\partial \theta} + \frac{q_j^2 B^2 r^2}{8m_j^*} + \frac{1}{2} m_j^* \omega_{j,0}^2 r^2. \tag{3.19}$$

Separating the variables, rearranging and defining the cyclotron frequency $\omega_{j,c} = \frac{eB}{m_j^*}$ the Hamiltonian can be simplified and the single particle eigenvalues E_{j,n_j,l_j} (Landau levels) are given by

$$E_{j,n_j,l_j} = (2n_j + |l_j| + 1)\hbar\sqrt{\omega_{j,0}^2 + \frac{\omega_{j,c}^2}{4}} \pm \frac{l_j \hbar \omega_{j,c}}{2} \tag{3.20}$$

where the last term is summed for electrons and subtracted for holes. An example of a resulting energy spectrum as function of B is shown in fig. 3.7 for holes. For $B > 0$, the degeneracies are lifted and the energy levels with positive and negative l_h move down and up respectively as B increases, due to the magnetic moment pointing opposite or along B. At large B ($\omega_c \gg \omega_0$), the energy levels converge into Landau levels as a consequence of the free particle behaviour prevailing over the confinement effect.

The above formulas are valid for a flat QD. For a later discussion (ch. 5), it is useful to

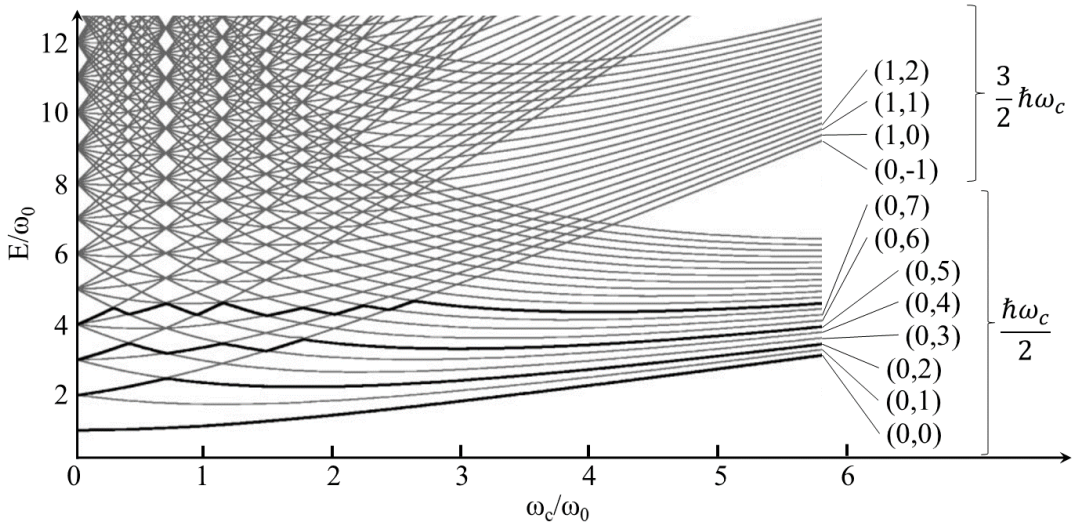

Figure 3.7: Schematic of the Fock-Darwin hole energy in units of ω_0 as function of ω_c/ω_0. Some of the levels are labelled with their quantum numbers (n_h, l_h). The ground state and, to show the change in l_h, also some excited states (second, fifth and ninth) are indicated with a bold line.

consider also a 3D model. Here, for simplicity and since it is beyond the scope of the mentioned discussion, no magnetic field is considered. Rewriting eq. 3.20 for a 3D system and with $l_j = 0$, the single particle energy levels are

$$E_{j,n_j} = \hbar\omega_{j,0}\left(n_j + \frac{3}{2}\right) \tag{3.21}$$

Given that, in an ideal case, $\omega_{j,0} \propto \frac{1}{m_j^* L^2}$, where L is the ground state oscillator length, which is here assumed to be the same for electrons and holes, the ratio between the electron and hole quantisation energy is

$$\frac{E_{e,n_e}}{E_{h,n_h}} = \frac{m_h^*}{m_e^*}. \tag{3.22}$$

Optical selection rules predict that, for allowed optical transitions, the electron and hole states must have equal quantum numbers $n_e = n_h$. The n^{th} level energy emission E_n is thus given by

$$E_n = E_g + E_{e,n} + E_{h,n} - C_{eh,n}. \tag{3.23}$$

Combining eqs. (3.22) and (3.23), the electron and hole quantisation energies become, respectively,

$$E_{e,n} = \frac{E_n - E_g + C_{eh,n}}{1 + m_e^*/m_h^*} \simeq 0.88(E_n - E_g + C_{eh,n}) \tag{3.24}$$

and

$$E_{h,n} \simeq 0.12(E_n - E_g + C_{eh,n}) \tag{3.25}$$

with the effective masses $m_e^* = 0.067m_e$ and $m_h^* = 0.51m_e$ and the electron rest mass m_e.

3.2.5 Exciton in a quantum ring

The above description covered particles in a QD. The following gives a theoretical description of a quantum ring, firstly considering an exciton in a one-dimensional ring and then an exciton formed by an electron and a hole in spatially separated rings.

The Hamiltonian of an exciton in a one-dimensional ring is

$$H_X = \frac{\hbar^2}{2m_e^* R^2}\left(-i\frac{\partial}{\partial\phi_e} + \frac{\Phi}{\Phi_0}\right)^2 + \frac{\hbar^2}{2m_h^* R^2}\left(-i\frac{\partial}{\partial\phi_h} - \frac{\Phi}{\Phi_0}\right)^2 - \frac{e^2}{2\epsilon\epsilon_0 R}\left|\sin\frac{\phi_e - \phi_h}{2}\right|^{-1} \tag{3.26}$$

where R is the ring radius, Φ is the magnetic flux through the ring and Φ_0 is the magnetic flux quantum [101]. By introducing the new variables $\phi_c = \frac{m_e\phi_e + m_h\phi_h}{m_e + m_h}$ and $\theta = \phi_e - \phi_h$, the exciton internal motion can be separated from its gyration as a whole in the ring [101], so that eq. 3.26 reads

$$H_X = -\frac{\hbar^2}{2(m_e + m_h)R^2}\frac{\partial^2}{\partial\phi_c^2} + \frac{\hbar^2}{2\mu R^2}\left(i\frac{\partial}{\partial\theta} - \frac{\Phi}{\Phi_0}\right)^2 + C_{eh}(\theta) \tag{3.27}$$

where $\mu = \frac{m_e m_h}{m_e + m_h}$ and the last term of eq. 3.26 represents the Coulomb interaction and is thus here indicated as $C_{eh}(\theta)$. The system's wavefunction can be expressed as

$$\Psi_X = \chi(\theta) e^{iA\phi_c + i\theta\frac{\Phi}{\Phi_0}} \tag{3.28}$$

where A is a real number and $\chi(\theta)$ satisfies the Schödinger equation

$$-\frac{\hbar^2}{2\mu R^2}\frac{\partial^2\chi}{\partial\theta^2} + C_{eh}(\theta)\chi = \left(E - \frac{\hbar^2}{2(m_e+m_h)R^2}J^2\right)\chi \tag{3.29}$$

with E the total energy of an exciton. The coefficient of χ in the right side of eq. 3.29 is the exciton internal energy and is named ω in the following. In order to assign a value to J and to determine the allowed solutions of eq. 3.29, Ψ_X is required to be periodic independently of ϕ_e and ϕ_h, with period 2π. Moreover, the solutions to eq. 3.29 are of the form $\chi = \nu(\theta)e^{ip\theta}$, with $-\frac{1}{2} < p < \frac{1}{2}$ and where ν is a periodic function of θ with period 2π, as this is the period of $C_{eh}(\theta)$ [101]. Adding 2π to ϕ_e and ϕ_h independently, the following relationships are obtained:

$$J\frac{m_e}{m_e+m_h} + \frac{\Phi}{\Phi_0} + p = N \tag{3.30}$$

and

$$J\frac{m_h}{m_e+m_h} - \frac{\Phi}{\Phi_0} - p = N', \tag{3.31}$$

with N and N' integers, from which it follows that J (rotational quantum number of the exciton) is also an integer. The eigenvalues ω of eq. 3.29 must be periodic functions of p ($\omega(p+1) = \omega(p)$). Given the relation between p and Φ/Φ_0 (eqs. (3.30) and (3.31)), the exciton binding energy should be a periodic function of Φ with period Φ_0. The oscillations of $\omega(\Phi)$ are caused by the fact that, in the trajectory of electrons and holes tunnelling towards one another along the ring, the wavefunction of the relative motion in the exciton takes the phase 2π times the number Φ/Φ_0 of flux quanta passed through the ring [101]. Assuming that $a_B \ll 2\pi R$, with a_B the effective Bohr radius, the tight binding approximation can be used to solve eq. 3.29. The binding energy has then the form

$$\begin{aligned}\omega_n &= E_n - \Delta_n \cos\left(2\pi\left(\frac{\Phi}{\Phi_0} + J\frac{m_e}{m_e+m_h}\right)\right) \\ &= E_n - \Delta_n \cos\left(2\pi\left(\frac{\Phi}{\Phi_0} - J\frac{m_h}{m_e+m_h}\right)\right)\end{aligned} \tag{3.32}$$

where n indicates the energy level of the exciton, Δ_n the tunnelling amplitude. Hence, the tunnelling leads to an oscillation of the exciton energy with Aharonov-Bohm (AB) period, albeit very weak due to the small tunnelling amplitude being of the order of $R_y e^{-2\pi R/a_B}$, where R_y is the Rydberg energy.

The above analysis is made considering an exciton in a one-dimensional ring, where the

electron and the hole have the same orbital radii. For the analysis in ch. 7, it is of interest to have a theoretical background also of an exciton formed by an electron and a hole orbiting in non-coinciding rings, in which case a radial dipole moment is obtained in the exciton. In the following, the simplest case is considered, where the electron and the hole are orbiting in concentric circles of radii R_e and R_h respectively. Introducing the variable $\phi_0 = \frac{m_e R_e^2 \phi_e + m_h R_h^2 \phi_h}{m_e R_e^2 + m_h R_h^2}$ and θ (as before), the internal motion of the exciton can again be separated from it gyration as a whole. However, in this case, the Hamiltonian of the center of mass depends on the magnetic field B and is given by

$$H_{X,c} = \frac{\hbar^2}{(R_e + R_h)(m_e R_e^2 + m_h R_h^2)} \left(-i \frac{\partial}{\partial \phi_0} + \frac{\Delta\Phi}{\Phi_0} \right)^2 \tag{3.33}$$

where the magnetic flux is $\Delta\Phi = \pi(R_e^2 - R_h^2)B$. The eigenvalues of $H_{X,c}$ are given by

$$E_J = \frac{\hbar^2}{(R_e + R_h)(m_e R_e^2 + m_h R_h^2)} \left(J + \frac{\Delta\Phi}{\Phi_0} \right)^2 \tag{3.34}$$

with $J = 0, \pm 1, \pm 2, ...$ The energies E_J represent those of the exciton gyration as a whole. To this, the energy ω of the electron-hole relative motion should also be added and can be calculated with the tight binding approximation, as in the previous case, assuming $a \ll R_e, R_h$. From eq. 3.34, it can be seen that the exciton ground state gradually transfers from the state with $J = 0$, to the ones with $J = 1$, $J = 2$, etc., as $\Delta\Phi$ increases. By doing so, the exciton energy oscillates with an AB period corresponding to the area difference of the electron and hole trajectories.

Chapter 4

Experimental and simulation methods

The measurements outlined in this thesis are performed on 8 samples, labelled #1 - #8[1], and containing LDE QDs in various sizes, shapes and densities. In this chapter, the fabrication method and process parameters are reported for each sample type[2]. Samples #4 - #8 are gated and contacted for electric field dependent measurements and thus these processes are also illustrated briefly. Further details on the technical methods and process parameters can be found in the appendix (app. A). A detailed description of the PL setup, the development of which is a major part of this PhD work, is also given in this chapter, followed by an explanation of the methods used to simulate the behaviour of a QD in electric and magnetic fields.

4.1 Sample fabrication

The samples studied in this work contain GaAs QDs fabricated with LDE method during solid-source MBE, as described in sec. 2.2. All the samples are fabricated on semi-insulating (001)GaAs wafers. Al droplets are used to drill nanoholes into AlGaAs or AlAs/AlGaAs heterostructures. The nanoholes are then filled with GaAs in pulsed mode and capped with AlGaAs to obtain the QDs. The composition and thickness of the grown layers is controlled by calibrating the GaAs and AlAs growth speed using RHEED (RHEED-12, STAIB Instrument GmbH, Munich, Germany). The shape and size of the LDE nanoholes is determined using atomic force microscope (AFM). The most relevant QD parameters are related to the

[1] In this thesis, the samples are renamed for clarity. The correspondence to the samples real number is here listed for reference: #1 = #2801; #2 = #196; #3 = #222; #4 = #2804; #5 = #3274; #6 = #3272; #7 = #2803 and #8 = 15446.

[2] Samples #1 to #7 are grown by previous group members. Sample #8 is grown by me in collaboration with Hans-Gerog Babin, from Ruhr-Bochum Universität.

temperature and droplet coverage during LDE, which controls the size, shape, and density of the nanoholes, and the number of filling pulses deposited for QD generation, which controls the QD size. Further important sample parameters are the Al content and the thickness of the AlGaAs barrier material, the number of QD layers, the distance between QD layer and sample surface, and the presence of a Si doped layer, which acts as a back gate for electric field dependent measurements. The eight samples studied in this thesis are here briefly compared. Details of the technical aspects of the sample fabrication and gate preparation are given in the appendix (app. A).

Samples #1 (fig. 4.1a) and #4 - #7 (fig. 4.1d and e) each contain a layer of low-density ($2 \times 10^7\,\mathrm{cm}^{-2}$) QDs grown on a thin AlGaAs layer (120 nm) and capped with 80 nm AlGaAs. The Al content of the barrier material is 33% for samples #1, #4 and #7 and 30% for samples #5 and #6. All these samples contain a 50 nm thick (Si)GaAs back gate for electric field-dependent measurements grown between a GaAs layer and the AlGaAs tunnel barrier layer. Sample #1 also contains an AlAs/GaAs superlattice (SL) grown on the GaAs substrate. The QDs are obtained by filling the nanoholes with 4 pulses of GaAs for samples #1 and #6 and with 2, 2.5 and 6 pulses for samples #4, #5 and #7 respectively.

Samples #4 - #7 are contacted for field-dependent measurements. The back contact pads are made of AuGe, which is annealed in order to reach the (Si)GaAs back gate layer. The top contact pads consist of 10 nm of Ti, 8 nm of Cr (for better adhesion) and 30 nm of Au. Samples #4 and #7 are dipped in HCl before the Ti deposition. The gates are obtained by depositing the gate materials through physical vapour deposition (PVD) on sample areas selected through photolithography. The mask designs used for the photolithography are shown in fig. 4.2 and the resulting gates of samples #5 and #6 and of samples #4 and #7 are shown in fig. 4.2b and c respectively. Top and back gates are contacted via Au wires.

Sample #2 (fig. 4.1b) contains a single layer of high-density ($4 \times 10^8\,\mathrm{cm}^{-2}$) QDs grown on AlAs/$Al_{0.37}Ga_{0.63}As$ heterostructure (5 nm/200 nm) and capped with 120 nm $Al_{0.37}Ga_{0.63}As$. An additional layer of QDs (optically inactive) is grown on top of the sample for AFM investigation. The nanoholes are filled with 5 pulses of GaAs.

Sample #3 (fig. 4.1c) contains a stack of 5 layers of high-density ($4 \times 10^8\,\mathrm{cm}^{-2}$) QDs grown on AlAs/$Al_{0.22}Ga_{0.78}As$ heterostructure, (5 nm/95 nm), with each QD layer separated by 20 nm of $Al_{0.22}Ga_{0.78}As$. The capping layer is 80 nm thick. Above and below the the tunnel barrier, thick (1.3 µm each) AlGaAs layers with high Al content (58% and 69% respectively) are grown. As for sample #2, the QDs are obtained by filling the nanoholes with 5 pulses of GaAs.

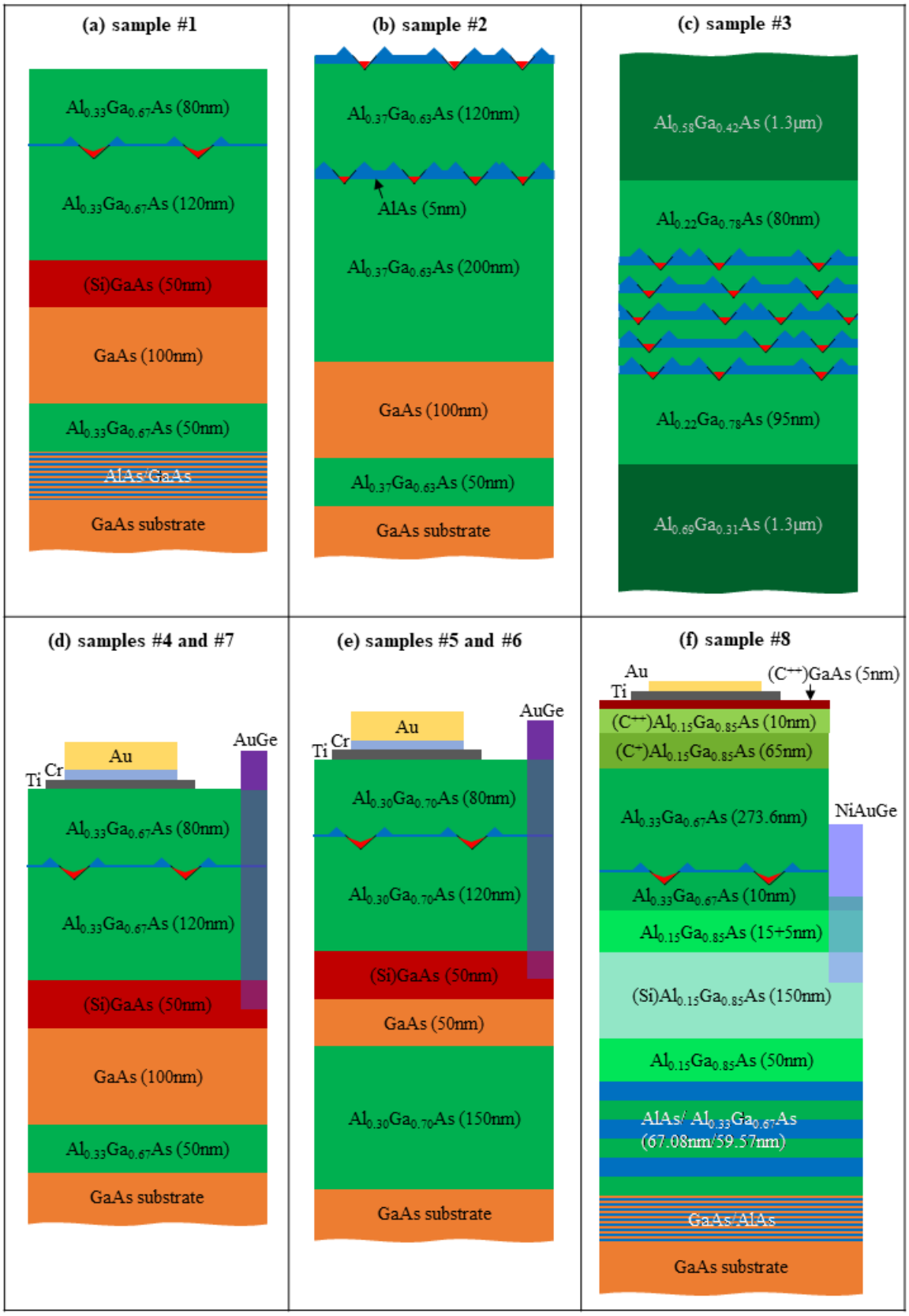

Figure 4.1: Schematic of the measured samples.

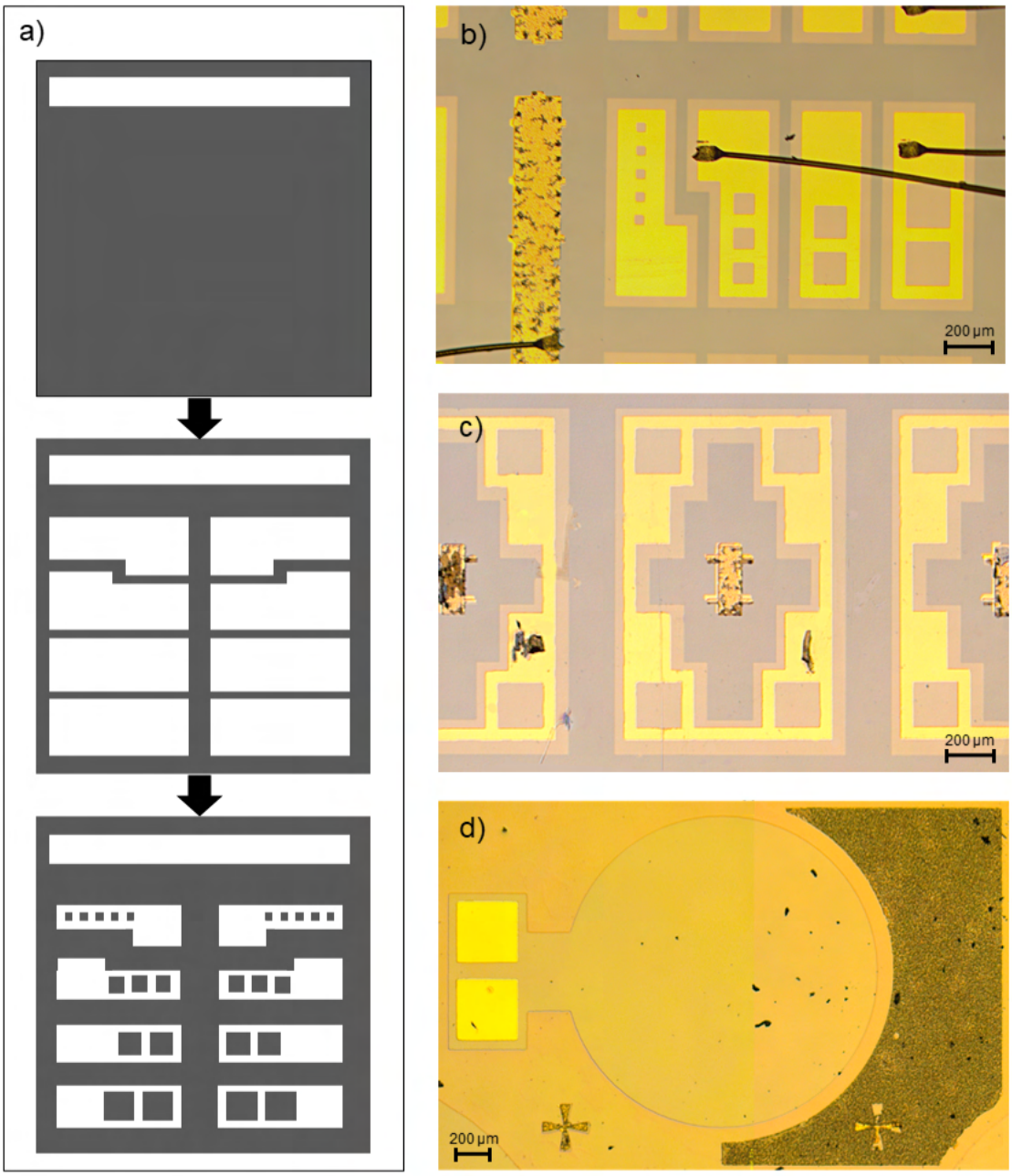

Figure 4.2: (a) Schematic of one of the mask designs used for the photolithography of gates. From top to bottom: back gate, Ti window, and Au frame masks. (b - d) Microscopy images of sample surfaces following the gate fabrication with 3 different designs, used (b) for samples #5 and #6, (c) for samples #4 and #7 and (d) for sample #8. The masks indicated in (a) are used for the lithography of the gates shown in (b). Some bond wires are visible in (b) whilst in (c) the wires are removed, leaving some marks. The image in (d) is taken before bonding.

Sample #8 (fig. 4.1f) has major differences with respect to the other samples described above. A SL and a distributed Bragg reflector (DBR) are grown above the substrate. The QDs are grown in $Al_{0.33}Ga_{0.67}As$ and have a density of $3.7 \times 10^7\,cm^{-2}$. One of the major difference in this sample are the gates. In fact, the sample has a p-i-n structure, with a $(Si)Al_{0.15}Ga_{0.85}As$ as back gate and an epitaxial top gate made of C-doped AlGaAs and GaAs layers. The metal contact pads are made of 3 nm of Ti followed by 7 nm of Au. The back gate pad is made of NiAuGe and annealed to the back gate layer, after an etching process to remove part of the layers in between. A microscopy image of the resulting gates is shown in fig. 4.2d. The wire bonding is done in the same way as for the other gated samples.

4.2 PL setup

The QD optical properties described in this work are studied with micro-PL spectroscopy measurements. The experimental setup used is illustrated in fig. 4.3. The experiments are performed using a continuous wave green laser diode of wavelength 532 nm. For a few measurements, a 405 nm blue laser diode is used instead. The laser beam passes a neutral density (ND) filter installed in a filter wheel. The motorised housing, with six

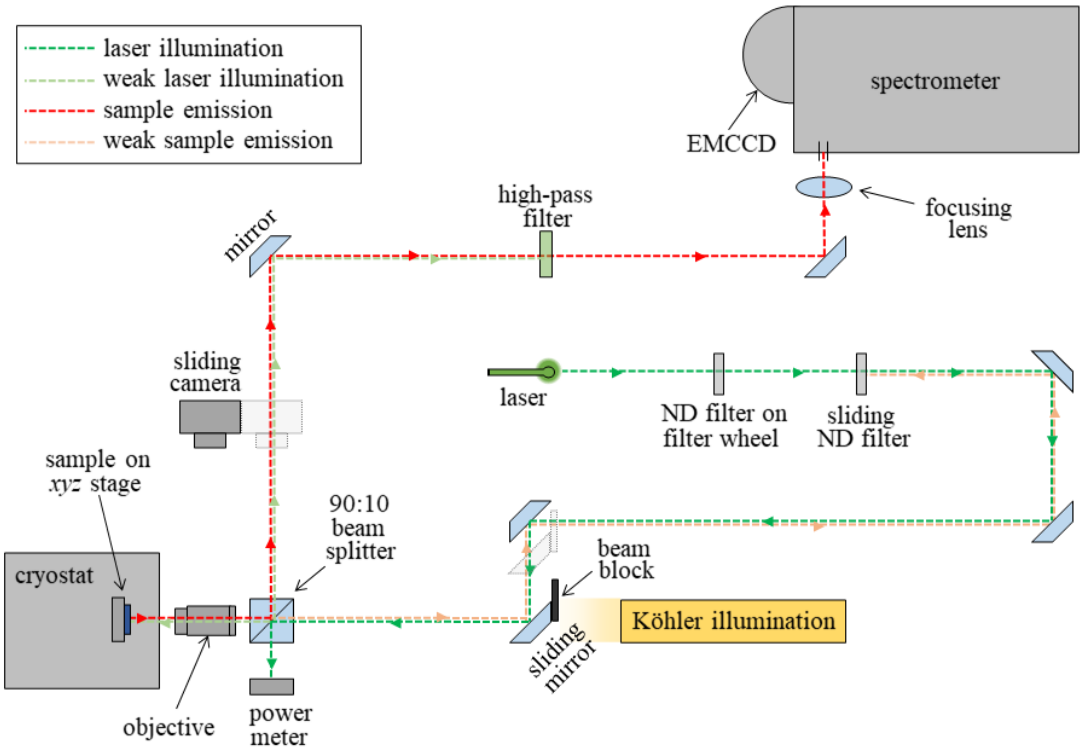

Figure 4.3: Schematic of the micro-PL setup.

filters with different attenuation factors, allows to select the desired filter for a first rough adjustment of the beam intensity. The beam passes then through a rectangular continuously variable reflective ND filter, which allows a further fine adjustment of the intensity as the filter attenuation can be linearly adjusted via translation. Following the filters, the beam is reflected on a set of mirrors, one of which can be moved in order to switch from the PL laser excitation to the microscopy feature, which is described separately. When the mirror is left in the position for the laser excitation, the beam is directed onto a 90:10 (R:T) beam splitter. The reflected part of the beam is used for in-situ intensity control of the beam by using a power meter with a standard photodiode sensor. The transmitted part is focused on the sample via a $\times 100$ objective that is installed inside the cryostat. The sample is mounted on a piezo-motor driven xyz-stage, which allows the movement of the sample with a precision of 100 nm and the focusing through the movement on the z direction. The sample on the stage sits inside a closed-cycle cryostat (Montana cryostation s200) for operation at low temperatures down to 3.3 K. Contact pins inside the cryostat allow electric field dependent measurements. The outgoing beam, comprising of the signal from the sample and the reflected laser light, is collected by the same objective and hits the same beam splitter. The reflected part (90% of the emission), passes by a high-pass filter. The filter lets through only light with wavelength above 650 nm, in order to remove the unwanted laser light reflected by the sample. The light passing through the filter is focused by a lens (120 mm focal length) into the slit of a grating spectrometer (Andor Shamrock SR-500i), which is equipped with 3 gratings (235 mm^{-1}, 600 mm^{-1} and 1200 mm^{-1}) with size 68 mm$\times$68 mm and an electron multiplying charged coupled device (EMCCD) camera (Andor Newton EMCCD with 1600$\times$200 array of 16 µm pixels and 3 mHz readout) for data acquisition. The acquired data are interpreted by the software Andor Solis, which provides the PL counts as function of wavelength.

4.2.1 Illumination

The description of the setup given so far covers only the laser excitation. The setup features also an inbuilt microscope for selecting desired areas from the samples. To move from excitation to microscopy, one of the mirrors before the beam splitter can be shifted, allowing the white light illumination and blocking the laser beam through a beam blocker attached to the mirror's sliding stage. The sample illumination is obtained through a Köhler illumination setup (fig. 4.4) adjusted for reflected light microscopy. The light, provided by a current-controlled white light LED, passes through three lenses, L1, L2 and L3 with focal lengths f_1, f_2 and f_3 respectively. Two irises, with adjustable aperture size, are used as aperture diaphragm (D1) and field diaphragm (D2). The light coming from the LED is

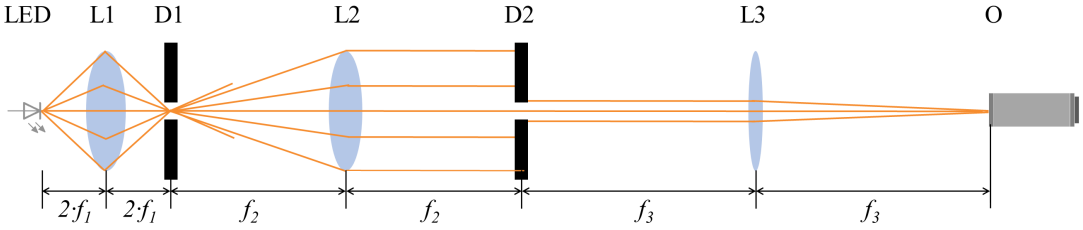

Figure 4.4: Schematic of the Köhler white light illumination setup adjusted for reflected light microscopy. The lenses are denoted as LN (N=1,2,3), with associated focal lengths f_N. The aperture diaphragm, the field diaphragm and the back focal length of the objective are indicated as D1, D2 and O respectively. The light rays are indicated with orange lines.

focused by L1 into D1 by setting the length between the LED and L1 and between L1 and D1 equal to $2f_1$. Due to the integrated lens of the LED, the distance between the LED and L1 deviates from $2f_1$ and is adjusted accordingly. The light going out of D1 is collimated by L2, placed at a distance f_2 from D1. The field aperture is placed also at a distance f_2 from L2. The last lens L3 is positioned at a distance f_3 from D2 and focuses the image of D2 into the back focal plane of the objective, placed at a distance f_3 from L3 [102]. The setup used for this work has lenses with focal lengths $f_1 = 25\,\text{mm}$, $f_2 = 50\,\text{mm}$ and $f_3 = 100\,\text{mm}$. The image obtained by the illumination light that hits the sample is viewed through a removable 5 MP CMOS camera (HAYEAR HY-500 B) with a 0.5× magnification lens attached. To direct the outgoing illumination light, a cubical beam splitter is placed between L3 and O, as shown in fig. 4.3. The same beam splitter is used to separate the laser excitation from the sample emission. Hence a 90:10 beam splitter is chosen, so that the loss of PL emission from the sample is minimal (10%). The accordingly low amount of white light reaching the sample is sufficient to clearly see the sample image.

4.2.2 Alternative arrangement and PL setup improvements

A second PL setup was realised as part of this work and, although it remains incomplete and it was not used to obtained the results outlined in this thesis, the differences are described here as they can possibly be used for improvements of the current PL setup. A schematic of the alternative setup is shown in fig. 4.5. The laser beam power is precisely controlled by an optical attenuator, which consists of an input and an output polariser and an intermediate half wave plate. The two polarisers are crossed such that no light would pass through them. However, the presence of the half wave plate, which is mounted on a motorised rotating stage, allows light to pass through and the amount of passing light can be tuned varying the angle of the plate with respect to the optical axis of the incoming polariser. Between the

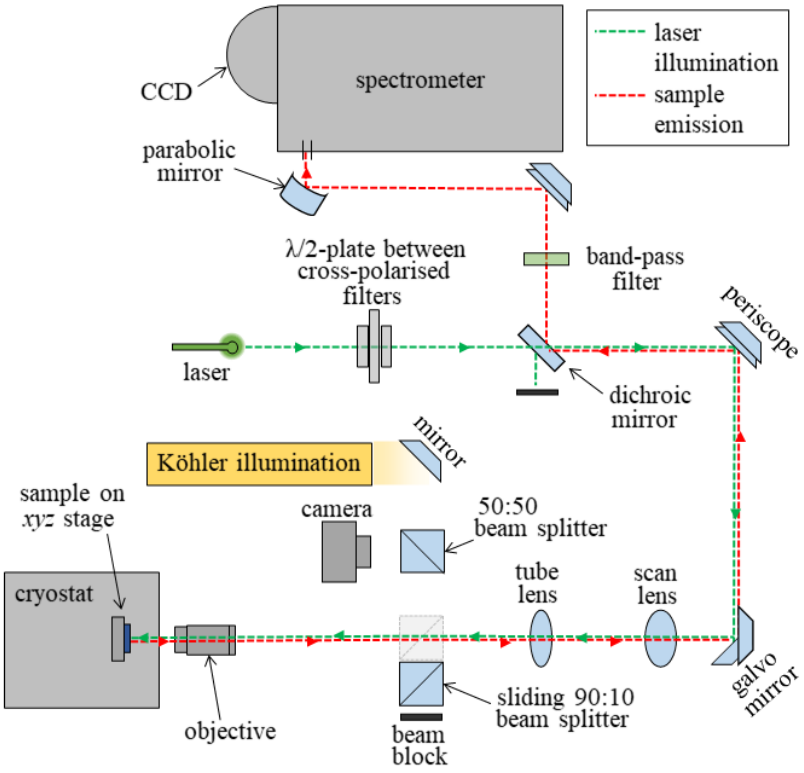

Figure 4.5: Schematic of an alternative PL setup.

laser and the attenuator, a number of mirrors are placed as adjustment aids (not shown in the schematic). A short pass dichroic mirror with 650 nm cut-off wavelength is placed after the attenuator and light with wavelength above the cut-off value is highly reflected whilst the one below this value is highly transmitted. The dichroic mirrors allows the removal of the residual laser light, reflected from the sample, from the signal emitted by the sample. A band-pass filter is also placed closer to the spectrometer. A dichroic mirror as beam splitter allows nearly 100% reflection for wavelengths above the cut-off wavelength, whilst the geometric beam splitter, used in the first setup, allows only 90% reflection, which causes a slight loss of the sample signal. However, with the geometric beam splitter, since a part of the laser light can also pass, the adjustment of the beam path is substantially simplified. A periscope is placed after the filters to adjust the beam height to the spectrometer slit, to which the beam is focused by using an off-axis parabolic mirror. A second periscope directs the beam to the entrance of a galvo mirror. This consists of a dual-axis mirror system, which can be remotely controlled and allows a very precise movement of the beam in the x and y directions over a few tens of micrometers. For point by point galvo scanning of the sample surface, the outbound rays from the galvo mirrors enter a scanning lens which needs to be paired with an infinity-corrected tube lens. This collimates the light into the

back of a ×100 objective. The galvo mirror is the main difference between this setup and the previously described one, where the sample is placed on a piezo-stage for scanning the sample surface. As opposed to using a piezo-stage, the galvo system allows higher precision and faster surface scanning, since larger surface areas can be covered with the mirror system. The piezo-stage is chosen for the first setup due to the demanding alignment process of the galvo system and since further tests indicate that single QDs can be still addressed without the galvo system.

The white light illumination is obtained in an analogous way to the previous setup. However, in this second setup, the 90:10 beam splitter is placed on a motorised stage and can be removed during spectroscopy. In this way, no emission signal is lost from the beam splitter. As a further difference, the camera is away from the laser path; by means of a second beam splitter (50:50), the sample surface and the laser can be observed simultaneously.
The other components and functions are similar to the previously outlined setup.

4.2.3 Setup for room temperature PL

For measurements at and close to room temperature, a commercial Raman microscope is used. The main differences to the previously described setups are briefly reported here.

For microscopy, a Renishaw inVia microscope is used; this has 6 objectives, ×100, ×63, ×50, ×20 and ×10. For the PL measurements, only the ×100 and ×50 objectives are used. The laser spot diameter through these two objectives is 764 nm for the ×100 and 865 nm for the ×50. As a further difference, there is no cryostat in the setup. The samples are placed on a piezo-stage; for measurements close to room temperature, the stage is equipped with a Peltier thermoelectric cooling, with minimum temperature of about 200 K.

4.3 Morphological characterisation

The surface morphology and the structural properties of the QDs studied in this work are obtained with two methods.

The samples where the LDE is performed directly on AlGaAs (samples #1 and #4 - #8) are imaged by AFM (Veeco Dimension 3200). To obtain a QD image, a number of measurements are performed on a sample series in which the fabrication process, with nominally identical process parameters for the growth of each sample in the series, is interrupted after the growth of different successive interfaces. An offset equal to the nominal layer thickness is applied to the baselines of the individual AFM scans to obtain the final image (fig. 2.5a, bottom). Although the so obtained AFM image is helpful to get a rough idea of the QD

shape, it has to be noted that the unfilled and filled nanoholes scanned are taken from different positions of two different samples. This is important to mention in order to avoid misinterpretation.

The samples where an AlAs layer is deposited on AlGaAs before performing the LDE (samples #2 and #3) are imaged with TEM, instead of AFM. This is because, due to the fast oxidation of the AlAs layer, AFM images of QDs in AlAs are not reliable. An example of a TEM image is shown in fig. 2.5b, bottom. The TEM imaging is done in collaboration with Akos Nemcics, using a 300 kV JEOL 3010 high-resolution microscope equipped with a GATAN Tridem model imaging filter [77]. To prepare the sample for the TEM images, thin cross-sections are cut from the sample. After cutting, the specimens are embedded into a holder, grinded mechanically, polished and ion beam etched using 10 keV Ar ions. The different atomic numbers cause contrast in the TEM image, allowing the colour-coding [77]. TEM imaging of the QDs in AlGaAs are not possible due to their lower density.

4.4 Simulation method

The results of the cone-shell (or V-shaped) QDs in electric (F) and magnetic (B) fields are obtained using a single-particle simulation model based on one-band Schrödinger equation in effective mass approximation and cylindrical symmetry. The Coulomb interaction between the charge carriers is then calculated with a first-order correction, without including configuration interaction. The following covers the main steps and the general approach for the computation. A more in-depth theoretical explanation can be found in ch. 3.

Firstly, electron and hole wavefunctions and energy eigenstates are calculated separately in an uncorrelated manner, by solving the single-particle Schrödinger equation $H_j\Psi_j(\vec{r}) = E_j\Psi_j(\vec{r})$ with $j = e$ for electron and h for hole. The single-particle Hamiltonian is derived in ch. 3 and is here rewritten for convenience:

$$\hat{H}_j = -\frac{\hbar^2}{2m_j^*}\vec{\boldsymbol{\nabla}}_j^2 - \frac{i\hbar q_j B}{2m_j^*}\left(y\frac{\partial}{\partial x} - x\frac{\partial}{\partial y}\right) + \frac{q_j^2 B^2}{8m_j^*}(x^2+y^2) - q_j F z + V_j(\vec{r}). \tag{4.1}$$

In the Hamiltonian, the second and third terms account for the presence of the magnetic field $\vec{B} = (0, 0, B)$ applied in the z direction, whilst the fourth term arises from the electric field $\vec{F} = (0, 0, F)$, also applied in the z direction; $V_j(\vec{r})$ is the confinement potential, which is non-zero only in the barrier material. The solutions to the Schrödinger equation are calculated by numerically solving the partial differential equation with the finite element method (FEM), using the software COMSOL Multiphysics. For the computation, the following formula,

deriving by expressing eq. 4.1 in terms of the magnetic quantum number l_j, eigenvalue of the operator $\mathbf{L_z}$ (see also eq. 3.18), is used as input to a COMSOL module:

$$c_j\left(\frac{l_j}{r}\right)^2 - \frac{\hbar q_j B l_j}{2m_j^*} + \frac{q_j^2 B^2 r^2}{8m_j^*} - q_j F z + V_j(\vec{r}); \tag{4.2}$$

here c_j is a constant. The COMSOL module iterates eq. 4.2 up to the required quantisation level number n_j.

Once the single particle energy eigenvalues $E_{j,n}$ and the corresponding wavefunctions $\Psi_{j,n}(\vec{r}_j)$ are obtained for both electrons and holes, the wavefunctions can be used to calculate the Coulomb integral eq. 3.2. For the scope of this thesis, only the ground state behaviour is of interest, hence the Coulomb interaction is obtained by using the ground state wavefunctions $\Psi_{h,0}(\vec{r}_h)$ and $\Psi_{e,0}(\vec{r}_e)$ as input to eq. 3.2.

For further information about the exciton recombination, the overlap integral, given by

$$I_{eh} = \left| \int_V \Psi_{e,0}(\vec{r})\Psi_{h,0}(\vec{r})\, d\vec{r} \right|^2 \tag{4.3}$$

can then be numerically calculated and used to compute the ground state radiative lifetime

$$\tau = \frac{12\pi\hbar^2 c^3 \epsilon_0 m_0}{n_{QD} e^2 (E_{e,0} + E_{h,0} + E_g) E_P I_{eh}} \tag{4.4}$$

with c the speed of light, m_0 the electron rest mass, $E_{e,0}$ and $E_{h,0}$ the electron and hole ground state energies, E_g the bandgap energy and n_{QD} and E_P the material specific refractive index and Kane energy, which are 3.52 [103] and 25.7 eV [104] for GaAs respectively. The accuracy of the approach and the model is discussed in ch. 7 in relation to the results.

Unless otherwise stated, the simulations are performed using the following structural parameters, as indicated in fig. 4.6: nanohole depth $h_{out} = 30\,\text{nm}$, nanohole opening radius $R_{out} = 56.5\,\text{nm}$, QD height $h_{in} = 7.05\,\text{nm}$ and indentation radius $R_{in} = 49.4\,\text{nm}$. These

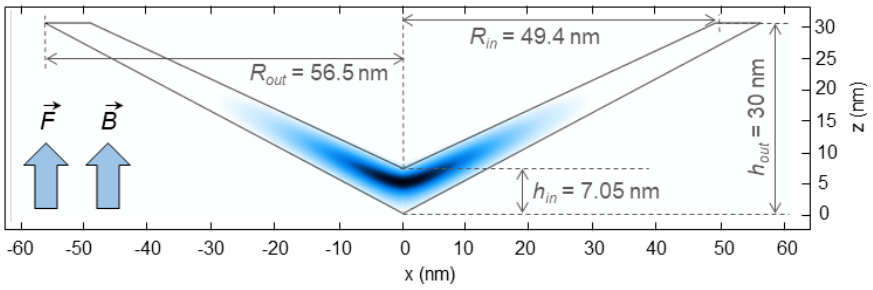

Figure 4.6: Schematic of the cone-shell QD. The dimensions used for the simulations are indicated along with the direction in which the electric and magnetic fields are applied.

parameters are chosen based on the AFM images of the cone-shell QDs (fig. 2.5a, bottom), taking into account the amount of filling material deposited. The values for the electron and hole effective masses are $m_e^* = 0.067m_0$ and $m_h^* = 0.51m_0$ in the QD and $m_e^* = 0.09m_0$ and $m_h^* = 0.6m_0$ in the AlGaAs barrier. The confinement potential for both charge carriers is 0 in the QD and $V_e = 300\,\mathrm{meV}$ and $V_h = 177\,\mathrm{meV}$ for electrons and holes in the barrier (these correspond to band discontinuities in $Al_{0.32}Ga_{0.68}As$ [105]).

Chapter 5

QD at and close to room temperature

Semiconductor QDs open the possibility for a variety of interesting devices, but the commercial use of these is often hindered by the effect of ambient temperature. In this chapter, the photoluminescence from three QD samples (samples #1, #2 and #3) is measured, first at low temperature and then at and close to room temperature (T_R). For one of the samples, which is optimised for T_R emission, a simple model is proposed to evaluate the mechanism behind the reduction in the PL intensity with increasing temperature. The analysed PL data are taken by illuminating the samples with a laser with wavelength 532 nm (green laser). In a second step, to study the influence of the laser energy on the PL emissions, the spectra are also taken by exciting the dots with a blue laser of wavelength 405 nm. The laser spot diameter is about 0.5 µm^2 for all the measurements outlined in this chapter.

5.1 PL characteristics at low temperature

The luminescence at cryogenic temperatures is here briefly outlined as a basis for comparisons with the results at higher temperatures, described in the next sections. PL spectra taken at a laser power of 0.2 µW are shown in fig. 5.1a for QDs of different size. The size of the QDs is here indicated by the GaAs filling layer thickness d_F. The shift in energy towards lower values is observed as the QDs increases in size, which is a direct consequence of the lower confinement. In the inset, a zoom-in of the PL emission of the QD with $d_F = 0.45$ nm is shown, where the X and XX peaks can be clearly distinguished. The line-width is of 49 µeV, which is at the resolution limit of the spectrometer used for the measurements, and the fine-structure splitting is of about 5 µeV [106].

When increasing the power from 0.2 µW to 10 µW, higher states of the QDs are filled. Thus, the X and XX peaks are not visible and, instead, the QD shell structure can be observed

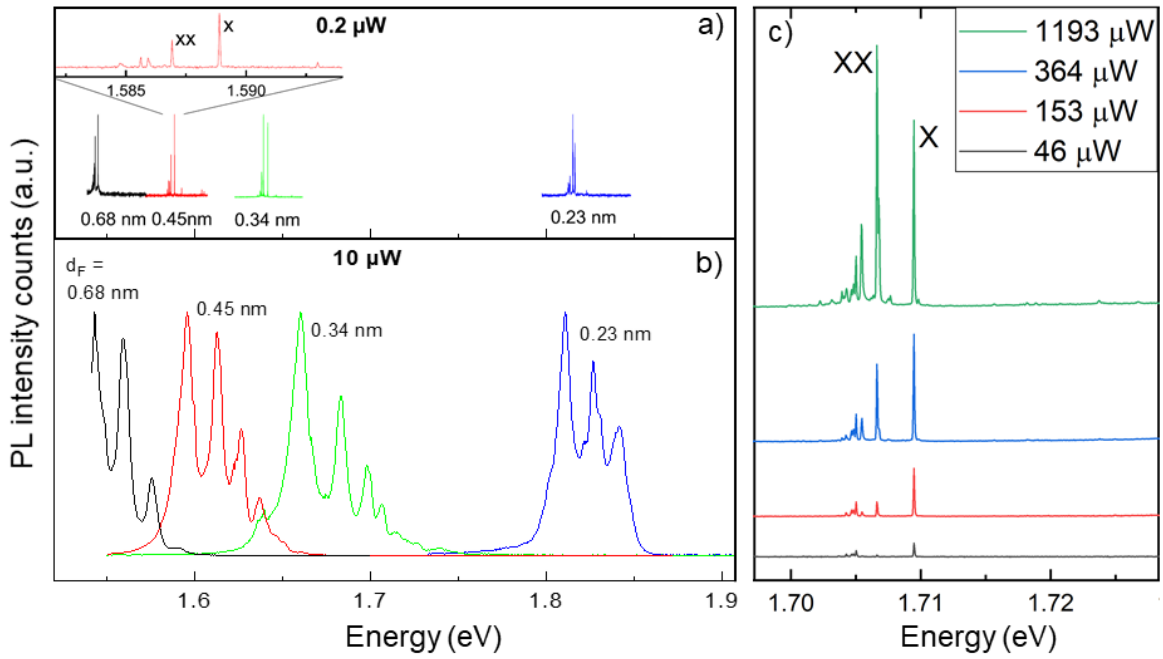

Figure 5.1: (a) PL measurements taken at about 8 K of QDs of different sizes, as indicated by the GaAs filling layer thickness d_F taken at 0.2 µW and (b) at 10 µW. The inset in (a) shows a zoom-in of the PL spectrum of a QD with $d_F = 0.45$ nm, where X and XX peaks are indicated. In (b) the QD shell structure is visible. (c) PL emission, taken at 3.6 K, from a single QD of sample #1, taken at four different powers; the X and XX peaks are indicated.

(fig. 5.1b).

PL spectra of sample #1 at 3.6 K are shown in fig. 5.1c for four different power values. Analysing the power dependence of the PL emissions helps to assign the peaks to the correct recombination process, as explained in ch. 3. The peak that initially appears at low power (46 µW, black line) is the X emission, since the exciton is the complex with the lowest number of particles involved. Further increasing the power to 153 µW (red line), and thus increasing the exciton generation rate, the probability of further particles occupying the QD also increases, leading to the presence of other peaks. Among these, the XX peak can be identified considering the rate model predictions outlined in ch. 3. The peak assigned to the XX is the one strongly increasing in intensity when reaching 364 µW (blue line) and which overpasses in intensity the X peak when the power is further increased to 1193 µW. The other peaks can be associated to trions.

5.2 Strong GaAs background

The PL measurements of sample #1 at cryogenic temperature ($T = 8\,\mathrm{K}$) are shown in fig. 5.2a. Sharp and clear excitonic and biexcitonic peaks, with linewidth of about 50 µeV, are visible at low-excitation power of 0.2 µW (inset). Increasing the excitation power to 10 µW, the ground state and three excited states of the single-dot PL are distinguishable, as a consequence of the filling of higher QD energy levels. The increase in linewidth, with respect to the low-power spectrum, is associated to the formation of multiexcitonic complexes. At low temperature, it can be noted that no GaAs background is observed.

The recombination of the ground state exciton is observed at $E_0(8\,\mathrm{K}) = 1.642\,\mathrm{eV}$ (inset in fig. 5.2a). Using eq. 3.12, the GaAs bandgaps at higher temperatures are estimated as $E_g(200\,\mathrm{K}) = 1.469\,\mathrm{eV}$ and $E_g(300\,\mathrm{K}) = 1.430\,\mathrm{eV}$. Using the bandgap values and considering eq. 3.23 for the ground state ($n = 0$), which reads

$$E_0(T) = E_g(T) + E_{e,0} + E_{h,0} - C_{eh,0}, \tag{5.1}$$

gives the ground state quantisation energy $E_0(T) - E_g(T) = 0.125\,\mathrm{eV}$ and the expected ground state emission energies $E_0(200\,\mathrm{K}) = 1.594\,\mathrm{eV}$ and $E_0(300\,\mathrm{K}) = 1.555\,\mathrm{eV}$ are obtained.

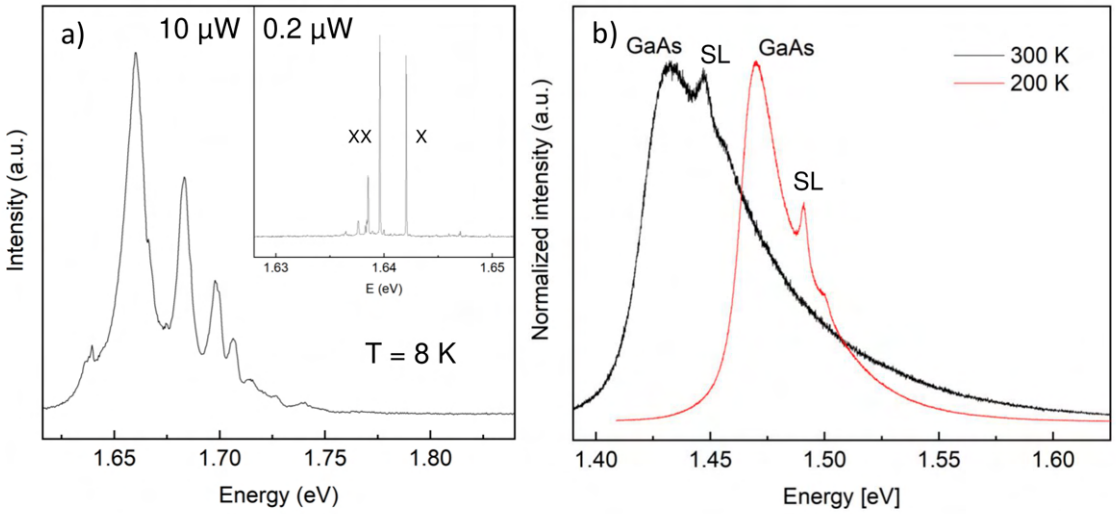

Figure 5.2: PL emission from sample #1 obtained by excitation through a 532 nm green laser. (a) Single-dot emission at $T = 8\,\mathrm{K}$ with 10 µW laser power; inset: single QD PL emission at 0.2 µW excitation power, with indicated exciton (X) and biexciton (XX) peaks. (b) Normalised PL emission at T_R (black) and 200 K (red) with 0.06 mW excitation power. The peaks from the GaAs substrate and the superlattice (SL) are indicated.

Measurements at and close to room temperature T_R are shown in fig. 5.2b. These are taken for a sample area of $8 \times 8\,\mu m^2$, scanned in steps of 500 nm. The sample has a QD density of $2 \times 10^7\,cm^{-2}$, thus, within the scanned area, an average of 13 QDs are expected. All the scanned fields show similar PL emissions, with a strong asymmetric and broad peak and a second sharper peak at around 21 meV at 200 K and 16 meV at 300 K. Both at T_R and close to T_R and for all scan fields, no peak is visible in correspondence to the energy at which QDs are expected to emit.

The sharper peak in fig. 5.2b can be associated to quantised states in the AlAs/GaAs superlattice (SL). The first undesired peak observed at high temperatures is caused by the GaAs substrate, as confirmed by the peak maxima at about 1.47 eV at 200 K and 1.43 eV at 300 K. PL measurements taken at 230 K and 300 K from a GaAs wafer (fig. 5.3) give a better insight into the peak characteristics. The very broad emission has a strong high-energy tail that increasingly broadens with increasing temperature. This tail, which is an indication of the thermal population of high-energy states (band-to-band recombination of free carriers) [107], heavily interferes with possible emissions from QDs at the expected energy. Moreover, it can be observed that, as the temperature rises, the GaAs PL intensity decreases, which is explained by the increasing importance of thermally activated non-radiative recombination processes [108].

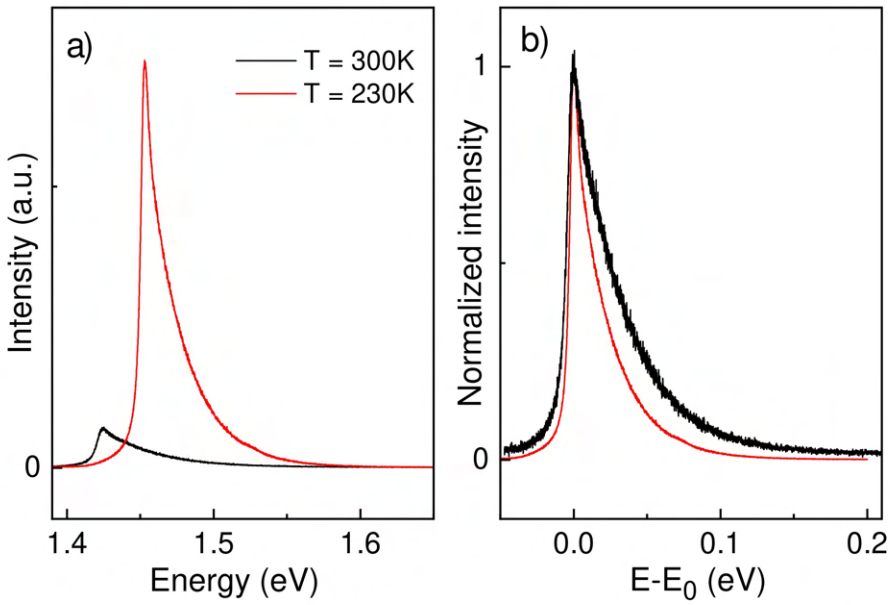

Figure 5.3: (a) PL emission spectra from a GaAs wafer at T_R (black) and at 230 K (red) taken with a 532 nm green laser. (b) Normalised GaAs PL intensity as function of the difference between emitted energy and GaAs bandgap energy.

5.2.1 Temperature enhanced excitonic emission intensity

Although at and close to room temperature not much information can be obtained about sample #1 QDs, measurements at temperatures below 90 K can still give interesting insights. As observed in the inset of fig. 5.2a, this sample shows sharp excitonic peaks at cryogenic temperatures. Here, an analysis of the temperature dependence of the excitonic PL emission intensity is presented and the resulting plot is shown in fig. 5.4, normalised to the intensity $I_{X,0}$ at 3 K.

The QDs in sample #1 are placed at a distance $d_{QD} = 80\,\text{nm}$ from the sample surface (fig. 4.1a). When illuminating the sample with a laser, the density of excited excitons at the surface is $n_0 = c_E P_E$, with c_E a constant and P_E the laser power. From Beer-Lambert law [109], the density of excitons in the QD layer excited by the laser is $n_E = n_0 e^{-\alpha d_{QD}}$, with α the absorption coefficient. For a green laser (532 nm) and for AlGaAs with an Al content of 31.5%, $\alpha = 5.59 \times 10^4\,\text{cm}^{-1}$, which leads to a density ratio $n_E/n_0 = 0.64$. This process is temperature independent. As can be observed in fig. 5.4, at temperatures below 15 K, the intensity is almost temperature independent and the QD emission can be associated to direct QD excitation by the laser. Hence, it can be assumed that only the absorption is influencing the exciton emission intensity at low temperatures.

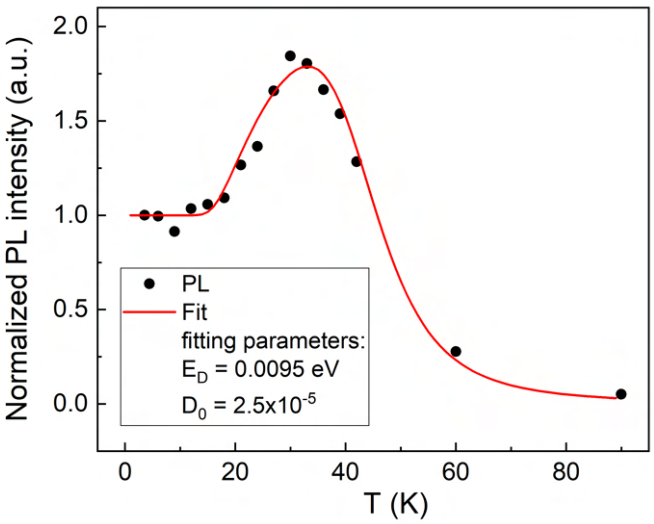

Figure 5.4: Exciton PL intensity as function of temperature, normalised with the intensity at $T = 3\,\text{K}$. Experimental data are indicated with black points whilst the red line is a fit to the data, with fitting parameters as indicated.

As the temperature exceeds 15 K, the exciton intensity ratio $I_{norm} = I_X/I_{X,0}$ (with I_X the exciton emission intensity) increases, reaching a maximum at about 30 K, where $I_{norm} = 1.85$. The increase in intensity can be explained by the additional contribution of excitons diffusing from the AlGaAs barrier into the QDs. In equilibrium conditions and assuming constant illumination, the exciton density at the QD layer is $n_D = n_0 e^{-d_{QD}/L_D}$, with the diffusion length $L_D = \sqrt{D\tau_X}$, where D is the diffusion coefficient and τ_X the exciton recombination lifetime. If an activated transport is assumed, the diffusion coefficient is given by $D = D_0 e^{-E_D/k_B T}$, where D_0 is a constant which indicates the maximal diffusion coefficient in the limit of infinite temperature and E_D is the exciton diffusion activation energy. This ansatz is also used in similar earlier work about temperature dependent luminescence in indirectly excited GaAs quantum wells [110]. The total density of excited excitons inside a QD is $n_E + n_D$, which is temperature dependent due to the temperature dependence of D and thus of n_D. The increase of I_X with increasing temperature in the range $15\,\mathrm{K} < T < 30\,\mathrm{K}$, can thus be explained by the increase of the diffusion coefficient and, consequently, of the diffusion length L_D as the function of the temperature.

The maximum intensity, reached at about 30 K, can be associated to a saturation point of n_D, obtained when $L_D \simeq d_{QD}$, which is indeed the case for the fitting line in fig. 5.4. As L_D exceeds d_{QD}, for temperatures above 30 K, the complete AlGaAs barrier above the QDs provides excitons to the QDs and no further excitons diffuse into the QD by further increasing the diffusion length. This, however, would be expected to cause the intensity to remain invariant. Instead, the intensity drops above this point, which can be associated to thermally activated processes, such as exciton break in the AlGaAs barrier and the escape of single charge carriers from the QD. These processes are analysed in sec. 5.4.1 in reference to sample #3.

5.3 QD signal close to room temperature

To increase the QD signal and decrease the GaAs background which interferes with the QD emission in sample #1, various modification are considered in the fabrication of sample #2. Firstly, the QD density is increased from $2 \times 10^7\,\mathrm{cm}^{-2}$ to $4 \times 10^8\,\mathrm{cm}^{-2}$ by adding an AlAs layer on the AlGaAs barrier where the Al droplets are deposited for the nanoholes formation. Due to this layer, the surface diffusion of the Al adatoms is reduced, leading to a higher number of droplets and thus of QDs [111]. Moreover, both the thickness and the Al content of the AlGaAs barrier layer are increased, from 200 nm to 320 nm and from 33% to 37% respectively, and the (Si)GaAs back gate is removed.

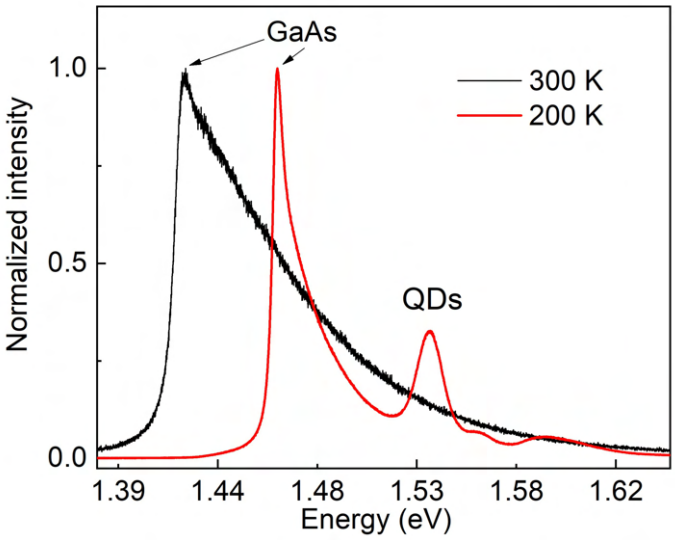

Figure 5.5: PL emission from sample #2 obtained by excitation through a 532 nm green laser. Normalised PL emission at T_R (black) and 200 K (red) with 0.06 mW excitation power. At 200 K, the emission from the QD ensemble is visible.

From the PL spectrum of sample #2 taken at $T = 4\,\mathrm{K}$ (not shown here), the QD ground state is measured to be $E_0(4\,\mathrm{K}) = 1.578\,\mathrm{eV}$. Hence, using eqs. (3.12) and (5.1), the QD ground state emission energies $E_0(200\,\mathrm{K}) = 1.529\,\mathrm{eV}$ and $E_0(300\,\mathrm{K}) = 1.490\,\mathrm{eV}$ are expected. The PL emission at room temperature T_R (fig. 5.5, black line) shows still a strong GaAs background peak and no QD signal for most scanned areas of the sample. For a few scanned spots, the PL measurements (not shown here) present a weak QD signal, which could be related to a locally higher QD density. It can thus be inferred that, at T_R, the emission from sample #2 is just below the threshold of QD visibility. Lowering the temperature to 200 K (fig. 5.5, red line), indeed a clear QD peak becomes visible at $E_0(200\,\mathrm{K}) = 1.534\,\mathrm{eV}$ for all scanned fields. The slight difference of 5 meV between the expected and actual emission energy value can be related to the QD size uniformity throughout the wafer. Two weak shoulders are also noticeable around 1.558 eV and 1.590 eV, which can be attributed to the first and second excited states.

5.4 Strong QD signal at room temperature

Sample #3 is specifically made to maximise the QD emission at room temperature. To do so, a thicker AlGaAs barrier (over 2.8 µm) is grown to avoid the GaAs background emission and the LDE and QD fabrication are repeated five times with identical parameters, hence obtaining five stacked layers of QDs and thus strengthening the ensemble emission.

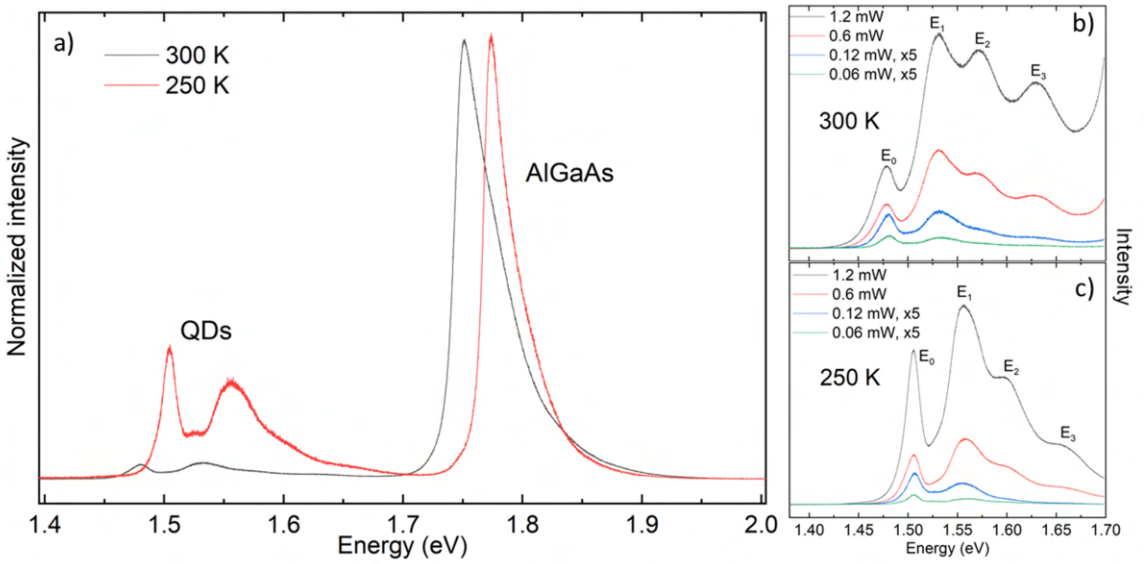

Figure 5.6: PL emission spectra from sample #3 obtained by excitation through a 532 nm green laser. (a) PL emission at T_R (black) and at 250 K with 0.06 µW excitation power; a strong QD ensemble signal is visible. (b) Zoom of QD ensemble emission at T_R and at (c) 250 K for various laser powers, as indicated.

The PL emission from sample #3 at T_R (fig. 5.6a), as a result of these improvements, shows no GaAs background. Furthermore, a strong AlGaAs peak is visible at $E = 1.75$ eV, from which an Al concentration of 22.3% is determined, but this peak is well-separated from the QDs' emission energy from 1.4 eV to 1.7 eV and thus does not interfere with it.

Power-dependent PL measurements at T_R (fig. 5.6b) show a strong ground state emission (1.479 eV) and three excited states (1.531 eV, 1.574 eV and 1.632 eV) at high excitation power of 1.2 mW. A reduction of the excitation power causes a gradual decrease of the emission intensity, in particular for high energy levels, which is explained by the diminution of the charge carriers in higher states. It can also be observed that at low power (0.06 mW), the ground state E_0 peak intensity is stronger than the first excited state E_1 peak intensity. As the power is increased above 0.12 mW the ground state emission is overtaken firstly by the first excited state and subsequently also by higher excited state peaks. This can be explained by considering the Pauli exclusion principle: the ground state can be occupied only by two electrons whilst the first excited state allows for four electrons. At a power for which both levels are likely occupied, the possibility of the first excited state being occupied by more electrons than the ground state is reflected by the higher intensity of the E_1 peak with respect to the E_0 peak. The same argument holds for the higher excited states.

Similar power-dependent PL measurements are taken at $T = 250\,\mathrm{K}$ (fig. 5.6c). The plot behaviour is analogous to the one at room temperature. It can however be observed that, lowering the temperature from 300 K to 250 K, the QD emissions become sharper and are blue-shifted by about 27 meV, reflecting the GaAs bandgap temperature-dependent shift from 1.430 eV at 300 K to 1.450 eV at 250 K (eq. 3.12, sec. 3.2.2).

5.4.1 Intensity reduction mechanism at high temperature

The QD PL emissions at and close to room temperature, normalised to have the same AlGaAs peak intensity maximum, are shown in fig. 5.6a. Even with the normalisation (which enhances the emission at T_R), it is evident that the emission intensity is strongly reduced at T_R.

To understand the mechanism behind this intensity loss, it is useful to calculate the quantisation energies inside the QD. For this estimation, the 3D Fock-Darwin model, describe in sec. 3.2.4.1, is used [100]. Although the model considers an idealised case of a spherical dot with parabolic confinement, which is not expected to be the case in the present system, it is here used for its simplicity and for a first rough estimation. Furthermore, the exciton binding energy is here assumed to be independent of the principal quantum number n ($C_{eh,n} = C_{eh}$). This choice is also made in order to further simplify the model. From eqs. (3.21) and (3.23), the energy difference between the first excited state and the ground state and between the ground state and the bandgap edge are $E_1 - E_0 = \hbar(\omega_e + \omega_h)$ and $E_0 - E_g = \frac{3}{2}\hbar(\omega_e + \omega_h)$ respectively, which lead to the binding energy $C_{eh} = E_g - \frac{5}{2}E_0 + \frac{3}{2}E_1$. Its numerical value, $C_{eh} = 23\,\mathrm{meV}$, is obtained plugging-in the experimental energy results E_n at room temperature summarised in Table 5.1. The corresponding oscillator length, $L \simeq 10\,\mathrm{nm}$ gives an estimation of the order of magnitude of the QD diameter. This value is similar to the one observed in the morphological images of sample #3 QDs (fig. 2.5b, bottom). The experimental PL data can be used in eqs. (3.24) and (3.25) to find the n^{th}-level electron and hole quantisation energies (Table 5.1 and fig. 5.7b).

To better understand the cause of the PL intensity drop with increasing temperature, the integrated ground state PL intensity is measured as function of the temperature, from 40 K up to 300 K, at a constant excitation power of 2 µW. Three distinct regimes can be noticed: a low-temperature regime from 40 K to 100 K, a transition regime from 100 K to 160 K and a high-temperature regime above 160 K (fig. 5.7a). The slope of the logarithmic intensity plot as function of the temperature gives the activation energies, assuming that the processes causing the intensity reduction are thermally activated.

Level, n	0	1	2	3
E_n	1479	1531	1574	1632
$E_n - E_{n-1}$	-	52	43	58
$E_{e,n}$	69	114	152	203
$E_{h,n}$	9	16	21	28
Exciton escape				
$E_{X,esc}$	254	202	159	101
Single charge escape				
$E_{e,esc}$	163	118	80	29
$E_{h,esc}$	137	130	125	118

Table 5.1: Measured PL energies E_n for QD sample type III at $T_R = 300\,\mathrm{K}$. Calculated electron and hole quantisation energies and escape energies. All energy values are in meV.

The red line in fig. 5.7a is based on a rate model. The QD emission intensity is

$$I_{PL} = N_{QD} R_{PL} \tag{5.2}$$

where N_{QD} is the population of excitons in the QD and $R_{PL} = \frac{1}{\tau_{PL}}$ is the exciton radiative recombination rate in the QD, with radiative lifetime τ_{PL}. The exciton population in the QD changes in time as

$$\frac{dN_{QD}}{dt} = N_B R_{cap} - N_{QD} R_{esc} - N_{QD} R_{PL} \tag{5.3}$$

with N_B the population of excitons in the barrier, R_{cap} the rate at which an exciton in the barrier is captured by the QD, and R_{esc} the rate at which an exciton thermally escapes from the QD into the barrier material. The time-dependent exciton population in the barrier is

$$\frac{dN_B}{dt} = R_E - N_B R_{br} \tag{5.4}$$

with R_E the rate at which excitons are generated by the laser irradiation (laser intensity) and R_{br} the rate at which an exciton thermally breaks. When the population is constant (i.e. in equilibrium, when $t \to \infty$), $\frac{dN_{QD}}{dt} = 0$ and hence, from eq. 5.3, the exciton population in the QD is $N_{QD} = \frac{N_B R_{cap}}{R_{esc}+R_{PL}}$. Since the time-dependence of N_B at constant illumination is also 0 $\left(\frac{dN_B}{dt} = 0 \right)$, thus from eq. 5.4 follows that $N_B = \frac{R_E}{R_{br}}$. Hence

$$N_{QD} = \frac{R_E R_{cap}}{R_{br}(R_{esc} + R_{PL})}. \tag{5.5}$$

From eq. 5.2, the optical intensity emitted from a QD becomes

$$I_{PL} = \frac{R_E R_{cap} R_{PL}}{R_{br}(R_{esc} + R_{PL})}. \tag{5.6}$$

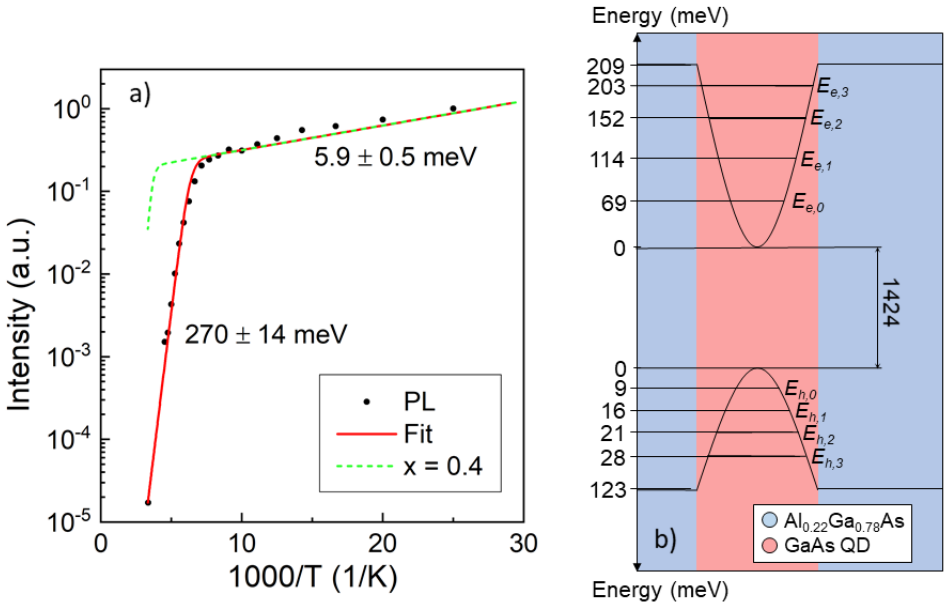

Figure 5.7: (a) Measured PL ground state emission intensities (dots) from sample #3 at different temperatures, together with model results using the indicated activation energies considering an Al content of 22% (red) and 40% (dashed green). (b) Schematic of the conduction and valence band at the interface between GaAs QD (red) and the AlGaAs barrier (blue). All the indicated energy values are in meV.

Assuming that R_{br} and R_{esc} are thermally activated rates whilst R_E, R_{cap} and R_{PL} do not depend on the temperature, eq. 5.6 simplifies to

$$I_{PL} \propto \frac{1}{R_{br}(R_{esc} + R_{PL})}. \tag{5.7}$$

The temperature dependent activation rates can be written as $R_{br} = \nu_{br} \exp(-E_{A1}/k_B T)$ and $R_{esc} = \nu_{esc} \exp(-E_{A2}/k_B T)$, with ν_{br} and ν_{esc} the vibrational frequencies and E_{A1} and E_{A2} the activation energies.

Using a typical lifetime of $\tau_{PL} = 1\,\text{ns}$ to calculate R_{PL}, the activation energies $E_{A1} = 5.9\,\text{meV}$ and $E_{A2} = 270\,\text{meV}$ for the low- and high-temperature regimes, respectively, give the model results (red line in fig. 5.7a) that best fit the experimental results, and are thus used for the analysis that follows. By using a different value for the lifetime, such as $\tau_{PL} = 10\,\text{ns}$ or $\tau_{PL} = 100\,\text{ps}$, the activation energies vary of only about 8%, which is here considered to be small.

The exciton binding energy in GaAs bulk material is 4.7 meV, which is close to E_{A1}. This can indicate that, in the low-temperature regime, a thermally activated process breaks the excitons excited by the laser in the AlGaAs barrier material and the deriving single charge

carriers diffuse separately through the crystal.

A number of possible loss channels can be linked to the higher activation energy E_{A2} at temperatures above 160 K. The most likely of these are exciton escape and single charge escape from the QD.

In the first case, an electron and a hole bound to each other escape from the dot into the AlGaAs barrier as an exciton. The escape energy is then $E_{X,esc} = \Delta E_c - E_{e,n} + \Delta E_v - E_{h,n}$, with ΔE_c the band discontinuity at the AlGaAs/GaAs interface for the conduction band and ΔE_v for the valence band. For an AlGaAs barrier with an Al content of $x = 0.223$, the band discontinuities are $\Delta E_c = 209\,\text{meV}$ and $\Delta E_v = 123\,\text{meV}$ [105].

In the other most likely mechanism, the Coulomb binding energy between the electron and the hole forming the exciton in the QD is first broken and then one charge carrier escapes the QD singularly into the conduction band or the valence band. The escape energies are thus $E_{e,esc} = \Delta E_c - E_{e,n} + C_{eh}$ and $E_{h,esc} = \Delta E_v - E_{h,n} + C_{eh}$ for electrons and holes respectively.

Comparing E_{A2} to the different escape energies summarised in Table 5.1, the escape of ground state excitons ($E_{X,esc} = 254\,\text{meV}$) is the mechanism that can best describe the intensity loss of the high-temperature regime. This result is in agreement with similar studies performed on InAs QDs [112, 113] and on self-assembled GaAs QDs comparable to the ones in sample #3 [94].

A way to partially overcome the exciton escape from the QDs is by raising the AlGaAs barrier. This is shown by the green line in fig. 5.7a, which illustrates the QD PL emission intensity predicted by the above described model for a higher Al content of 40%, the maximum reasonable content that would still allow not having an indirect band structure. The QD PL intensity is predicted to increase by more than three orders of magnitude.

5.5 Influence of laser energy

The PL emissions discussed in the previous sections are taken by illuminating the samples with a green laser (532 nm). In this case, the emissions at and close to room temperature from samples #1 and #2 are strongly affected by the GaAs background signal. A possible way to increase the ratio I_{QD}/I_{GaAs} between the QD and the background emissions, is to excite with a blue laser (405 nm).

The absorption coefficient α is wavelength dependent and, using values close to sample #1

as an example, for an AlGaAs barrier material with an Al content of 31.5% is $\alpha_{blue} = 4.19 \times 10^4\,\mathrm{cm}^{-1}$ and $\alpha_{green} = 5.59 \times 10^5\,\mathrm{cm}^{-1}$ when using a blue (405 nm) and a green laser (532 nm), respectively [114]. In sample #1, the plane containing the QDs is at a depth $d_{QD} \simeq 80\,\mathrm{nm}$ from the surface, hence in between the penetration depths of the blue and green lasers. This leads to a ratio between blue and green excitation intensities of $I_{blue}/I_{green} = 5 \times 10^{-2}$. The interface between the AlGaAs barrier and the GaAs is at a depth $d_{GaAs} = 200\,\mathrm{nm}$, which gives $I_{blue}/I_{green} = 7 \times 10^{-4}$. Hence, although the blue laser is expected to lead to a lower QD intensity as opposed to the excitation through a green laser, due to the shorter penetration depth of 24 nm as opposed to the 179 nm penetration depth of the green laser, it is also expected to suppress the background emission by a factor of about 70, if other effects, such as exciton diffusion, are neglected.

The PL measurements resulting from the blue laser excitation of sample #1 (fig. 5.8a and b) confirm the expectations. Compared to the excitation with the green laser (fig. 5.2b), the GaAs background peak is not visible. Both at 300 K and 200 K, the SL and the AlGaAs barrier peaks are visible. These are also visible when using a green laser (fig. 5.2b). As most improvement with respect to the green laser case, the QD ground state energy peak is observed at 300 K. Its value $E_0 = 1.540\,\mathrm{eV}$ is close to the energy 1.555 eV expected from the low-temperature data of the sample with 532 nm excitation discussed in sec. 5.2. At

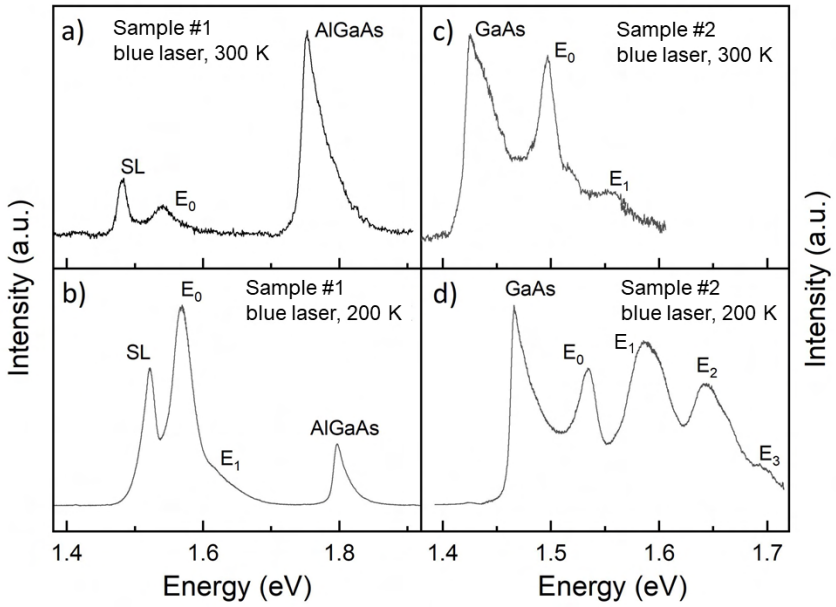

Figure 5.8: PL emissions from sample #1 and #2 obtained by excitation through a 405 nm blue laser. (a) Sample #1 at T_R, (b) sample #1 at $T = 200\,\mathrm{K}$, (c) sample #2 at T_R and (d) sample #2 at $T = 200\,\mathrm{K}$.

200 K, the increased emission intensity reveals also a shoulder which might indicate the QD first excited state.

The PL spectra from sample #2 (fig. 5.8c and d) also show major improvements when using a blue laser: already at room temperature, the QD ground state emission is visible and becomes clear at $T = 200\,\mathrm{K}$. The energies, $E_0 = 1.495$ for $T = 300\,\mathrm{K}$ and $E_0 = 1.530$ for $T = 200\,\mathrm{K}$, agree well with the estimation in sec. 5.3. The first excited state is also already visible at 300 K and, at 200 K, with the same excitation power, 3 excited states can be distinguished. The GaAs background, although still present, is reduced by a factor larger than 6000 in comparison to the green laser excitation case.

The PL measurements of sample #3 with the blue laser (not shown) do not present any emission from QDs, which can be explained by the very thick and hence highly absorbing AlGaAs barrier layer, appositely grown for increasing the emission when exciting with a green laser.

5.6 Summary

The influence of the temperature on the optical properties of LDE QDs is analysed in this chapter. As the temperature increases, the QD optical emissions are observed to becomes broader, as a consequence of exciton-phonon coupling phonon scattering [97]. Furthermore, the QD emission peaks move to smaller energy values due to the GaAs bandgap shrinkage caused by the atomic vibrations becoming stronger with increasing temperature [94].

The temperature dependence of the QD PL intensity is also investigated. It is shown that, at temperatures below about 15 K, the intensity is nearly temperature independent, which indicates that the emission is obtained only through direct excitation of the QD by absorption at or in very close vicinity to the QDs. Between 15 K and 30 K, an enhancement of the PL intensity is observed, which is associated to diffusion of excitons from the AlGaAs barrier into the QD, which contributes to the overall intensity. At about 30 K, where the diffusion length and the distance of the QD layer from the sample surface are expected to be equal, the intensity starts dropping and thermally activated loss channels come into play. These loss channels are studied through a rate model, which indicates a low- and a high-temperature regime. In the former ($T < 100\,\mathrm{K}$), the break of excitons excited by the laser in the barrier material and the consequent single charge carrier separate diffusion through the crystal are considered to be the main loss channels. In the high-temperature regime (above 160 K), the most likely loss channel is the escape of ground state excitons from the QD.

Chapter 6

Cone-shell QD in electric field F

When an external electric field F is applied on a QD, the electrostatic energy of the electrons and holes in the QD is altered. This causes the recombination energies to be shifted as a result of the quantum-confined Stark effect [79, 115–117] and the electrons tunnelling probability to change. These effects are here investigated on QDs which are referred to as cone-shell QDs (samples #4 to #8), as they result in the shell of a cone, as shown in fig. 4.6. Thanks to the particular shape of these QDs, allowed by the LDE method, as opposed to other more common shapes like pyramidal [118] and spherical [119] shapes, an external electric field applied parallel to the QD growth direction is expected to induce the formation of either an electron or a hole ring at the base (top) of the cone-shell structure, as a consequence of the charge carrier separation and the confinement regime. Hence, here an electric field applied in the growth direction also causes a lateral separation of the wavefunctions.

In this chapter the model described in ch. 4 is firstly used to simulate the electron and hole wavefunctions for various F values and to predict the QD PL measurements by computing the single-particle ground state energies and the Coulomb interaction. Secondly, electric field dependent measurements are provided and compared to the theoretical results.

6.1 Simulation predictions

In order to predict the behaviour of the charge carriers of a cone-shell QD under the influence of an external F, simulations are performed, firstly in the single-particle frame and, as a second step, the Coulomb interaction is included as a perturbation. The calculations are performed without considering configuration interaction (CI) to avoid extensive computation times. The purpose here is to obtain rough predictions of experimental outcomes, rather than to make a precise theoretical model. Thus a simple approach, albeit approximated, is preferred to a more precise and complex one.

6.1.1 Single-particle frame

For the study of the structure in the single-particle frame, without interaction, the simulation of the wavefunction and the corresponding energy eigenvalues is computed separately for electron and hole. The effect of an electric field F, applied from bottom to top (fig. 4.6), can be understood by analysing the change in the probability density of the charge carriers, which is shown in fig. 6.1. The left and right columns show the cross-section of the electron and hole ground state square wavefunctions $\Psi^2_{e,0}$ and $\Psi^2_{h,0}$ respectively, with the white colour being where it is most probable to find the corresponding charge carrier, blue where it is less likely and black where it is very unlikely to be found. When no electric field is applied (fig. 6.1c and h), both electron and hole are at the tip of the cone-shell. Due to its smaller effective mass, the electron has a higher probability density in the barrier material

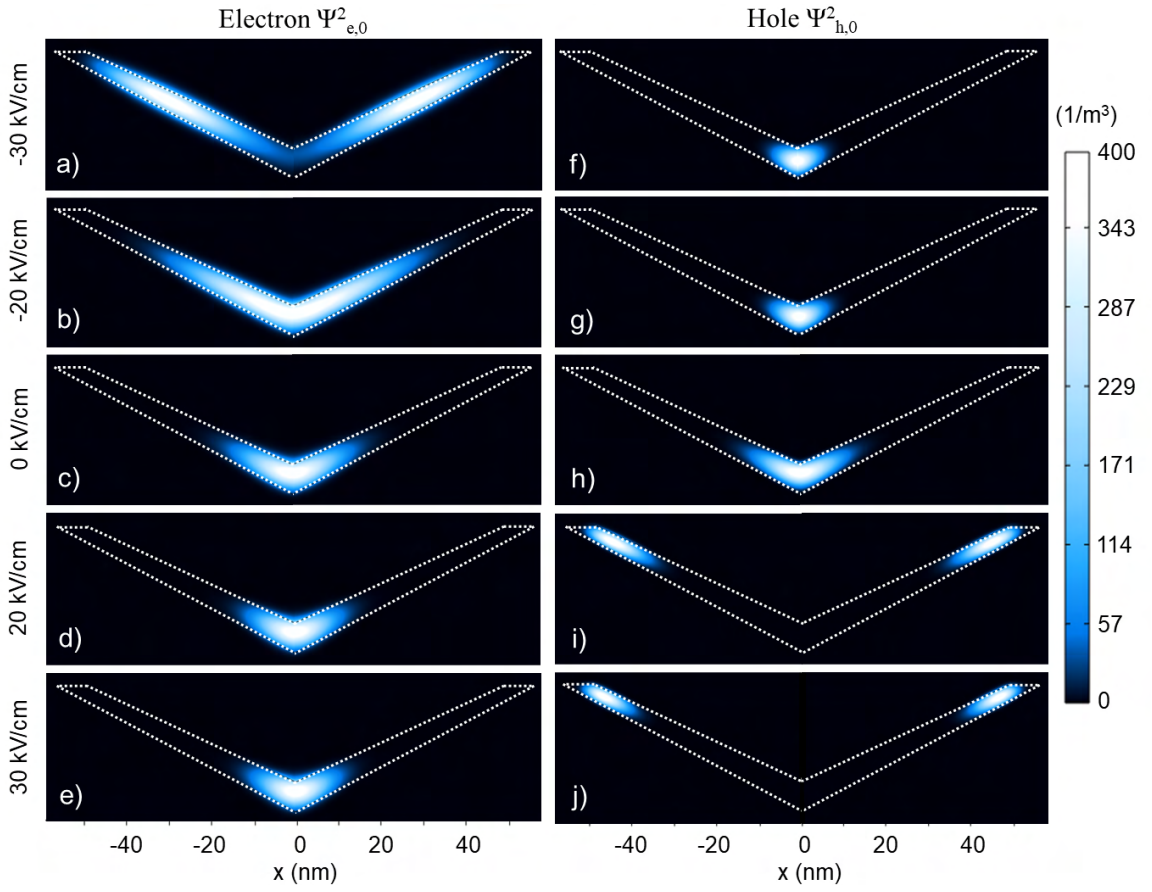

Figure 6.1: Simulated cross-section ground state probability density Ψ^2_0 for electrons (left) and holes (right) in a cone-shell QD (the QD shape is indicated with white dashed lines). A vertical electric field F of (a,f) $-30\,\mathrm{kV/cm}$, (b,g) $-20\,\mathrm{kV/cm}$, (c,h) $0\,\mathrm{kV/cm}$, (d,i) $20\,\mathrm{kV/cm}$ and (e,j) $30\,\mathrm{kV/cm}$ is applied. The probability density of the squared wavefunctions is colour scale encoded as indicated on the bar at the right hand side.

and extends over a larger space in the confinement structure compared to the hole wavefunction. Applying a negative electric field F from bottom to top, the electron is pushed towards the top and, due to the structural configuration, the electron moves towards the sides, whilst the hole wavefunction is further squeezed into the tip of the cone-shell. This can be clearly seen, for example, in fig. 6.1a and f, in which a field of $-30\,\mathrm{kV/cm}$ is applied. In this way, an electron ring is obtained whilst the hole wavefunction stays as a dot. The contrary is obtained when a positive electric field F is applied. In this case, the electron wavefunction is squeezed at the tip of the cone-shell whilst the hole is pushed towards the base, thus an electron quantum dot (fig. 6.1d and e) and a hole quantum ring (fig. 6.1i and j) are obtained. It can be noticed that, again due to the difference in effective masses between electrons and holes, a smaller electric field $|F|$ is needed to form a hole ring compared to an electron ring. For example, at $-20\,\mathrm{kV/cm}$, the electron wavefunction is not forming a clear ring yet and part of the probability density is still concentrated at the tip of the cone-shell (fig. 6.1b). On the other hand, the same positive electric field F of $20\,\mathrm{kV}$ is enough for the hole wavefunction to form a well-defined ring (fig. 6.1i).

6.1.2 Exciton frame

The possibility of tuning either the electron or the hole wavefunction separately from dot to ring by means of an electric field is a specific property of the cone-shell QD, made possible by its unique shape. The large displacement between the charge carriers suggests important consequences on the PL emission. To predict the behaviour of the luminescence, the Coulomb interaction C_{eh} needs to be accounted for. The dependence on the electric field F of C_{eh} and of the position of the electron and hole wavefunction center of masses ($z_{c,e}$ and $z_{c,h}$) is shown in fig. 6.2a and b respectively. C_{eh} shows a peak[1] ($C_{eh} = 15\,\mathrm{meV}$) at $F = 0\,\mathrm{kV/cm}$ as this is the position in which the overlap between the electron and hole wavefunctions is maximal. As the electron and hole are pushed apart from each other by applying an electric field, C_{eh} decreases and approaches a minimal value of about $1\,\mathrm{meV}$ at high $|F|$. As previously mentioned, the electron and hole wavefunction extension in the cone-shell (and thus their tunnelling probability into the barrier material) differs due to their different effective masses; this is described in further details also in ch. 7. Consequently, the extent to which they respond to the electric field also differs, as can be seen in the plot of z_c. For example, at $F = -40\,\mathrm{kV/cm}$, $z_{c,e} = 22.6\,\mathrm{nm}$, whilst at $F = 40\,\mathrm{kV/cm}$ $z_{c,h} = 27.1\,\mathrm{nm}$. The gradual flattening of the $z_{c,h}$ curve approaching about $28\,\mathrm{nm}$ is caused by the structural constrain, since the cone-shell has a height of $30\,\mathrm{nm}$. The different response to the electric

[1] For all the simulations, the Coulomb interaction C_{eh} is calculated as a positive value and subtracted to get the exciton energy $E_X = E_g + E_e + E_h - C_{eh}$

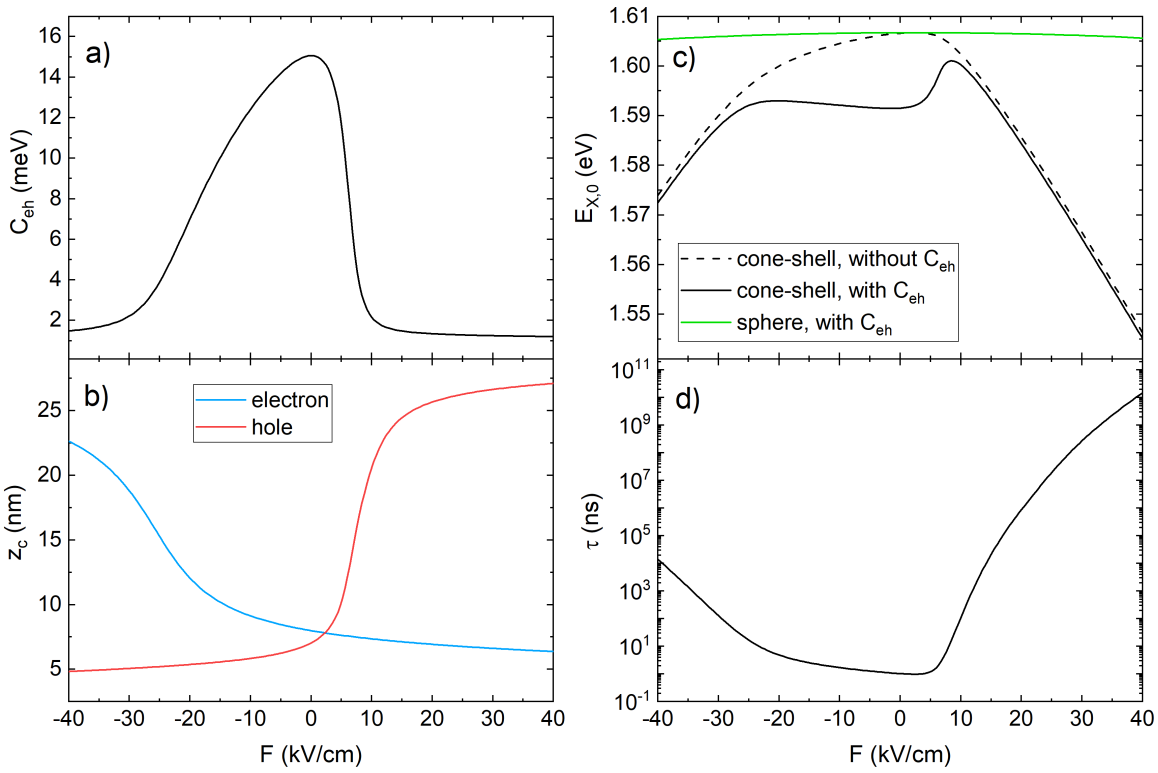

Figure 6.2: (a) Simulated Coulomb interaction C_{eh}, (b) position of the wavefunction center of mass for electron (blue) and hole (red), (c) ground state exciton energy with (black full line) and without including C_{eh} (black dashed line), and (d) ground state recombination lifetime in logarithmic scale as function of the applied electric field F for a cone-shell QD. The green line in (c) is the ground state exciton energy, including C_{eh}, for a spherical QD with wavefunction extension at $F = 0\,\mathrm{kV/cm}$ comparable to the cone-shell QD.

field F from electrons and holes explains the asymmetric behaviour of the $C_{eh}(F)$ plot and of the other variables as function of the electric field F deriving from C_{eh}.

The charge carrier separation causes also a quantum confined Stark-shift [120] in the exciton ground state energy as function of the electric field F (fig. 6.2c). The exciton recombination energy without including C_{eh}, i.e. the sum of the single-particle energies and the band gap energy E_g, is shown with a dashed line. A strong Stark-shift is observed at large electric field, as would be expected, since the Stark shift increases with increasing QD size in the electric field direction [99], which is caused by the increased electron-hole wavefunction separation induced by the electric field. Comparing the dashed and the full black lines, it can be observed that, when C_{eh} is included, $E_{X,0}$ is almost constant for $-22\,\mathrm{kV/cm} < F < 5\,\mathrm{kV/cm}$. This is because the gradual change of C_{eh} in this regime compensates for the energy increase. Similarly, the spike in the $E_{X,0}$ plot for $5\,\mathrm{kV/cm} < F < 10\,\mathrm{kV/cm}$

is associated to the sudden drop of C_{eh} as the holes are pushed from the tip to the base of the cone-shell accompanied with an abrupt electron-hole charge separation. The dashed line, which shows the Stark-shift when C_{eh} is not included, is close to a parabola but it is indeed not fully parabolic, which is a clear consequence of the asymmetric system shape in the z-direction.

It has to be noted that the asymmetry of the cone-shell system is of particular interest and is the cause of the above described field dependence of the QD energy. In fact, a strong confinement (narrow quantum well potential) is attractive for the high quantisation energies, which allow the QD emission to be separated from, for instance, the substrate luminescence. However, such tight confinement limits the ability to experimentally tune the QD emission by means of an electric field, as explained in ch. 3. In the cone-shell QDs, this is not the case: despite the tight confinement, the asymmetric shape causes the coupling of the motion in the radial and the z-direction, leading to a strong field dependence of the energy. To demonstrate this, the cone-shell QD ground state energy is compared to the ground state energy of a spherical QD (fig. 6.2c, black and green full lines respectively). A spherical QD is chosen for its simplicity and because of its wide use in the literature [121–124]. The radius $r = 5\,\mathrm{nm}$ of the spherical QD is chosen such that the cone-shell QD and the spherical QD wavefunction extensions at $F = 0\,\mathrm{kV/cm}$ are comparable. It can be observed that the Stark-shift for the spherical QD is extremely small compared to the cone-shell case. For example, from $F = 8.5\,\mathrm{kV/cm}$ to $F = 40\,\mathrm{kV/cm}$ the variation in the ground state energy is $\Delta E_{X,0} = 56.0\,\mathrm{meV}$ for the cone-shell QD as opposed to only $0.9\,\mathrm{meV}$ for the spherical QD. The Stark-shift of the spherical QD is small because of the small wavefunction shift and, consequently, the small charge carrier separation, allowed by the spherical shape when the electric field is applied.

Although time-dependent PL measurements are not accessible by the set-up used in this thesis, it is interesting to see the theoretical prediction related to the recombination lifetime, as this is an important parameters for applications in quantum technologies. The strong Stark-shift obtained as the electric field F increases is accompanied by a drastic elongation of the recombination life-time, over more than eight orders of magnitude, as can be seen in fig. 6.2d. Due to the stronger displacement of the holes compared to the electrons at the same $|F|$, the elongation is more pronounced for positive electric field, reaching seconds at $F \simeq 40\,\mathrm{kV/cm}$.

6.2 Field-dependent PL measurements: overview

From here onward, this chapter discusses the experimental results obtained for samples #4 to #8. When the computation results are considered, mainly for comparison purpose with the experimental outcomes, this is explicitly stated for clarity.

To obtain an electric field across the QDs, an external bias voltage V_G is applied between the top and the back gates. The PL spectra are then taken as function of V_G. The conversion between V_G and the strength of the electric field F is done by assuming a simple parallel plate capacitor. In this way, the electric field is given by

$$F = \frac{V_{bi} - V_G}{d_{gates}} \tag{6.1}$$

where V_{bi} is the built-in potential of the Schottky diode and d_{gates} is the distance between the top and the back gate (fig. 4.1). This approach represents an approximation. A more precise relation between V_G and the electric field F should consider also internal electric fields induced by depletion zones or charge accumulations. To estimate V_{bi}, the 1D Poisson solver of G. Snider is used [125]. The program uses the method of finite differences to find the 1D band diagram of the semiconductor structure. The mobile charge concentrations are computed using Boltzmann statistics and dopant ionization is also considered for both shallow and deep dopants. In the studied gated samples, the semiconductor layer containing the QDs is unintentionally p-doped, leading to band bending. Two interfaces are thus obtained, each acting as a pn-diode. One interface is the Schottky contact between the metal top gate and the p-type semiconductor and the second interface is the one between the same p-type semiconductor and highly doped n-type back gate. Two depletion zones can then be obtained. The band bending and whether a flat region separates both depletion zones depend on the doping concentration. For the present computations, the unintentional weak acceptor concentration of the 200 nm layer containing the QDs is assumed to be about $10^{15}\,\mathrm{cm}^{-3}$, which results from earlier low temperature mobility measurements. For the heavily doped back gate, a donor concentration of $10^{18}\,\mathrm{cm}^{-3}$ is used. In this case, the depletion zones merge, and the band bending is small. When the layer between the gates is fully depleted, any change in the voltage does not cause changes in the charge distribution and contributes only to the electric field (i.e. the field to voltage dependence is linear). For the present samples, since the distance $d_{gates} = 200\,\mathrm{nm}$ between the metal contacts is smaller than the usual length of the depletion zone, which is generally on the range of a few microns, it is likely that the background doping is sufficiently low that the layer between the metal gates is fully depleted. An almost linear dependence of the electric field F on the voltage is obtained, in agreement with eq. 6.1.

For the computation through the solver, the height of the Schottky barrier is needed. For an interface between $Al_xGa_{x-1}As$ and various metals, the barrier height is reported to increase with increasing x from 0.00 to 0.33 [126–130]. This increase, in the case of an $Au/Al_{0.33}Ga_{0.67}As$ and $Au/Al_{0.30}Ga_{0.70}As$ contacts is of 20% and 19% compared to Au/GaAs (i.e. where the Al concentration is 0) [126]. Assuming a similar increase in the case of $Ti/Al_{0.33}Ga_{0.67}As$ and $Ti/Al_{0.30}Ga_{0.70}As$, and knowing that the expected barrier height for Ti/GaAs is of 0.84 V [131], the expected barrier height is 1.01 V for $x = 0.33$ and 1.00 V for $x = 0.30$. Using these values in the 1D Poisson solver, V_{bi} can be estimated and can be approximated to 0.72 V.

Experimentally, this value can be obtained by measuring the photocurrent I as function of the applied voltage V_G (I-V curve). In fact, when the sample is illuminated by the laser, the photons excite charge carriers in the AlGaAs barrier. Due to the band bending, and depending on the bias polarity and the material doping, the electrons are dragged towards the top gate and holes towards the back gate or vice versa, causing a photocurrent that depends on the laser power and on the electric field. When V_G compensates V_{bi} (flat-band condition), no photocurrent is present. Since the application of a voltage to a non-illuminated Schottky diode also leads to a current, in reality the current induced by the forward bias compensates the photocurrent slightly before the photocurrent becomes 0 [130]. Thus the experimentally measured V_{bi} are higher than the predicted 0.72 V value.

Besides using the $I-V$ curve, there are also other experimental ways to assign a value to the built-in potential V_{bi}. In fact, one argument is that the maximum of the energy plot $E(V_G)$ is obtained at $F = 0$ kV/cm and thus V_G at which the maximum is obtain corresponds to V_{bi}. Another argument is that, at flat-band condition, the wavefunction overlap should be maximised (shortest lifetime) [76] and thus the intensity is maximised. Hence V_G at which the QD PL emission intensity is maximised corresponds to V_{bi}, assuming symmetric confinement potential. All the methods lead to slightly different results. Due to the difficulty in assigning a value to V_{bi} and for consistency reasons, all the voltage to field conversions in this thesis, unless otherwise stated, are done by fixing $V_{bi} = 1.8$ V. This value is the one for which simulations using an atomistic model (discussed later), with the parameters in fig. 4.6, best fit the corresponding experimental data.

6.3 Exciton and biexciton energy

In the measurements discussed here, the exciton (X) and biexciton (XX) peaks are identified by performing a power dependent measurement at $V_G = 0$ V, to study the relative

behaviour of the peaks. In fact, initially only the X peak is visible and, as the power increases, the XX peak appears. Further increasing the power, the XX peak intensity grows, until it overcomes the X peak [132]. The physics behind this behaviour is related to the likelihood of the QD ground state occupation with excitons and biexcitons and is described by a rate model outlined in ch. 3. An example of the exciton and biexciton relative intensities as function of the excitation power is shown in fig. 3.5. In the measurements discussed below, besides the indicated X and XX peaks, a number of other peaks are present, which are associated to other excitonic complexes. In this work, only X and XX are considered in detail (unless otherwise stated). In this section, a first overview of the main features observed in the QD energy spectra is first outlined through some example plots. Detailed comparisons are then given in the sections that follow.

The PL emission energy E of a QD from sample #4, taken with laser illumination power of $22\,\mathrm{W/cm^2}$, is shown in fig. 6.3a as function of V and the electric field F. The colours indicate the emission intensity, with red being the highest intensity and blue the lowest. From $F = -35\,\mathrm{kV/cm}$ to $30\,\mathrm{kV/cm}$, a small Stark-shift (blue-shift) of about $0.8\,\mathrm{meV}$, for both X and XX emissions, is observed. The Stark-shift is slightly stronger at negative electric field (larger V_G). The separation between X and XX emissions stays roughly constant at about $E_X - E_{XX} = 2.4\,\mathrm{meV}$. At the chosen low power, the X energy has the strongest intensity over the whole field range. The third energy line below the XX line is associated to an excitonic complex. Beside this line, at least two replicas of the high intensity lines are observed at higher energies, which can be emissions from other QDs neighbouring the directly illuminated QD. As a final observation, all the peaks abruptly lose intensity at about $1.1\,\mathrm{V}$.

The PL emission from a second QD of the same sample positioned in the same Ti window of the first QD is shown in fig. 6.3b. All the measurements in the plot are taken at a laser power of $20\,\mathrm{W/cm^2}$. Since the XX energy line can hardly be distinguished by the lines of the other excitonic complexes, only the emission from X is indicated. There is almost no change in the X energy in the range of the electric field F considered below about $37\,\mathrm{kV/cm}$, whilst, between $37\,\mathrm{kV/cm}$ and $40\,\mathrm{kV/cm}$, a red-shift of $2.4\,\mathrm{meV}$, indicated with a red arrow in fig. 6.3b, is observed. Compared to QD1 in fig. 6.3a, QD2 emits at higher energies, indicating that the second QD is smaller than the first. The size variation of the two small QDs obtained by filling the nanoholes with 2 GaAs pulses is within the range expected for this type of QD ensembles [68]. For a smaller QD, a smaller Stark-shift is expected. It would thus be expected to observe a drop in energy with increasing electric field (for $V_G < 1\,\mathrm{V}$) for QD1, stronger than for QD2. However, due to the drop in intensity at low voltage, this

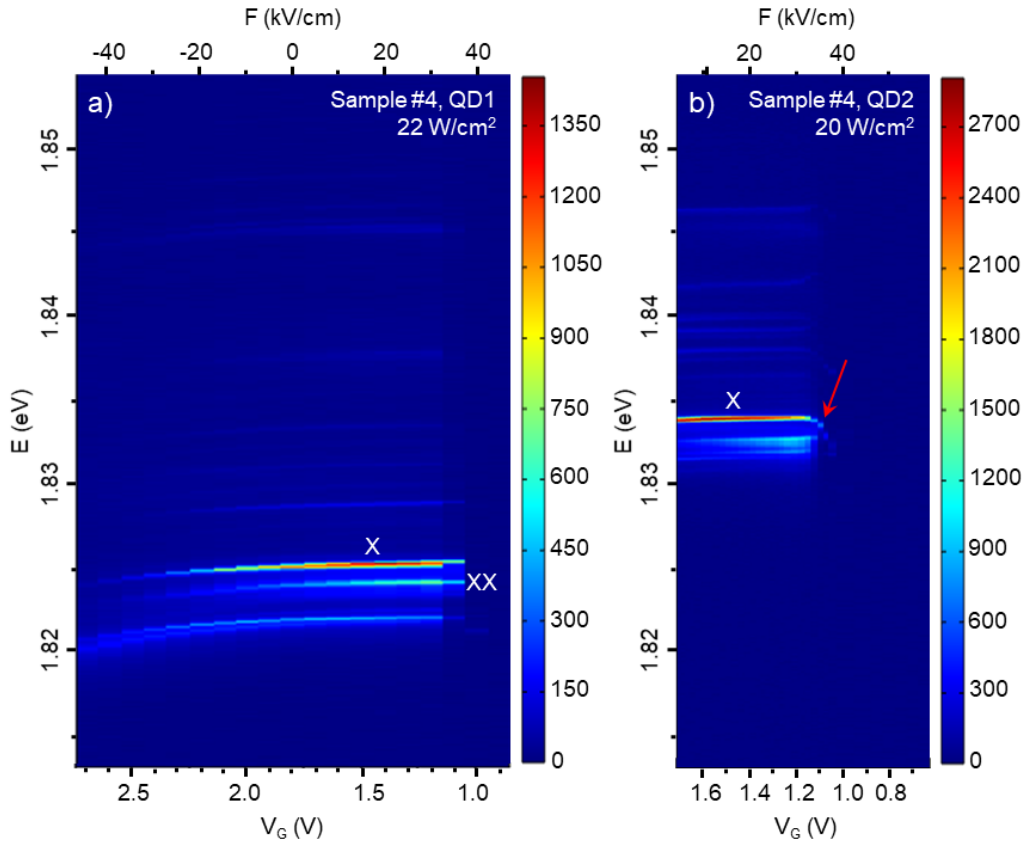

Figure 6.3: Energies of emission lines as function of V and the electric field F (with $V_{bi} = 1.8\,\mathrm{V}$) for two different QDs in sample #4 (2 filling pulses), under the same top gate pad. The exciton (X) and biexciton (XX) energy lines are labelled. The colours indicate the emission intensity. The measurements are taken by illuminating the sample with a green laser (532 nm) with a power of (a) $22\,\mathrm{W/cm^2}$ and (b) $20\,\mathrm{W/cm^2}$. The energy scale is the same for the two plots for better comparison.

is not visible in the measurements.

As a further example, the PL emission energy of a QD of sample #7, obtained by illuminating the sample with $112\,\mathrm{W/cm^2}$ laser power, is shown in fig. 6.4. As the negative electric field becomes smaller, the emission energy shows a strong red-shift ($\Delta E = 3\,\mathrm{meV}$ from $0\,\mathrm{kV/cm}$ to $-20\,\mathrm{kV/cm}$). At low positive electric field, the X and XX energy lines are nearly flat whilst at high $F > 50\,\mathrm{kV/cm}$ the energy red-shifts with increasingly positive electric field. The change in energy in the positive field range is steeper than in the negative range, as expected for a cone-shell QD. The behaviour of the lines at strong positive electric field is barely visible because, as for the first QD in sample #4 (fig. 6.3a), the intensity of the peaks abruptly decreases below $V_G \simeq 0.7\,\mathrm{V}$ (or for $F \geq 55\,\mathrm{kV/cm}$). The stronger Stark-shift observed in sample #7 compared to sample #4 is explained by the QD size, as

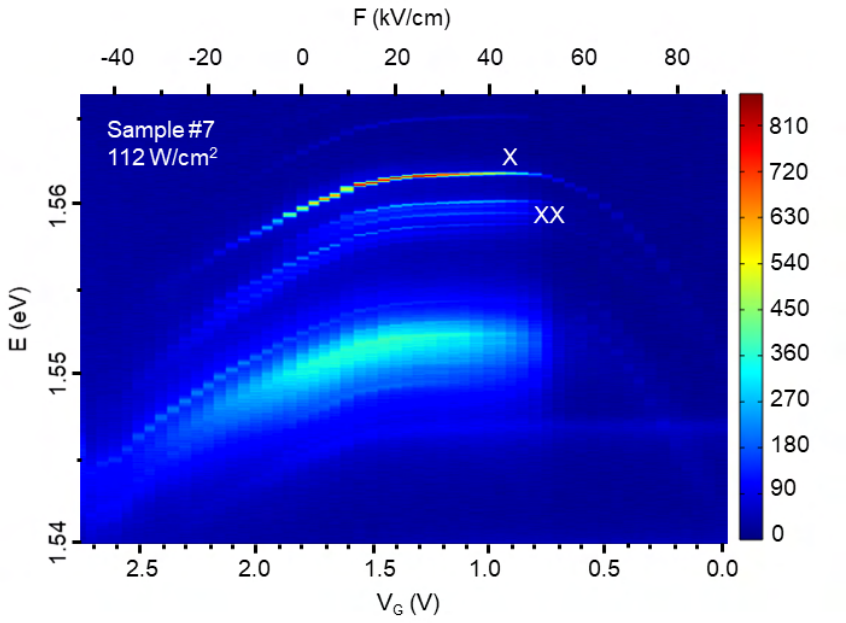

Figure 6.4: Energy as function of V and the electric field F (with $V_{bi} = 1.8\,\mathrm{V}$) of a QD in sample #7 (4 filling pulses). The exciton (X) and biexciton (XX) energy lines are labelled. The colours indicate the emission intensity. The measurements are taken by illuminating the sample with a green laser (532 nm) with $112\,\mathrm{W/cm^2}$ excitation power.

in sample #7 the nanoholes are filled with 6 pulses instead of 4, obtaining larger QDs. Since the Stark-shift is stronger with increasing QD size, the experimental results qualitatively confirm the expected behaviour. The larger QD size in sample #7 as opposed to sample #4 is also reflected in the lower emission energy of the former.

6.4 Shape-dependent Stark-shift

As previously mentioned, the Stark-shift increases with increasing QD size in the field direction, as the charge carriers that are separated by the electric field have more space to move further from each other. In this section, emissions from QDs from samples #4, #5, #6 and #7, obtained by filling nanoholes with respectively 2, 2.5, 4 and 6 pulses, are compared to obtain a quantitative relationship between the QD height and the energy shift. A comparison between the exciton energies E_X for these samples is shown in fig. 6.5a. As a first clear observation, the Stark-shift is strongest for larger QDs. In fact, for the QD of sample #4, of which the height expected with AFM imaging is around 3.9 nm, the difference in energy is of about 1.1 meV from $F = -40\,\mathrm{kV/cm}$ to $30\,\mathrm{kV/cm}$. For sample #5, with 4.9 nm expected QD height, the energy shift for the same field variation is 6.2 meV. For these two samples, the PL emission at high positive electric fields is hardly visible and data points are thus

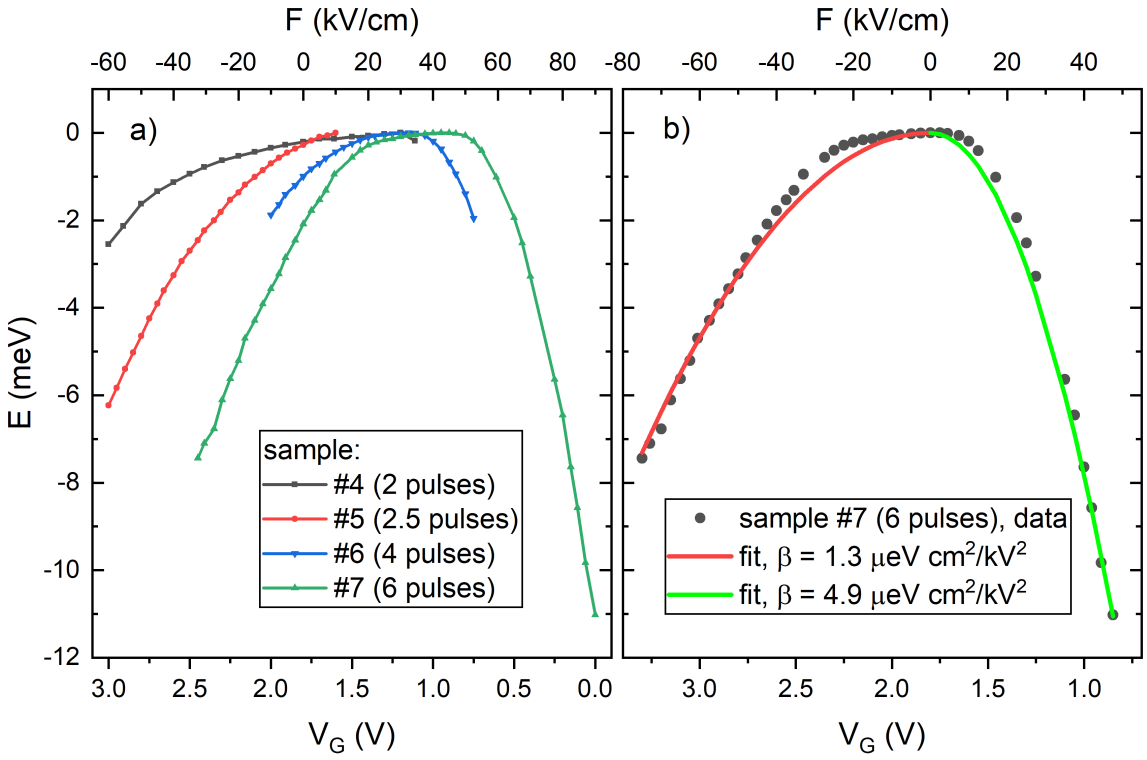

Figure 6.5: (a) Stark shift of the exciton energy E_X of a QD from each sample, as indicated. The power used for the measurements are 46 W/cm^2 for sample #4, 112 W/cm^2 for samples #5 and #7, and 1778 W/cm^2 for sample #6. All the energies are with offset to have the same maximum energy at 0 meV for better comparison. (b) Experimental data from sample #7 (same as the green line in (a)) and parabolic fit using a simple point charge model (see eq. 3.13) with two different polarizability values, as indicated, for negative and positive applied electric field F ranges.

missing in the comparison plot. The emission from the QDs of samples #6 and #7, span a larger range of positive electric field F, up to about 50 kV/cm and 90 kV/cm, whilst on the negative side they reach about -10 kV/cm and -30 kV/cm, after which the signal cannot be distinguished from the noise. The Stark shift for sample #6 QD (with an expected height of about 7.4 nm) is of about 1.9 meV from -10 kV/cm to 30 kV/cm. For the same field range, sample #7 QD (11.8 nm expected height) shows an energy shift of 2.6 meV. As previously inferred, these observations confirm the expected Stark-shift dependence on the QD size. From fig. 6.5a, considering the energy behaviour for increasing F, it can also be seen that the change in the exciton energy observed on the right side of the maximum of each plot in fig. 6.5 is stronger than the change on the left side. This is qualitatively in agreement with the theoretical prediction, for which holes, due to their higher effective mass, need a smaller $|F|$ to be pushed to the sides of the cone-shell, and hence to increase

the electron-hole spatial separation and thus the Stark-shift.

For a comparison of the cone-shell structure with the literature, it is of interest to extrapolate from the plots the polarizability β. Using eq. 3.13 in point-charge approximation and assuming an approximately linear distance d_{eh} between the electron and hole wavefunction barycenters, a parabolic fit is performed. It has to be noted that this approach does not consider the Coulomb interaction, which in the cone-shell system is expected to be a dominant parameter counteracting the Stark-shift induced by the electric field and is also strongly field dependent. Hence, the dipole model used for the fitting is not a precise description of the system and is here used only for a rough comparison with the literature. The resulting fitting lines are shown in fig. 6.5b. To account for the strongly asymmetric Stark-shift caused by the different charge carrier effective masses and the cone-shell shape, as mentioned above, two separate fitting are performed, one for negative electric field F, where the electrons are pushed to the side of the cone-shell, and one for positive F, where the holes are pushed to the sides. The polarizability β is $1.3\,\mu\mathrm{eV\,cm^2/kV^2}$ for electrons and $4.9\,\mu\mathrm{eV\,cm^2/kV^2}$ for holes. These polarizability values are at least one order of magnitude larger than the values found in the literature [133].

6.5 PL intensity dependence on power and voltage

A comparison between PL spectra of the same QD in sample #4, taken at different excitation powers, is shown in fig. 6.6. At low power of $22\,\mathrm{W/cm^2}$ (fig. 6.6a), the X emission has the strongest intensity throughout the whole field range considered. The XX emission is strong at positive fields and gradually decreases in intensity as the field becomes smaller. When a stronger power of $46\,\mathrm{W/cm^2}$ is applied (fig. 6.6b), the XX peak is stronger than the X peak at high positive fields and gradually decreases in intensity as the field strength reduces, whilst the X peak starts increasing, becoming stronger than the XX peak below $18\,\mathrm{kV/cm}$, and then wears off at highly negative fields. By increasing the power even further, to $78\,\mathrm{W/cm^2}$ (fig. 6.6c), the XX emission becomes even stronger whilst the relative intensity of X, with respect to the XX intensity, reduces. As the power increases, it can be observed that the lines associated to other excitonic complexes and to aforementioned neighbouring QDs of slightly different sizes become more evident. A detailed explanation about the behaviour of the relative intensities of the X and XX peaks is given in ch. 3.

When the sample is illuminated by the laser non-resonantly (i.e. when the energy of the laser photons is larger than the band gap energy of the barrier material), the electrons are excited above the conduction band edge of the barrier material. Through phonon emission,

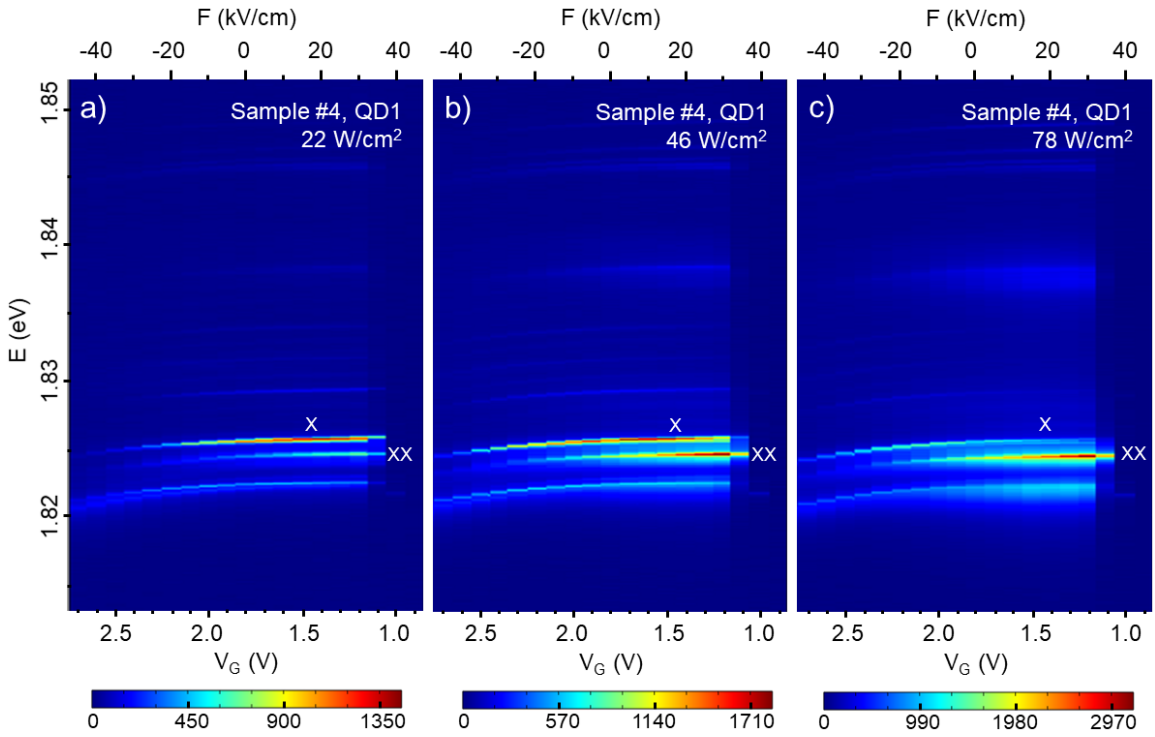

Figure 6.6: PL emission spectra as function of gate voltage V_G and electric field F (with $V_{bi} = 1.8\,\mathrm{V}$) from a QD of sample #4 (2 filling pulses), taken by illuminating the sample with a green laser (532 nm) with excitation power of (a) $22\,\mathrm{W/cm^2}$, (b) $46\,\mathrm{W/cm^2}$ and (c) $78\,\mathrm{W/cm^2}$.

the so formed electrons and holes, relax first into the band edge and then, when in the proximity of a QD, they further relax into the lowest energy levels of the QD. As outlined in ch. 3, the excitonic and biexcitonic emissions are obtained when a bound electron-hole pair in the ground state recombines respectively without or with the presence of a second pair in the ground state. It is thus clear that, with increasing laser power, the number of excited charge carriers occupying the QDs increases, hence causing the recombination of a higher number of excitons per unit time and thus increasing the intensity.

As previously mentioned, another feature of the intensity dependence on the field is the sudden drop at high positive fields, or low voltage values. This can be clearly observed in fig. 6.6, where the intensity of all the emission lines drops for $F \geq 31\,\mathrm{kV/cm}$, or $V \leq 1.18\,\mathrm{V}$. The value at which the intensity drops is power independent. The reason behind this intensity drop at high fields is unclear. However, comparing various spectra (fig. 6.7, top row), the following general ideas and speculations can be obtained. Comparing the spectra in fig. 6.7a, b and c (top), taken by measuring QDs from 3 different samples, it can be seen that the intensity drops at different field values for the different samples, ranging from

about 20 kV/cm to 50 kV/cm. It can thus be inferred that the intensity drop is not caused by the setup or the measurement instruments. Samples #4 and #7 underwent a HCl dip, whilst samples #5 and #6 did not. Again comparing the spectra in fig. 6.7a, b and c and also considering previously studied spectra for sample #4, such as those in fig. 6.3, the HCl dip does not seem to play a role in the sudden intensity variation. Furthermore,

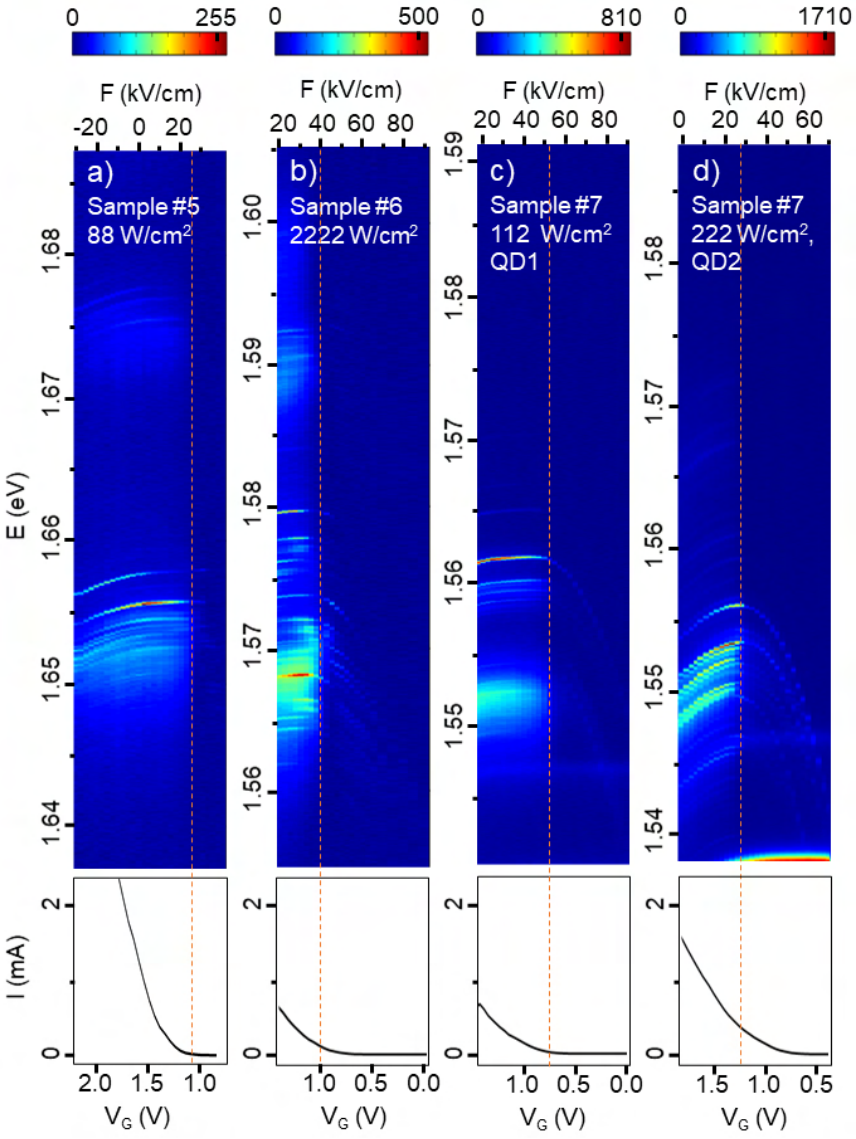

Figure 6.7: Top row: voltage or field dependent ($V_{bi} = 1.8\,\mathrm{V}$) PL emission spectra from a QD (a) from sample #5 (2.5 filling pulses), taken by illuminating the sample with a green laser (532 nm) and at excitation power of $88\,\mathrm{W/cm^2}$, (b) from sample #6 (4 filling pulses) at $2222\,\mathrm{W/cm^2}$ and (c) from sample #7 (6 filling pulses) at $112\,\mathrm{W/cm^2}$ and (d) at $222\,\mathrm{W/cm^2}$ (two different QDs positioned under two different top gate pads). The dashed red lines mark the voltage at which the intensity rapidly diminishes. Bottom row: corresponding I-V curves for each measurement of the top row.

comparing the spectra of two QDs under different top gates on the same sample, such as in fig. 6.7c and d (top), it can be seen that these measurements also differ in the value at which the intensity drops. The two QDs are measured at different powers but, from the previously discussed spectra, it is concluded that the drop is power independent. Hence, the comparison suggests that the value at which the intensity drops varies depending on the gate where the voltage is applied. Given these observations, and in particular the fact that the field values at which the intensity suddenly drops is always positive, one possibility is that the intensity change reflects the sudden charge separation when the hole moves into the base of the cone-shell QD.

Besides the above mentioned general observations, an analysis of the *I-V* curve of each measurement (bottom row of fig. 6.7) suggests a link between the onset of the leakage current and the abrupt intensity change. The link is explained by injection of charge carriers into the QDs once the leakage current starts flowing, and thus the formation of charged excitons and other excitonic complexes. This hypothesis is also supported by the presence of several emission lines on the left side of the dashed red lines in fig. 6.7, as opposed to just a few emission lines in the low intensity side (right side of the dashed red lines). However, fig. 6.7d does not fully fit this interpretation, as the change in intensity occurs when the leakage current is already about 0.3 mA, and not at its onset.

6.6 Simulation and experimental results comparison

The simulation results outlined at the start of this chapter are here compared with the experimental results. The QD model used for the simulations has a height of 7.05 nm (fig. 4.6), which is obtained by AFM imaging of a sample with 4 filling pulses. Hence, for comparison, experimental measurements of sample #6 are considered. A comparison between the expected and real result is shown in fig. 6.8a.

As a first observation, the Stark shift in the experimental results is on the range of meV whilst the simulated one is on the range of 10^{-1} eV, i.e., about one to two orders of magnitude larger. This indicates that the model predicts a vertical charge carrier displacement larger than what is experimentally obtained. This suggests that the parameters used for the simulations do not match with the sample considered. As the number of available samples with gate structures is limited and QD size and exact shape differ from sample to sample, here a short discussion is made to find the parameters that can best match the specific experimental outcome shown in fig. 6.8a[2]. Although the following optimisations of the model

[2]For the simulations that follow in this thesis, the earlier used parameters (see ch. 4) are kept for the model as a basis for discussion.

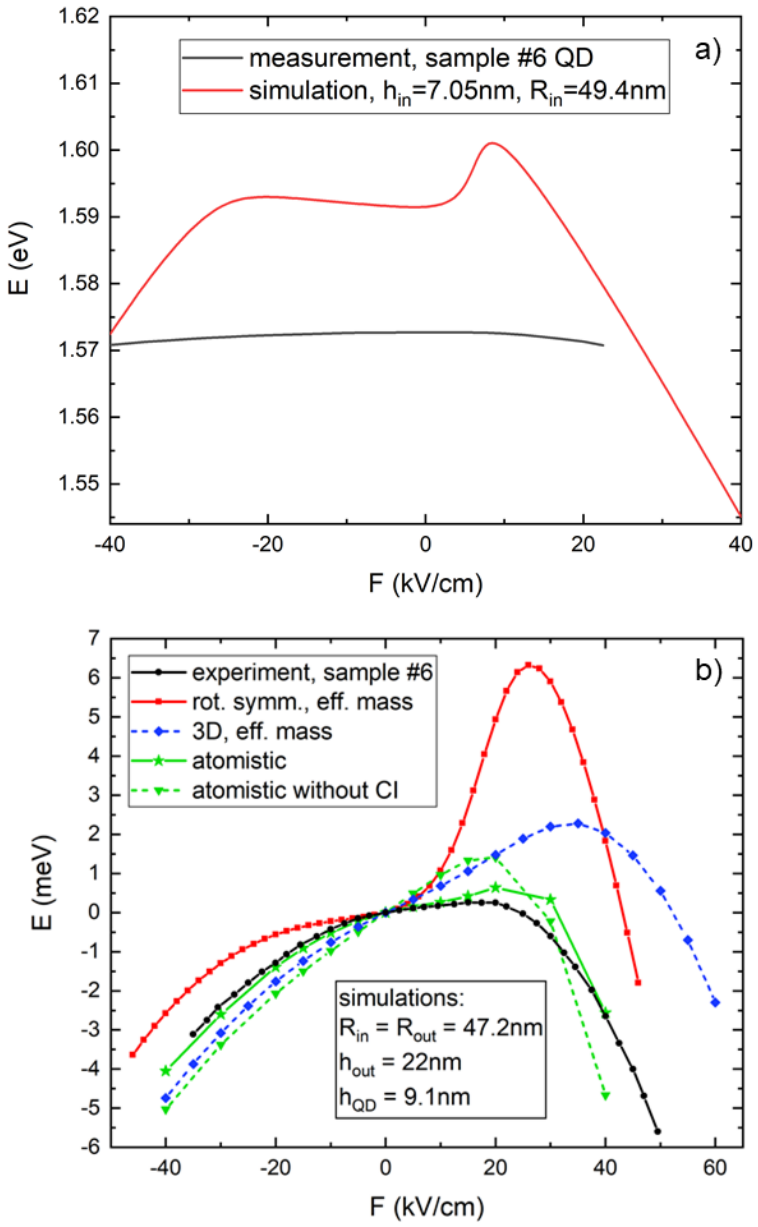

Figure 6.8: (a) Comparison between simulated (red) and measured exciton energy for a QD in sample #6 (black). The simulated line is obtained using a QD model with the height and internal radius as indicated; the other parameters can be found in ch. 4. (b) Comparison between the same experimental result (black) and simulations using 3 different models: rotational symmetric quasi-3D model in the effective mass approximation (red), fully 3D model also in the effective mass approximation (blue) and atomistic model with (green full line) and without including configuration interaction (green dashed line). All the simulations are performed using the indicated model parameters and all the lines are with an offset to have $E_X = 0\,\text{meV}$ at $F = 0\,\text{kV/cm}$ for better comparison.

improve the agreement of the simulation and the experimental results, the computations presented in the thesis are performed using the model in fig. 4.6 due to the extensive computation times and the fact that the new model does not lead to major qualitative differences in the results. The results obtained with the model in fig. 4.6 are still useful to get an indepth understanding of the cone-shell structure.

As mentioned, to improve the agreement between the model and the experimental results, the simulated Stark shift needs to be reduced. As a first step, this can be done by increasing the internal radius R_{in}, such that the wavefunction's shift towards the side of the cone-shell is reduced. Another way to reduce the wavefunction shift is by reducing the simulated nanohole height h_{out}. Through various optimisation attempts, the best match of the Stark-shift is obtained for $R_{in} = R_{out} = 47.2\,\text{nm}$ and for $h_{out} = 22\,\text{nm}$. Despite the improved agreement obtained by using these model parameters, the simulated E_X remains still higher than the experimental value. To adjust this, the height of the simulated QD needs to be increased, which in turn leads to a weaker confinement and thus a lower E_X. The QD height that gives the best match is 9.1 nm. The optimised model is shown in fig. 6.9 and the final simulated result obtained using this model is shown by the red line in fig. 6.8b, along with the experimental result indicated with the black line. It can be observed that the two lines have a good match, although not perfect, only for negative electric field. In fact, the simulated peak at positive electric field is barely visible in the experiment. The difference between the energy at the highest point of the simulated line and the experimental E_X at the same electric field value of $26\,\text{kV/cm}$ is about 6.8 meV. Analysing the behaviour of the ground state exciton energy curve with and without C_{eh} (fig. 6.2c), it can be noted that the curve without C_{eh} closely resembles the experimental behaviour. This suggests that the strong discrepancy at positive electric field between simulated and experimental result is caused by an overestimation of C_{eh}.

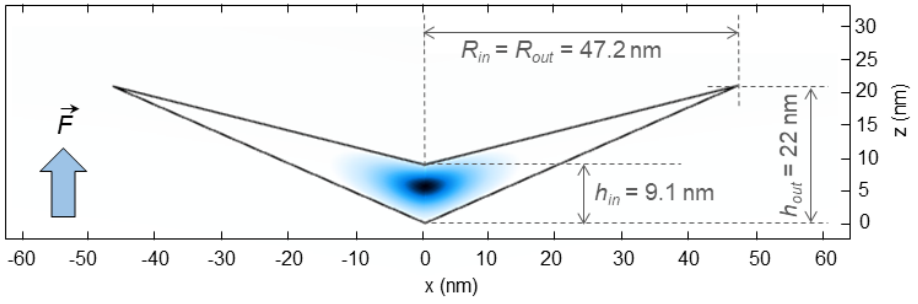

Figure 6.9: Schematic of the cone-shell QD model optimised for a better match with the experimental results obtained for sample #6 QDs. The dimensions used for the simulations are indicated along with the direction in which the electric field is applied.

To understand the issue in the model, other models are compared with the present one and the results are shown in fig. 6.8b. For better comparison, all the lines have an offset such that $E_X = 0\,\mathrm{meV}$ when no electric field is applied. The blue line is obtained using a 3D model (including C_{eh}) [98], which does not assume rotational symmetry but still assumes effective mass approximation[3]. The model parameters used are the same as for the previously discussed improved model (fig. 6.9). The agreement for both the negative and positive electric field range is significantly improved. This suggests that the assumption of rotational symmetry, which is the main difference between this model and the previously discussed one, should be taken with care for simulations in an electric field. However, despite the better agreement, the energy overestimation for $F > 0$ is still considerable, with a difference of about 3.6 meV at 35 kV/cm, where the $E_X(F)$ peak of the simulated result is maximum. An empirical adjustment of the hole effective mass m_h^* gives an improved agreement between the experimental and simulated results of the 3D effective mass model. The best agreement is obtained for $m_h^* = 0.2m_0$ but, since no physical explanation can yet be attributed to this value, this is not considered in the model comparison in fig. 6.8.

A third model is an atomistic model[4], which takes into account CI for 12 conduction and 12 valence state energies. The resulting E_X for the atomistic model, with the same structural parameters as for the other simulations (fig. 6.9), is shown with a solid green line in fig. 6.8b. The result is in almost perfect agreement with the experimental results, with an only small peak. The small discrepancy can be attributed to the simulation parameters not being exactly matching the QD considered and to the fact that the real QDs do not have the ideal shape used for the computations. It can be thus concluded that the overestimation of E_X for $F > 0$ in the previous two models is caused by either (or both) the effective mass approximation and by not including correlation effects.

For a better understanding, the atomistic computation is also performed without inclusion of correlation effects (fig. 6.8b, dashed green line). The peak in the positive electric field range of the $E_X(F)$ curve slightly increases when excluding CI, stronger deviating from the experimental results. However, the peak remains much lower than the one obtained with the simulation in the effective mass approximation. This indicates that the missing CI and the effective mass approximation both contribute to the energy overestimation, with the latter being the dominant part. Hence, further work can be done to include CI in the earlier discussed models to obtain an improved result, but for quantitatively reliable results a more realistic model than the effective mass approximation needs to be used. In any case, due

[3]The results using the fully 3D model are computed by Christian Heyn.

[4]Atomistic model development and result computation by Geoffrey Pirard and Gabriel Bester (Hamburg, work to be published).

to the extensive computation time for the atomistic model, its complexity, and the limited available computation memory, the effective mass approximation is used also in ch. 7 to analyse the behaviour of the cone-shell QDs in an external magnetic field. Although not perfect, the results obtained using this approximation can still give an interesting insight into the qualitative characteristics of the QD PL emission.

6.7 PL from QDs in an n-i-p diode

PL measurements taken from sample #8 differ from the previously discussed results because of the different growth process and materials and fabrication steps of the gates. Hence spectra from sample #8 are here discussed separately. The PL emission from an exemplary QD of this sample is shown in fig. 6.10, where the exciton and other excitonic complexes are indicated according to the literature [134].

As opposed to the previous samples, where the QDs are embedded in a Schottky diode, here the QDs are embedded in an n-i-p diode, which allows very high electric field values above 100 kV/cm. Furthermore, sample #8 has a shorter distance between QDs and back gate (about 30 nm as opposed to 120 nm for the previously discussed samples, app. A), which allows tunnelling and loading of charge carriers into the QDs. However, for the same reason, the lines are visible for a smaller electric field range than for the earlier discussed sample with a larger barrier. Hence, several short lines from excitonic complexes are visible in the spectrum in fig. 6.10. Positively charged excitonic complexes (X^+ and X^{++}) and the neutral exciton peak are visible for $60\,\mathrm{kV/cm} < F < 110\,\mathrm{kV/cm}$. Further decreasing the electric field F, or increasing V_G, the signatures of negatively charged excitonic complexes also become visible (X^- and X^{--}). The discrete jumps in the spectrum at specific electric field values, with one line abruptly losing intensity and the successive one appearing, is the direct evidence of QD occupation change together with Coulomb blockade [135]. As mentioned, thanks to the short tunnel barrier, the QD net charge can be controlled, with the possibility of adding charges one by one by tuning the voltage. When a new charge carrier is added, the additional Coulomb interaction with the new carrier causes the shift in the emission energy, which thus results in the jumps observed in fig. 6.10 [134]. The charge states are indeed assigned by counting the number of jumps in the energy spectrum as the gate voltage V_G changes. For example, X^{--} is assigned to the line that appears right after the X^- line disappears as V_G increases. With measurements of better resolution and with longer exposure times, it is expected that emissions from highly charged excitons (up to about eight-times negatively charged exciton in the case of the QDs in this sample) can be measured [134]. Among QDs with an emission wavelength close-to-visible, the possibility

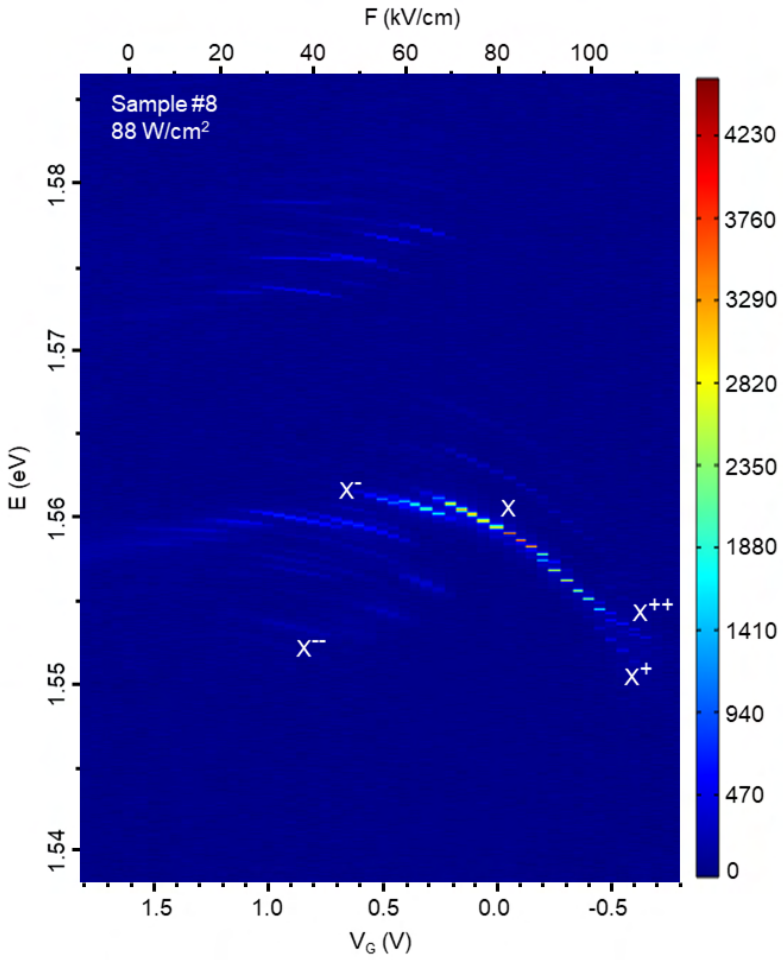

Figure 6.10: PL emission energy spectrum for a sample #8 QD as function of voltage and electric field F (with $V_{bi} = 1.8\,\mathrm{V}$). The measurements are taken by illuminating the sample with a green laser (532 nm), with $88\,\mathrm{W/cm^2}$ excitation power. The colour code indicates the emission intensity (red highest and dark blue lowest intensity). Exciton and excitonic complexes are indicated.

of such a wide range of charge tuning is a feature observed only in samples with the specific structure and growth parameters as of sample #8.

As a further observation, the X energy as function of the electric field F shows a strong energy variation of about 8 meV for a field variation of about $38\,\mathrm{kV/cm}$, which gives an indication of the relatively large QD size, as is also suggested by the numerous lines that can be associated to highly charged excitons, which indicates a higher number of available quantum levels to be filled in the QD.

As observed for other measurements discussed earlier, also here a higher energy replica is observed, which can be attributed to either a neighbouring QD of slightly smaller size or to

the p-shell of the same QD.

Regarding the energy emission intensity, the sudden change in intensity observed for samples #4 - #7 is not visible here and the intensity increases or decreases smoothly for each line. Moreover, the emission intensity of #8 relative to the other samples is much higher, for example the highest count number for the X emission of sample #5 is 250, whilst the one for sample #8 is 4000, where the same illumination power of 88 W/cm^2 and same exposure time of 10 s is considered. The much higher intensity can be attributed to the presence of the DBR in sample #8, which increases the collection efficiency of the photons emitted by the QD [134].

6.8 Summary

The influence of an external vertical electric field F on the optical properties of the cone-shell QD is studied in this chapter, through both simulations and experimental PL measurements. Simulations with rotational symmetry and effective mass approximation show that the cone-shell shape allows a strong charge carrier separation and the formation of either electron or hole rings, depending on the field polarity. This large separation gives rise to a strong Stark-shift and to the elongation of the radiative lifetime up to milliseconds, which suggests these quantum structures for application light storage in the field of quantum information technology.

The measurements also show a strong Stark-shift but on the range of meV rather than the predicted range of 10^{-1} eV. For better agreement with the experimental results, some corrections to the simulation model parameters are proposed. An improved agreement is obtained by increasing the size of the cone-shell tip to 9.1 nm and by making its sides sharp. Despite the reduced Stark-shift of the new model compared to the previous one, the formation of rings is still expected, and hence also the lifetime elongation. Based on the new model, a proposal for improvement of the samples to obtain stronger Stark-shift and longer recombination lifetimes is to fabricate deeper nanoholes with steeper side facets, which can be done by increasing the process temperature during Al droplet deposition [56]. The amount of filling material should also then be accordingly increased so that the entire side facets are covered.

It should be noted that, although the old model does not fully agree with the experimental results, its qualitative results and its predictions (strong Stark-shift, radiative lifetime elongation and, as discussed later, the possibility of observing AB oscillations) are still valid and thus this model can give useful insights on the cone-shell optical properties. Hence and

also due to the extensive computation times required to newly compute the results with the new model, the old model is used in the next chapter for the discussion of the influence of an externally applied magnetic field.

Chapter 7

Quantum ring in magnetic field B

Charge carriers orbiting a magnetic flux in a closed trajectory, such as in a nanometer-scale ring, undergo a phase shift which manifests itself by an oscillatory behaviour of the charge carriers' energy levels as function of the external magnetic field B. This quantum-interference phenomenon is known as Aharonov-Bohm (AB) effect [136]. A direct consequence of the AB effect is the possibility of driving a persistent current through B without any external sources. This persistent current is predicted to have potential applications in quantum information and quantum electronics [137].

The ring-shape wavefunction induced by the electric field F in the cone-shell QDs, as illustrated in ch. 6, suggests these structures for interesting studies under a magnetic field. AB oscillations are a property of charged particles and, apart from tunnelling corrections [101], they are not expected to be observable for neutral particles. However, the strong spatial separation between electrons and holes in the cone-shell QDs when an electric field is applied, hints to the likelihood of observing the AB effect also in neutral excitons, as a result of their enhanced polarization.

In the present chapter, the simple model described in ch. 4 is used to simulate and better understand the cone-shell QD characteristics and to predict possible outcomes of magneto-PL measurements. It has to be noted that the simplicity of the model and the computational approach, which does not take into account configuration interaction, can imply imprecise results. An atomistic model, which is currently not reported in the literature, can give precise results, but due to the complexity and the high computational time and memory required, it is not used here. Furthermore, the model with rotational symmetry and effective mass approximation can be considered to be reliable for small rings, where the exciton radius is smaller than the ring radius. Also, despite its simplistic approach, the model is a strong tool when used to understand the general magnetic field-dependence of the electron-hole interaction and to confirm the possibility of observing excitonic AB oscillations.

7.1 Single particle frame

As a first step, to get a better understanding of the system, the simulations are performed in the single particle frame, without considering electron-hole interaction. The electron and hole single particle energies as function of magnetic field B are shown in fig. 7.1 for fixed values of $F = -20\,\mathrm{kV/cm}$, $0\,\mathrm{kV/cm}$ and $10\,\mathrm{kV/cm}$ applied in the z-direction, from bottom to top. The principal and magnetic quantum numbers n and l_j ($j = e, h$) associated to each energy line are indicated in brackets (n_j, l_j) for some of the lines.

Analysing first the electron energy, it can be seen that, when no electric field is applied (fig. 7.1b), the plot resembles the electron energy spectrum of a perfectly symmetrical QD and can be described using the Fock-Darwin (FD) model described in ch. 3 (eq. 3.20). This is because the electrons are at the tip of the cone-shell structure, which has a conical volume space, allowing the wavefunction to assume a nearly symmetric shape in 3 dimensions. This also explains the fact that the ground state, indicated with red dashes, is obtained for $l_e = 0$ for the entire magnetic field range.

When a positive $F = 10\,\mathrm{kV/cm}$ is applied (fig. 7.1c), the electrons are pushed further towards the tip of the cone-shell, hence the same argument of the $F = 0\,\mathrm{kV/cm}$ case applies. As a difference with respect to the zero-field case, the electron energy lines at positive electric field F are shifted to higher energy values, which reflects the stronger confinement induced on the electrons by the positive electric field F.

When a negative $F = -20\,\mathrm{kV/cm}$ is applied (fig. 7.1a), the electrons are pushed towards the base (sides) of the cone-shell, and the wavefunction assumes a ring-like shape due to the confining structural shape. Hence, as the magnetic field B increases, the energy bands tend to overlap and the ground state l_e switches from 0 to 1 for strong magnetic field B (ch. 3). This behaviour becomes more evident for the hole ring, as discussed later.

Moving now to the analysis of the hole energy spectra, when no electric field is applied (fig. 7.1e) the spectrum is similar to the one of the electron. As the electrons, the holes are also at the tip of the QD and the energy can be described by the FD model, with any deviation being associated to the non-symmetry of the QD shape.

A similar outcome is obtained when applying a negative $F = -20\,\mathrm{kV/cm}$ (fig. 7.1d): the holes are further squeezed to the tip of the cone-shell and the energy spectrum resembles the one of a symmetric QD. The stronger confinement induced by the negative electric field F manifests in the shift of the energy lines to higher energy values.

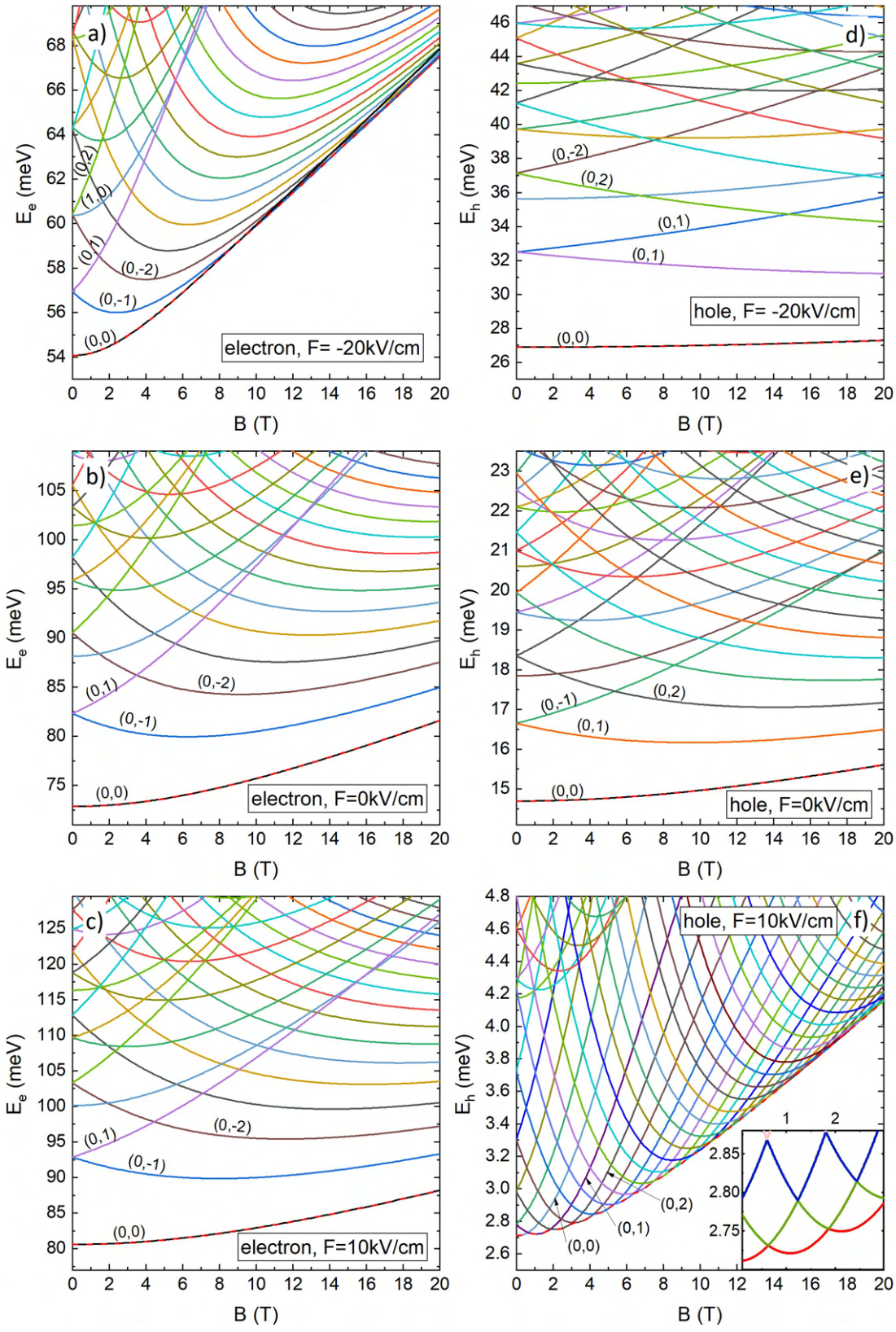

Figure 7.1: (a-c) Electron and (d-f) hole energy without Coulomb interaction C_{eh} for fixed $F = -20\,\mathrm{kV/cm}$, $0\,\mathrm{kV/cm}$ and $10\,\mathrm{kV/cm}$ as indicated. The quantum numbers n and l_j ($j = e, h$) are indicated in brackets (n, l_j). Inset in (f): zoom-in of the hole's first 3 energy states from 0 to 3 T.

The energy spectrum drastically changes when a positive $F = 10\,\mathrm{kV/cm}$ is applied (fig. 7.1f). The holes are now pushed to the base of the cone-shell and form a well-defined ring. A consequence of the ring formation is that the ground state is given by increasingly higher hole magnetic quantum numbers l_h as the magnetic field B increases. For example, the ground state at $B = 1\,\mathrm{T}$, $4\,\mathrm{T}$, $7\,\mathrm{T}$ and $10\,\mathrm{T}$ is given by $l_h = 1$, 3, 6 and 9 respectively. The quick switching between the ground state l_h, which is explained in ch. 3, makes the AB oscillations in the hole energy lines clearly visible. A zoom-in of the first 3 states is shown in the inset of fig. 7.1f, where 3 oscillations are already visible below $3\,\mathrm{T}$.

Altough the general behaviour of electron and hole single particle energy as function of magnetic field B is similar for electric field F with opposite sign, at the same electric field magnitude the effect of the magnetic field is stronger on the holes. This is because of the higher effective mass of the holes compared to the electrons. Considering the Bohr radius of electrons and holes can give a better understanding of how the charge carriers see the confining structure. The Bohr radius is

$$a_{B,j} = \frac{4\pi\epsilon_r\epsilon_0\hbar}{m_j^* e^2} \tag{7.1}$$

with $\epsilon_r = 13.1$ the GaAs relative permittivity, which gives $a_{B,e} = 10.5\,\mathrm{nm}$ and $a_{B,h} = 1.4\,\mathrm{nm}$. The Bohr radii can then be compared to the cone-shell structural sizes described in ch. 4, such as the nanohole radius $R_{out} = 5.4\,a_{B,e} = 40.4\,a_{B,h}$ or the QD height $h_{in} = 0.8\,a_{B,e} = 5.0\,a_{B,h}$. As the comparison suggests, a small electric field is enough to push the holes towards the base or the apex of the cone-shell, as they are more easily polarisable. On the other hand, the electrons are weakly confined and need a much stronger electric field to move, which leads to the energy behaviour in fig. 7.1a, where a field of $-20\,\mathrm{kV/cm}$ is not enough to distinguish clearly the oscillations in the ground state energy at high magnetic field B, as opposed to the spectrum in fig. 7.1f, where $10\,\mathrm{kV/cm}$ are enough to distinctly see the oscillations in the hole ground state energy, already starting from low $B < 1\,\mathrm{T}$.

The confinement induced by the structure on the charge carriers is also linked to the energy separation between the energy points at $B = 0\,\mathrm{T}$. For $F = 0\,\mathrm{kV/cm}$, the separation between the ground state and the first excited state is $9.5\,\mathrm{meV}$ for the electrons and $1.9\,\mathrm{meV}$ for the holes (fig. 7.1b and e). This separation increases to $12.2\,\mathrm{meV}$ for the electrons and reduced to $0.07\,\mathrm{meV}$ for the holes when $10\,\mathrm{kV/cm}$ are applied (fig. 7.1c and f), reflecting the movement of the electrons and the holes further to the tip and towards the base, respectively, as previously described. Similarly, when a negative field $F = -20\,\mathrm{kV/cm}$ is applied, the separation becomes $3\,\mathrm{meV}$ for the electrons and $5.6\,\mathrm{meV}$ for the holes.

By further analysing fig. 7.1, additional information can be obtained on the consequences of applying a magnetic field B. Regardless of the electric field, the ground state at $B = 0\,\mathrm{T}$ is obtained for $(n, l) = (0, 0)$. Furthermore, degenerate states are present, along with non-degenerate ones. Observing the system's Hamiltonian (eq. 4.2) and considering that the electric field does not affect r, as it is applied in the z direction, the former states can be associated to states with same $|l|$ and same n, whilst the latter states to those with $l = 0$ and varying n. When a magnetic field B is applied (from bottom to top), the degeneracy is lifted and the high energy states become the ones with $l_e > 0$ for the electrons and $l_h < 0$ for the holes. The low branch of each energy line pair with same $|l|$, first decreases, reaches a minimum and then goes upward with increasing magnetic field B. The B value at which the minimum is reached is gradually higher for higher $|l|$, as can be seen, for example, in fig. 7.1a.

7.1.1 Deviation from an ideal ring

To optimise and better understand the cone-shell nanostructure, it is useful to study how much the ring-shaped wavefunction of a cone-shell, obtained by applying an external electric field F, deviates from an ideal ring.

The energy of the holes forming a ring in the cone-shell is shown in fig. 7.2a to c for different fixed electric field F, whilst the energy dispersion of the hole confined in an ideal ring is shown in fig. 7.2d. The corresponding cross-sections of half the structure, symmetric with respect to $x = 0$, are shown in fig. 7.3. At low electric field, the hole ring is still not well defined and, in the considered range of up to $B = 4\,\mathrm{T}$, no ground state oscillation is visible. At stronger $F = 10\,\mathrm{kV/cm}$, as already observed in sec. 7.1, a well defined hole ring is formed, which is proven by the clear oscillations in the $E_h(B)$ plot due to the switching of the hole magnetic quantum number l_h associated to each energy level. As the electric field further increases, the system starts behaving very similarly to the ideal ring case. The energy spacing between each energy level at $B = 0\,\mathrm{T}$ becomes smaller and the ground state energy line is pushed less upwards as the magnetic field B increases. The differences between the spectra from the cone-shell QD and the ideal ring are due to the fact that the cross-section of the wavefunction is not a perfect circle but has rather an elongated shape which is asymmetric in the xz-plane. As the electric field F increases, the holes are squeezed at the base of the cone-shell and the wavefunction cross-section becomes closer to a perfect circle.

In the ideal ring case, the energy spectrum as function of magnetic field can be used to extrapolate some of the structural characteristics of the ring. For example, the radius R

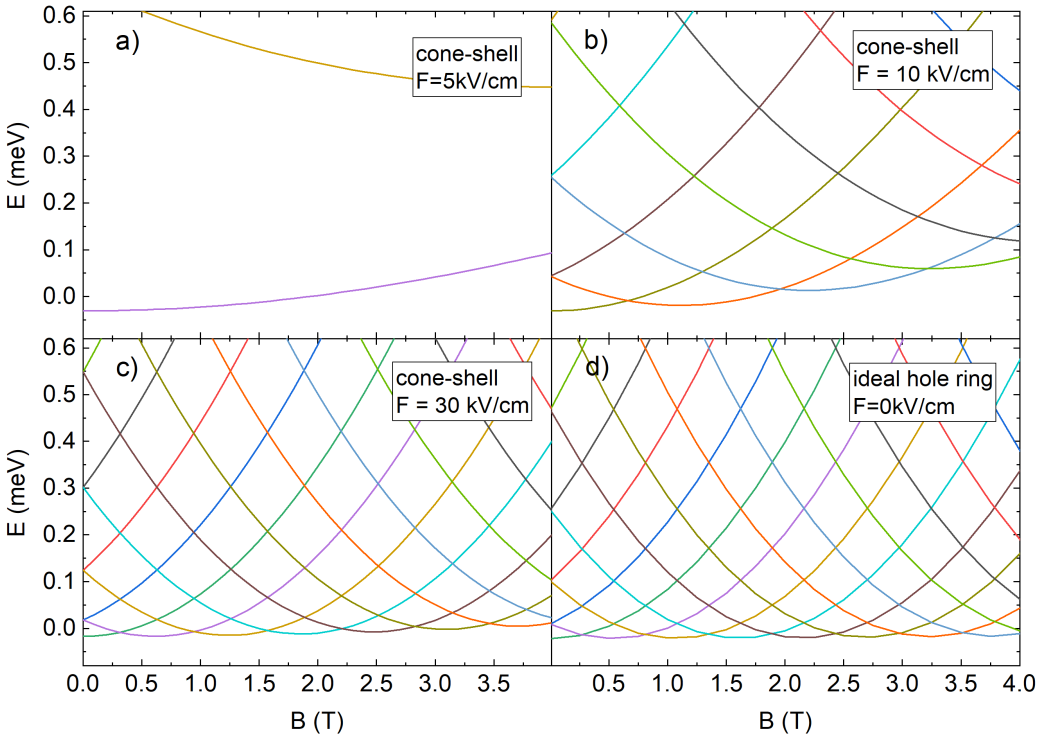

Figure 7.2: Hole energy as function of magnetic field B for the cone-shell structure at (a) $F = 5\,\mathrm{kV/cm}$, (b) $F = 10\,\mathrm{kV/cm}$ and (c) $F = 30\,\mathrm{kV/cm}$ and (d) for a hole confined in an ideal ring with no applied field. All the energies are with an offset for better comparison.

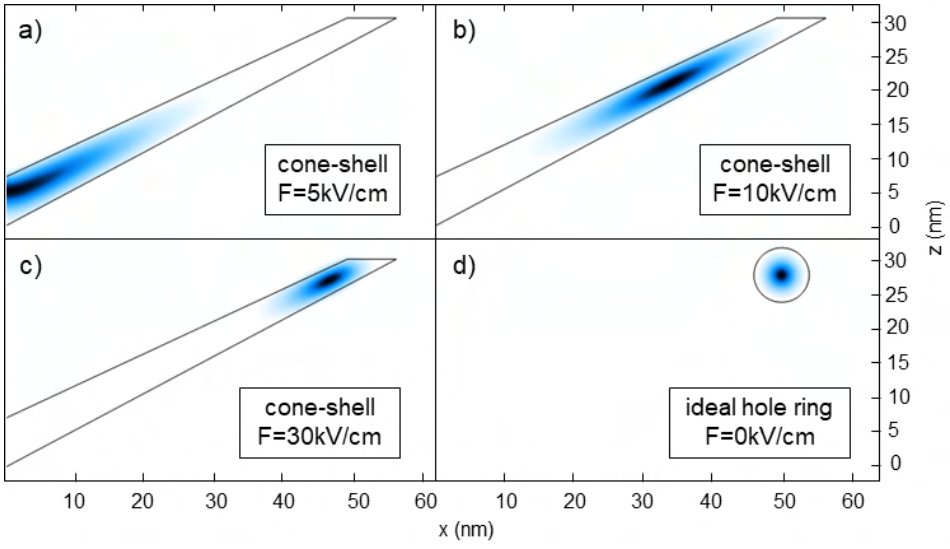

Figure 7.3: Cross-section of the hole probability density in the xz-plane of the cone-shell at (a) $F = 5\,\mathrm{kV/cm}$, (b) $F = 10\,\mathrm{kV/cm}$ and (c) $F = 30\,\mathrm{kV/cm}$ and (d) of the ideal ring with no applied field. All the schematics are for no applied magnetic field. The most intensive part of the probability density is in dark blue and the least intensive in white.

can be calculated in two ways. One is by using, for example, the energy spacing [138] ΔE_{1-0} between E_0 and E_1 at $B = 0\,\mathrm{T}$:

$$R = \sqrt{\frac{\hbar^2}{2m_j^* \Delta E_{1-0}}}. \tag{7.2}$$

Another way is to use the AB oscillation period ΔB [101, 139]:

$$R = \sqrt{\frac{\Phi_0}{\pi \Delta B}} \tag{7.3}$$

where $\Phi_0 = h/e$ is the flux quantum. From the energy plot of the ideal ring, $R = 49\,\mathrm{nm}$ and 51 nm when computed using eq. 7.2 and eq. 7.3 respectively, which matches the simulation parameter $R = 50\,\mathrm{nm}$ with a $\pm 1\,\mathrm{nm}$ precision. This imprecision likely originates from the fact that the above formulas assume a ring with a zero cross-sectional wire diameter, while the diameter of the wire of the ring considered in the simulation has a finite value of 8 nm. For the cone-shell structure, when an electric field F of $10\,\mathrm{kV/cm}$ is applied, the radius calculated analytically is 33 nm using both methods with the energy spacing at $B = 0\,\mathrm{T}$ and the period from the first to the second ground state oscillation. This agrees with the wavefunction center of mass observed from the simulation, which is 34 nm. However, as opposed to the ideal ring case, the AB oscillation period in the cone-shell energy dispersion is not constant and hence the corresponding analytical result varies. For example, if the period is taken for oscillations between 15.6 T and 16.6 T, the computed R would be 36 nm, and larger when considering periods at even higher magnetic field (not shown in fig. 7.2). This is because the particles in the cone-shell structure are not physically constrained to a ring of fixed radius and thus the interplay between electric field, magnetic field and hole magnetic quantum number l_h is linked to a shift of the wavefunction center of mass. On the other hand, when $F = 30\,\mathrm{kV/cm}$, the oscillation period is almost constant as well. The analytical result obtained with both methods is $R = 46\,\mathrm{nm}$ and agrees well with the wavefunction center of mass obtained in the simulations. These results confirm that the system behaves very similarly to an ideal ring when a strong electric field is applied.

7.2 Exciton frame

The previous results in the single particle frame give a first idea of the system behaviour under the application of external electric and magnetic fields. To obtain a more realistic insight that can predict possible PL results, the electron-hole Coulomb interaction C_{eh} needs to be considered. In the following, the main observations resulting from including C_{eh} are outlined, along with a comparison with the Fock-Darwin model. All the results illustrated below are obtained by considering positive electric field and hence the formation of a hole

ring, while the electrons stay at the tip of the cone-shell structure. Analogous outcomes and analysis would apply when considering an electron ring, however, as explained in sec. 7.1, the effects induced by the fields on the holes are more apparent than on the electron for the same field value. The electron magnetic quantum number l_e is set to 0, which is the case when $F > 0$.

7.2.1 General observations: l, F and B dependence

The dependence of the position $z_{c,h}$ (on the z direction) of the hole wavefunction center of mass on the hole magnetic quantum number l_h is shown in fig. 7.4 for various fixed electric and magnetic field values.

For all magnetic and electric fields, an increase in $|l_h|$ causes the holes to be pushed further

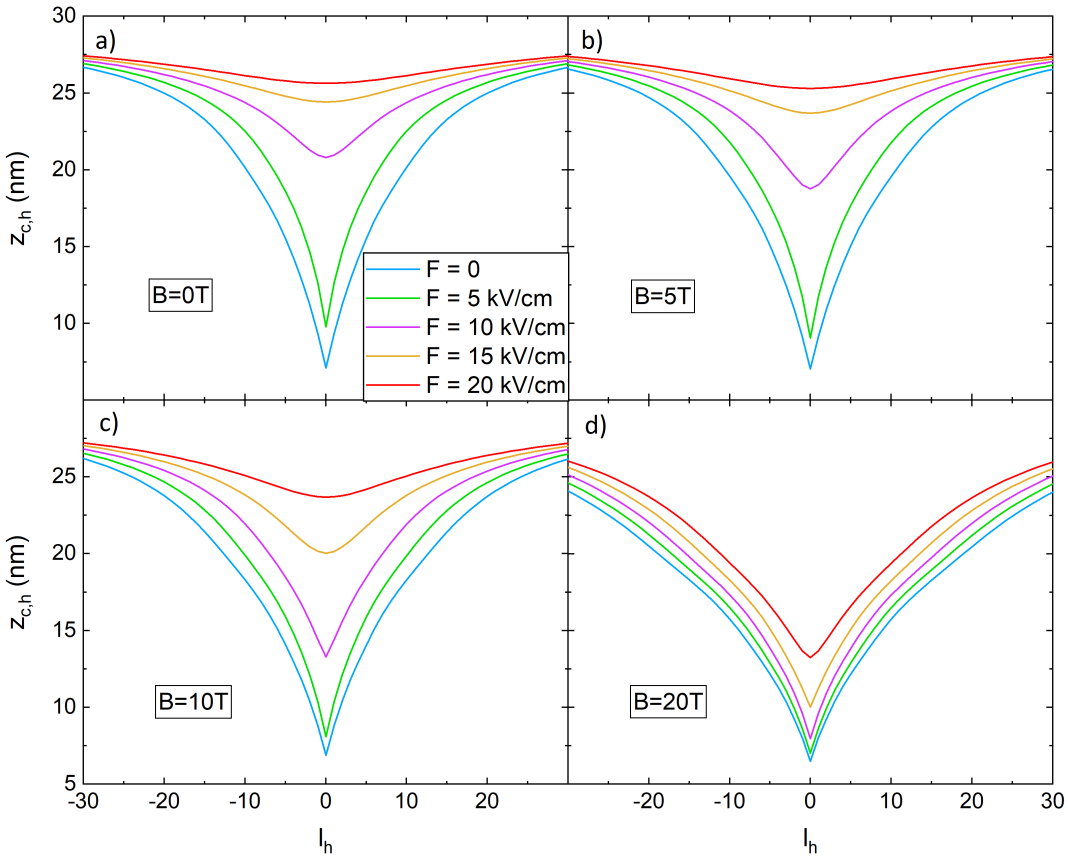

Figure 7.4: Hole wavefunction center of mass position $z_{c,h}$ as function of the hole magnetic quantum number l_h for fixed electric field F from 0 to 20 kV/cm (in steps of 5 kV/cm) and fixed (a) $B = 0$ T, (b) $B = 5$ T, (c) $B = 10$ T and (d) $B = 20$ T. The lines connecting the $z_{c,h}$ values associated to each discrete l_h value are guides to the eye.

towards the base of the cone-shell, increasing their separation with the electrons at the tip. As $|l_h|$ grows, $z_{c,h}$ approaches a maximum of about 27.5 nm imposed by the structural geometry (i.e. $h_{out} = 30\,\text{nm}$, fig. 4.6). Furthermore, all the plots are symmetric with respect to $l_h = 0$ and hence it can be inferred that the hole wavefunction center of mass position $z_{c,h}$ is independent of the sign of l_h. The magnetic quantum number l is associated to the circular current, from which the magnetic dipole, which interacts with the magnetic field, arises. Opposite l numbers indicate that the circular currents are rotating in opposite directions, which is equivalent to the situation in which the direction of the magnetic field B is reversed. Hence, $z_{c,h}$ is independent of the direction of the magnetic field.

When no magnetic field is applied (fig. 7.4a), considering the same hole magnetic quantum number l_h, the effect of the electric field F is evident. As F increases, the holes are pushed by repulsion towards the base of the structure, further away from the electrons. At $F = 20\,\text{kV/cm}$ (red line), the holes are far away from the cone-shell tip already for $l_h = 0$, hence why an increase in l_h causes only a very small shift in the wavefunction center of mass, as opposed to a more drastic shift, for example at 5 kV/cm (green line).

Comparing now lines obtained applying the same electric field, such as the red lines for $F = 20\,\text{kV/cm}$, it is noted that, for example, for $l_h = 0$ and at $B = 0\,\text{T}$ (fig. 7.4a), $z_{c,h} = 25.6\,\text{nm}$ whilst at $B = 20\,\text{T}$ (fig. 7.4b), $z_{c,h} = 13.2\,\text{nm}$. Similarly, at high $|l_h|$, the hole wavefunction center of mass position $z_{c,h}$ saturates at $B = 0\,\text{T}$ whilst it does not for $B = 20\,\text{T}$. The effect caused by the magnetic field B can then be inferred: contrary to the hole magnetic quantum number l_h and electric field F dependence of $z_{c,h}$, B tends to reduce $z_{c,h}$. In other words, as the magnetic field increases, the holes are pushed back towards the electrons at the tip of the cone-shell structure. It has to be noted that the directions in which the magnetic field and the electric field push the charge carriers are different. In fact, the single particle Hamiltonian shows that the magnetic field affects only the radial component r of the Hamiltonian whilst the electric field only the z component (eq. 4.1). However, due to the geometry of the system and the consequent coupling between z and r motion, a shift of the wavefunction center of mass in the r direction is linked to a shift also in the z direction.

The position of the wavefunction center of mass directly impacts the Coulomb interaction C_{eh}, which is plotted in fig. 7.5 as function of the hole magnetic quantum number l_h for various fixed electric field F and magnetic field B. For $l_h = 0$, which corresponds to the minimum hole wavefunction center of mass position $z_{c,h}$, the interaction shows a maximum[1],

[1]For all the simulations, the Coulomb interaction C_{eh} is calculated as a positive value and subtracted to get the exciton energy $E_X = E_g + E_e + E_h - C_{eh}$.

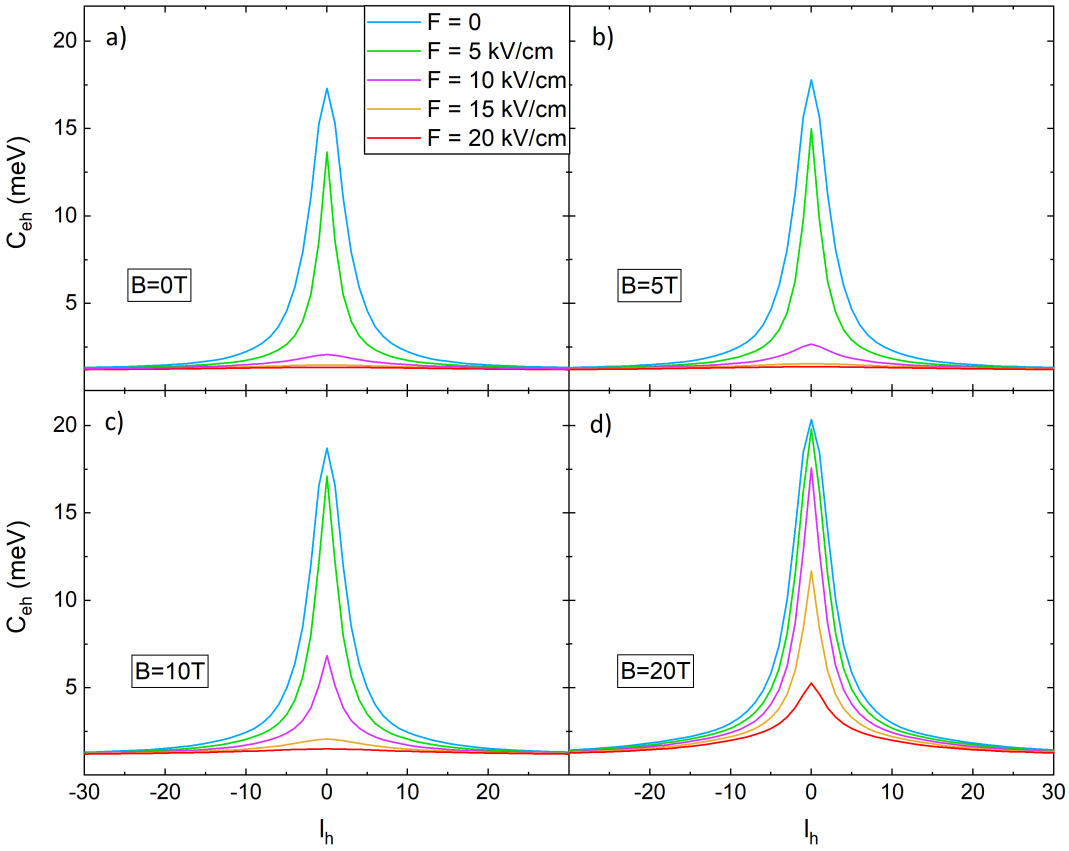

Figure 7.5: Electron-hole Coulomb interaction C_{eh} as function ofthe hole magnetic quantum number l_h for fixed electric field F from 0 to 20 kV/cm (in steps of 5 kV/cm) and fixed (a) $B = 0$ T, (b) $B = 5$ T, (c) $B = 10$ T and (d) $B = 20$ T. The lines connecting the C_{eh} values associated to each discrete l_h value are guides to the eye.

as the charge carriers are in the closest position allowed by the combination of the applied electric and magnetic fields. Without and at small magnetic field B, the peak in the red line associated with $F = 20$ kV/cm is not present or very small, as the effect of the strong electric field, pushing the carriers away from each other, overcomes the effect of the weak magnetic field, which tends to push the carriers closer. This indicates the formation of a hole ring well separated from the electrons at the tip of the structure.

Only when a strong magnetic field B is applied (fig. 7.5d) does the peak appear in the C_{eh} curve also at strong electric field. This is because the magnetic field is strong enough to compensate the effect of the electric field, reducing the distance between electron and hole wavefunction center of masses and causing the carriers to be influenced by the presence of each other.

Regarding the hole magnetic quantum number l_h dependence of the Coulomb interaction C_{eh}, it can be observed that, as $|l_h|$ increases, C_{eh} approaches about 2 meV. This can be expected by the l_h dependence of the hole wavefunction center of mass position $z_{c,h}$, described above. In fact, the holes move further up the cone-shell, forming a well-defined ring at large $|l_h|$. When a magnetic field is applied, the motion of the holes related to an increasing $|l_h|$ is less pronounced, as it is compensated by the effect of the magnetic field. Thus, the $|l_h|$ value at which the Coulomb interaction approaches 2 meV gets larger with increasing magnetic field.

Another observation that can be made from fig. 7.5 is that, similarly to $z_{c,h}(l_h)$, the $C_{eh}(l_h)$ plots are also symmetric with respect to $l_h = 0$, which indicates that the Coulomb interaction C_{eh} is independent of the sign of the hole magnetic quantum number l_h or the direction in which the magnetic field is applied.

Having now a clear idea of how the Coulomb interaction C_{eh} relates to l_h, F and B, the exciton energy E_X can be analysed. Its dependence on l_h is plotted in fig. 7.6 for various fixed electric and magnetic field values. In the plots, in particular in the one with no magnetic field (fig. 7.6a), the Stark-shift induced by the electric field is clear for high $|l_h|$ and it manifests as a shift of the energy lines to lower values as the electric field increases. The behaviour is more complex for low $|l_h|$. In fact, it can be observed that the plot at $B = 0\,\mathrm{T}$ shows a sharp minimum at $l_h = 0$ for $F = 0\,\mathrm{kV/cm}$ and $5\,\mathrm{kV/cm}$, which becomes smoother as the electric field F increases. The peak is associated to the maximum peak of $C_{eh}(l_h)$, which causes the drop in energy. Since C_{eh} as function of the hole magnetic quantum number l_h for strong electric field F, such as $F = 20\,\mathrm{kV/cm}$, is nearly flat (red line in fig. 7.5a), $E_X(l_h)$ is parabolic (red line), reflecting the single particle energy dependence on the magnetic quantum number l. To confirm the origin of the parabolic behaviour, the energy curve is compared to the kinetic term $(c_h/r^2)l_h^2$ of the single particle Hamiltonian (eq. 4.2), where $c_h \simeq 7.47 \times 10^{-20}\,\mathrm{eV\,m^2}$. The quadratic term is indicated with a dashed line in fig. 7.6a, with an offset to account for the electric field induced shift. The almost perfect fit confirms that the energy dispersion at $F = 20\,\mathrm{kV/cm}$ arises from the single particle energy.

When a magnetic field B is applied (fig. 7.6a to d), the minimum of the energy curves at high electric field F is obtained for higher hole magnetic quantum number l_h as the magnetic field increases, which also agrees with the single particle behaviour, as explained in sec. 7.1. The sharp minimum, which at $B = 0\,\mathrm{T}$ is present only at low electric field F, starts to appear also at higher F as the magnetic field increases. From the earlier explanation, this is associated to the increasingly stronger Coulomb interaction C_{eh} resulting from the

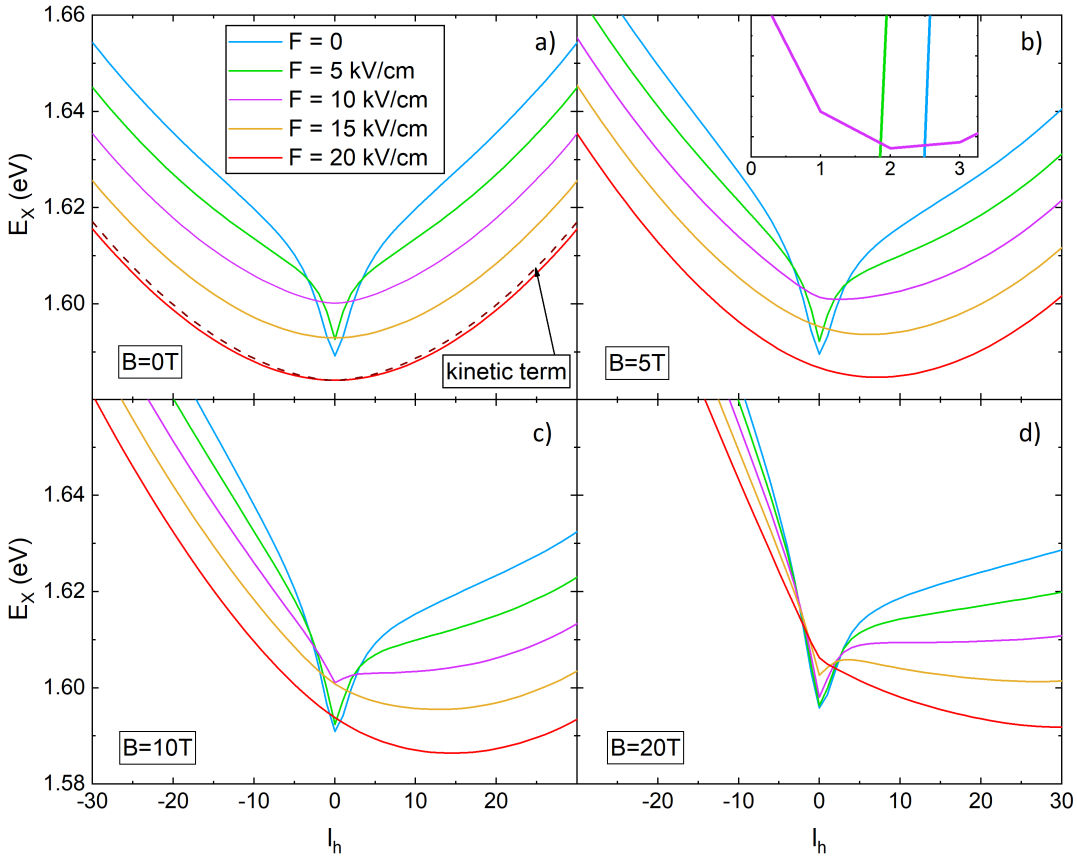

Figure 7.6: Exciton energy E_X as function of the hole magnetic quantum number l_h for fixed electric field F from 0 to 20 kV/cm (in steps of 5 kV/cm) and fixed (a) $B = 0$ T, (b) $B = 5$ T, (c) $B = 10$ T and (d) $B = 20$ T. The dashed line in (a) shows the single particle Hamiltonian kinetic term with an offset to account for the shift caused by $F = 20$ kV/cm. Inset in (b): zoom-in of $E_X(l_h)$ plot at 5 T, the minimum of the $E_X(F = 10\,\text{kV/cm})$ curve is at $l_h = 2$. The lines connecting the E_X values associated to each discrete l_h value are guides to the eye.

magnetic field overcoming the effect of the electric field.

An interesting observation can be made for the energy curve at $F = 10$ kV/cm (pink line): when no magnetic field is applied, the minimum is at $l_h = 0$; then, as the magnetic field increases to 5 T, the minimum shifts to $l_h = 2$ (inset of fig. 7.6b), as would be expected from the single particle frame. However, at $B = 10$ T, when the Coulomb interaction C_{eh} becomes strong, the l_h at which the minimum is obtained drops again to 0 and remains 0 when further increasing the magnetic field. This is caused by the fact that, with increasing magnetic field, larger l_h lead to smaller energies in the single particle frame (i.e. larger l_h are preferred), whilst the Coulomb interaction C_{eh} tends to smaller l_h, since, as previously

discussed, at higher l_h, $z_{c,h}$ is larger and hence the electron-hole separation also increases, thus reducing C_{eh} and increasing E_X. The counteracting tendencies of the single particle energies and the Coulomb interaction, depending on the applied electric and magnetic fields, can lead to a sudden jump of the ground state l_h back to 0, as observed for the $F = 10\,\mathrm{kV/cm}$ case in fig. 7.6. This behaviour is studied in more details later.

An additional consideration that can be made is related to the symmetry of the plots. As noticed earlier, the $z_{c,h}$ and C_{eh} plots as functions of the hole magnetic quantum number l_h are symmetric regardless of the electric and magnetic fields. In contrast, the energy plot is symmetric only for $B = 0\,\mathrm{T}$. As the magnetic field increases, the plots become increasingly asymmetric and the energies associated with positive l_h decrease whilst the ones associated with negative l_h increase. The energy plots suggest a classical analogy of the system[2]. However, the symmetric behaviour of $z_{c,h}$ and C_{eh} contradicts this analogy. In fact, classically, when the magnetic field is applied in one direction, the centrifugal force and the Lorentz force add up and when the magnetic field is reversed, the two forces counteract each other. Consequently, an asymmetry would be expected not only for E_X but also for $z_{c,h}$ and C_{eh} as function of the magnetic field B or of the hole magnetic quantum number l_h, which is not reflected in the non-classical results. The classical view can only explain the results for $B = 0\,\mathrm{T}$, where no Lorentz force needs to be considered.

Althoug the classical analogy cannot be applied, the symmetry of the hole wavefunction center of mass position $z_{c,h}$ is indeed expected when studying the Hamiltonian of the system (eq. 4.2). Considering the case where $F = 0\,\mathrm{kV/cm}$ for simplicity, the system potential $V(r, z)$ (fig. 7.7) is

$$V(r, z) = V_i - \frac{\hbar e B l}{2m_i} + \frac{e^2 B^2 r^2}{8m_i}. \tag{7.4}$$

V_i is 0 in the QD and a constant outside (see ch. 4) and is indicated with a black line in fig. 7.7. When a magnetic field is applied, the potential (orange line) increases parabolically as function of r (from the last term which is proportional to r^2). Hence, the locations in the cone-shell with large r, and hence large z, are energetically unfavourable. This is related to

[2]Classical view - Hole circulating around an electron fixed in the $z = 0$ plane: the higher the angular momentum, the larger the centrifugal force which drives the hole and electron away from each other, leading to an increase in the separation at higher magnetic quantum number l. There are two competing forces, the centrifugal force F_C, caused by the hole rotating around the electron, and the Lorentz force F_L, caused by the magnetic field. Opposite l signs indicate opposite magnetic field directions (i.e. if both l and B are reversed in sign, the same results are obtained). Considering, for example, B applied from the tip to the base of the cone-shell ($B > 0$), with increasing $|l_h|$ on the negative l_h side, F_L is expected to add up to F_C, pushing the wavefunction further out and thus increasing the ring radius and $z_{c,h}$, hence reducing the Coulomb interaction C_{eh} and leading to an increasing exciton energy E_X, whilst, with increasing $|l_h|$ on the positive l_h side, F_L is expected to counteract the effect of F_C, pushing the hole wavefunction back towards the centre, thus reducing $z_{c,h}$, increasing C_{eh} and leading to a decreasing exciton energy E_X.

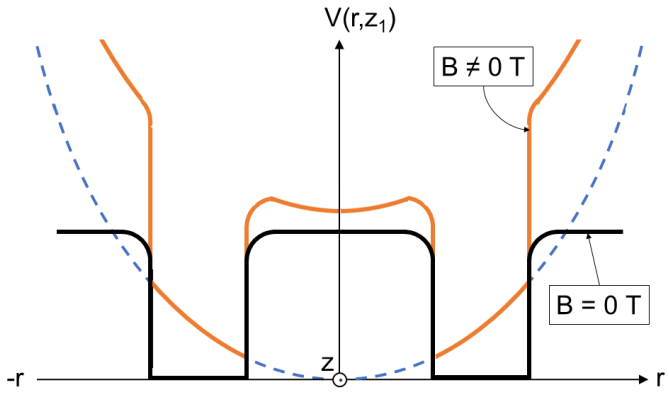

Figure 7.7: Sketch of the cross-section of the potential $V(r, z)$, without and with magnetic field B (black and orange lines, respectively). No external electric field is applied.

the carriers being pushed back towards the tip of the cone (i.e. increasing magnetic field B decreases $z_{c,h}$). This term is l-independent whilst the 2^{nd} term is the only term containing both B and l, but it has no spatial coordinate. This means that the magnetic quantum number l does not change the overall behaviour of the potential when a magnetic field is applied, it only shifts the parabola up or down. Hence, the $z_{c,h}(l_h)$ symmetry is expected and, being it directly related to the Coulomb interaction C_{eh}, the symmetry of C_{eh} is also expected from the formula.

7.2.2 Comparison with Fock-Darwin model

The Fock-Darwin model describes the energy spectrum of a single particle as function of magnetic field B, assuming that the QD is flat, such that the principal quantum number in the z direction, n_z, is 0 and hence the particle is always in the ground state for motion in this direction, and, for the remaining spatial coordinates, assuming a radially symmetric parabolic confinement potential in polar coordinates. The resulting eigenenergies of the Fock-Darwin states, are indicated in eq. 3.20. A comparison between the Fock-Darwin model and the energy plots obtained for the cone-shell QD can give some further insight into the characteristics of this particular structure.

The exciton energy at $B = 20\,\mathrm{T}$ is plotted as function of the hole magnetic quantum number l_h in fig. 7.8. Since the FD model does not include electric field, all the computations are performed with $F = 0\,\mathrm{kV/cm}$ and hence the model is compared to the simulation case in which the hole wavefunction is at the tip of the cone-shell structure when $l_h = 0$. All the energies are calculated with $n = 0$ and they have an offset such that $E_X(l_h = 0) = 0$ for better comparison. The energy without considering the Coulomb interaction C_{eh} (dashed

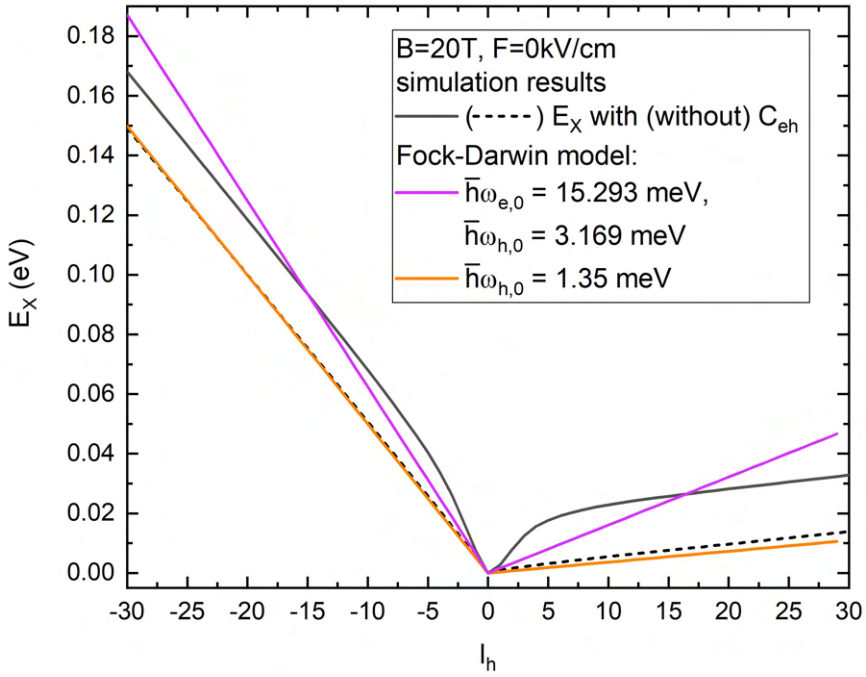

Figure 7.8: Exciton energy as function of the hole magnetic quantum number l_h with (black full line) and without electron-hole interaction (black dashed line) and exciton energy given by the sum of the single-particle energies obtained using FD model for $B = 20\,\mathrm{T}$ and no electric field F (coulored lines). Each line is obtained using the indicated quantisation energies in the FD equation. All plots have an offset obtained by subtracting $E_X(l_h = 0)$. l_e and n are both fixed to 0. The lines connecting the E_X values associated to each discrete l_h value are guides to the eye.

black line) can be compared to the FD model result (coloured lines) as the FD model does not include electron-hole interaction. The FD states are obtained by summing the energy contributions obtained by using eq. 3.20 for electron and hole. The quantisation energies $\hbar\omega_{j,0} = E_{j,n=1} - E_{j,n=0}$ are obtained from the simulation results using the model described in ch. 4 and are $E_{e,0} = 15.293\,\mathrm{meV}$ and $E_{h,0} = 3.169\,\mathrm{meV}$ for electron and hole respectively (violet line). Comparing the black dashed line and the violet line, it can be noted that the slopes for both negative and positive hole magnetic quantum number l_h is smaller for the cone-shell than for the perfectly symmetric QD case. In both cases, the electron magnetic quantum number l_e is set to 0, hence the electron wavefunction is located at the centre of the structure. On the other hand, in the cone-shell QD, the varying l_h pushes the hole wavefunction towards the sides and an increasing l_h leads to a hole wavefunction shape that increasingly resembles an ideal ring, which is not the case for the FD model case. The deviation in shapes and potentials can be linked to the discrepancy in the $E_X(l_h)$ plot. A fit of the FD model (orange line) is performed to find the hole quantisation energy leading to the best match with the simulation results. The electron quantisation energy $E_{e,0}$ is not

changed as it does not influence the slope of the $E_X(l_h)$ plot when $l_e = 0$ (eq. 3.20), but it only causes a shift of the plot, which is removed by the offset in the plot. The closest match is obtained by setting $E_{h,0} = 1.35\,\text{meV}$. As mentioned, the disagreement is connected to the fact that the FD model considers a parabolic potential, whilst the cone-shell QD potential is not parabolic.

The deviation from the model induced by the inclusion of the Coulomb interaction C_{eh} is also analysed. The exciton energy E_X with C_{eh} is plotted as function of the hole magnetic quantum number l_h in fig. 7.8 (solid black line). As could be expected from the analysis in sec. 7.2.1, the deviation from the FD model consists in a dip in the plot close to $l_h = 0$. This is associated to the strong peak in C_{eh} around this value (see blue line in fig. 7.5d) which, being subtracted from the total energy, leads to the dip. As the holes are pushed towards the sides with increasing hole magnetic quantum number l_h, C_{eh} decreases leading the slopes of the FD model and the $E_X(l_h)$ plot obtained by simulations to be equal towards large l_h values.

The wavefunction analysed so far in this section is for $F = 0\,\text{kV/cm}$. As already observed, when an electric field F is applied, the energy dispersion drastically changes due to the formation of a quantum ring and cannot thus be explained by the FD model of a dot. In fact, whilst for the QD case (i.e. with no external electric field applied) the energy is linearly dependent on the hole magnetic quantum number l_h, as is evident from fig. 7.8, when an electric field is applied and the holes form a ring, $E_X \propto l_h^2$ (ch. 3). This can be seen in fig. 7.6 and is discussed in sec. 7.2.1.

7.2.3 Luminescence control through F and B fields

Bringing together all the observations discussed in this chapter allows to make some predictions about the QD luminescence. To better discuss these, the results can be organised in two regimes: a high electric field regime for $F \geq 10.5\,\text{kV/cm}$, where the holes form a well defined ring, and a low electric field regime for $F < 10.5\,\text{kV/cm}$, where the holes form a hybrid system. In the following, the two regimes are analysed in depth and the PL emission is discussed for each.

7.2.3.1 High F regime: quantum ring

For $F \geq 10.5\,\text{kV/cm}$, the holes are strongly pushed towards the base of the cone-shell structure, forming a well defined ring, whilst the electrons stay at the tip. The ground state exciton energy $E_{X,0}$, the electron-hole interaction and the hole magnetic quantum number l_h are plotted in fig. 7.9a, b and c as functions of magnetic field B for fixed electric field F.

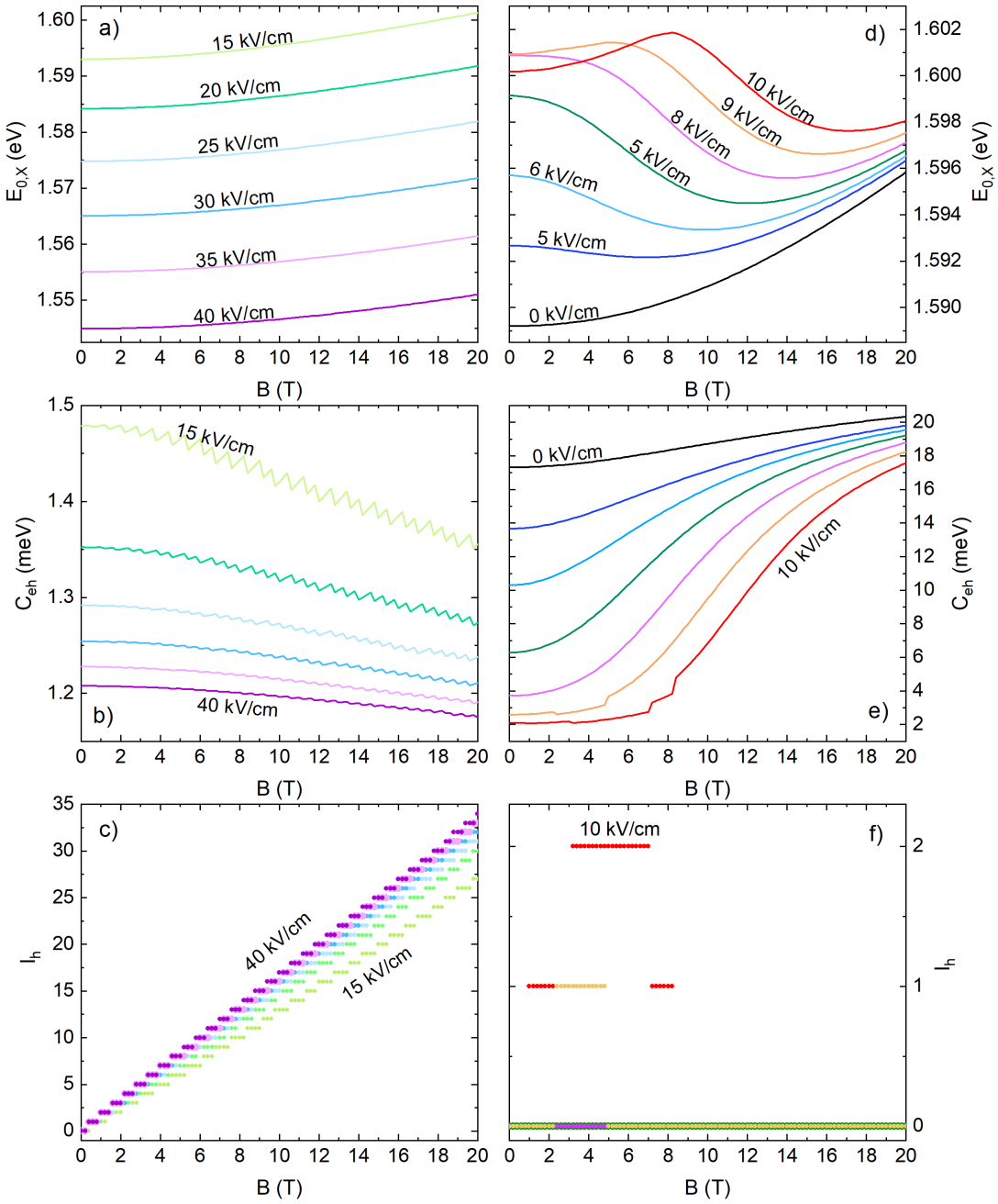

Figure 7.9: (a, d) Ground state exciton energy $E_{X,0}$, (b, e) Coulomb interaction C_{eh} and (c, f) hole magnetic quantum number l_h as function of the magnetic field B and for fixed electric field F as indicated in (a) and (d) (the colour code is consistent throughout the plots). The plots on the left are for the high electric field regime ($F \geq 10.5\,\mathrm{kV/cm}$) whilst the right side plots are for the low electric field regime ($F < 10.5\,\mathrm{kV/cm}$). The results are obtained for $l_e = 0$ and for l_h computed for the lowest exciton energy E_X considering C_{eh}.

The plotted results are obtained by fixing the electron magnetic quantum number l_e to 0, since all the considered electric field values are positive. The value used for the hole magnetic quantum number l_h is the one that gives the minimum exciton energy when including the Coulomb interaction C_{eh}.

From the ground state energy plot (fig. 7.9a), it can be noted that the Stark-shift dominates, red-shifting each energy line as the electric field F increases.

Furthermore, each line moves upwards as the magnetic field increases. To understand this behaviour all the energy contributions are plotted separately in fig. 7.10a for $F = 40\,\mathrm{kV/cm}$. It can be observed that the steep increase in the exciton ground state energy (black line) is mainly caused by the electron energy dispersion (blue line), reflecting the diamagnetic shift of the electrons in the dot when the external magnetic field increases. The hole contribution (red line) is very small due to the larger effective mass and hence only slightly increases the slope of $E_{X,0}(B)$. It is also noticeable that the variation in the Coulomb interaction C_{eh} from $B = 0\,\mathrm{T}$ to $20\,\mathrm{T}$, relative to the other energies, is extremely small (green line) since the holes are well separated from the electrons due to the strong electric field F, regardless of the magnetic field. The inset shows a zoom-in of the ground state exciton energy $E_{X,0}$ and the hole ground state energy in the single particle frame (violet line) and in the exciton frame (i.e. calculating l_h for minimum exciton energy E_X including interaction, red line). The discrepancy between the hole ground states in the two frames is caused by the different l_h that gives the ground state in the two frames as a consequence of taking into account the Coulomb interaction C_{eh}, which has a very small but yet non-zero variation as function of magnetic field B, as can be better appreciated in fig. 7.9b. The inset of fig. 7.10a also reveals AB oscillations in both the hole and the exciton energy lines. These are discussed in details later.

From fig. 7.9b, it can also be noted that the variation in C_{eh} from $B = 0\,\mathrm{T}$ to $20\,\mathrm{T}$ increases as the electric field decreases, which, from the discussion in sec. 7.2.1, is expected, since for smaller electric field the counteracting effect of the magnetic field pushing the holes closer to the electrons becomes more prominent.

To predict the intensity of the PL emission, the following clarification must be made about the approach used for the computation. The electron and hole wavefunctions $\Psi_{e,0}(\vec{r})$ and $\Psi_{h,0}(\vec{r})$ have, in addition to a r and a z-dependent function, also a ϕ-dependent function ($e^{i\phi l_e}$ and $e^{i\phi l_h}$ for the electron and the hole respectively). The overlap integral I_{eh} is given by eq. 4.3, where the product of the wavefunctions is integrated over r, z and ϕ. However, for the simulations presented in this thesis, the overlap integral is computed integrating only

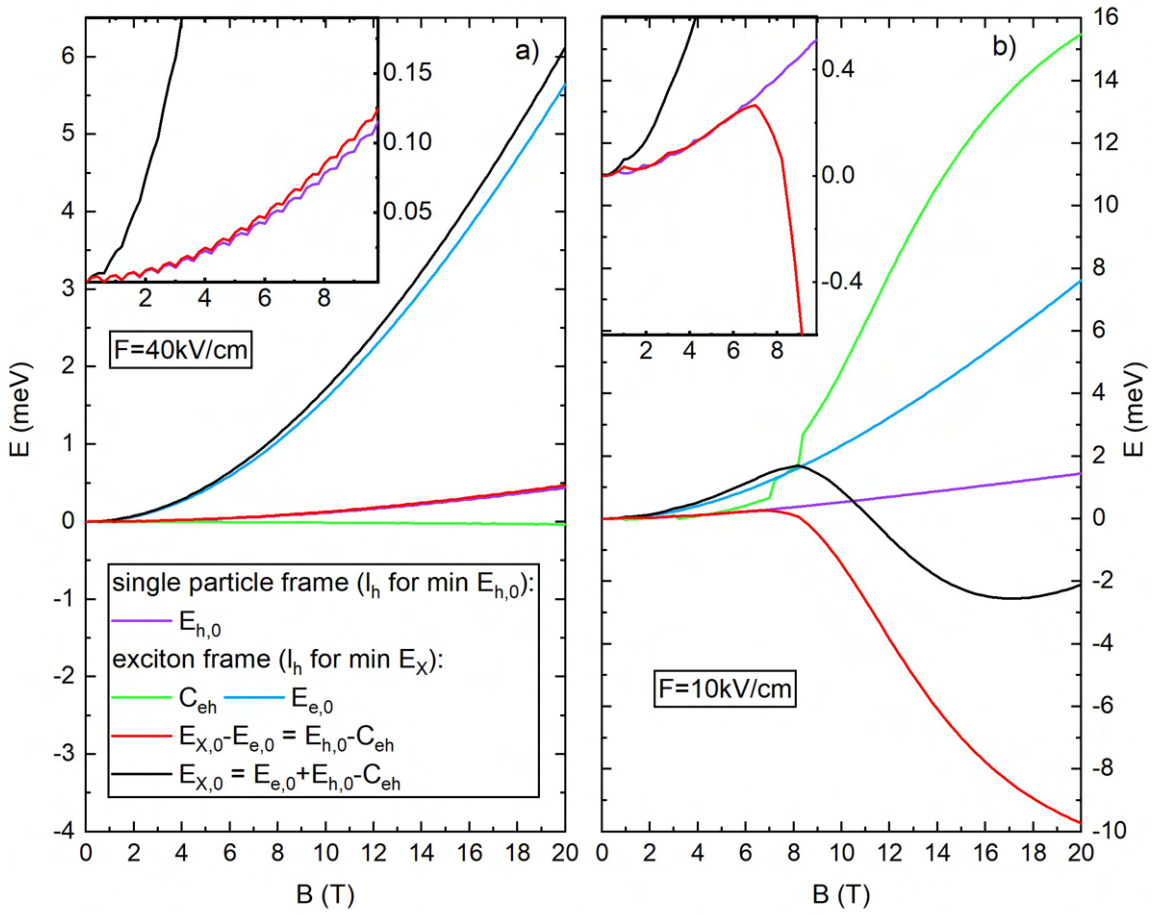

Figure 7.10: Hole ground state energy (violet) in the single particle frame, where l_h is computed for minimum hole energy and hole ground state in the exciton picture with C_{eh} (red, i.e. l_h is computed for minimum exciton energy E_X including interaction, then the electron ground state energy is subtracted to E_X, hence obtaining $E_{h,0} - C_{eh}$). Electron ground state energy in the exciton frame (blue), exciton ground state energy (black) and Coulomb interaction (green). All the energies are as function of magnetic field B at fixed electric field (a) $F = 40\,\mathrm{kV/cm}$ and (b) $F = 10\,\mathrm{kV/cm}$. The results are obtained for $l_e = 0$ and for l_h computed for the lowest E_h (single particle frame) or the lowest exciton energy E_X considering the Coulomb interaction C_{eh} (exciton frame). All energies are with offset to have $E(B = 0\,\mathrm{T}) = 0\,\mathrm{meV}$. The two insets show a zoom-in from $B = 0\,\mathrm{T}$ to $10\,\mathrm{T}$ of the exciton energy and the hole energy in both frames.

over r and z, but not the angular dimension ϕ. From this point, the so obtained overlap integral is named I'_{eh} to distinguish it from the overlap integral I_{eh} which considers the ϕ. It should be noted that, to calculate the PL intensity, both I'_{eh} and the angular momenta need to be considered. However, when the condition $l_e = l_h$ is satisfied, I'_{eh} is sufficient to calculate the PL intensity and related parameters, such as the recombination lifetime. The other parameters discussed up to this point and below, such as the energies, are not affected by the mentioned issue, since they are computed from the probability distribution where

the wavefunction is squared. An important implication deriving from this discussion and by observing fig. 7.9c is that the luminescence is expected only at low magnetic field, when $l_e = l_h$. For example, at $F = 15\,\mathrm{kV/cm}$, $l_h = l_e = 0$ only up to about $0.4\,\mathrm{T}$ and, beyond this threshold value of the magnetic field, l_h gradually increases and hence no luminescence is expected as $l_h \neq l_e$. Depending on the applied electric field F, the threshold value decreases. For example, at $40\,\mathrm{kV/cm}$, luminescence is expected only up to $B = 0.2\,\mathrm{T}$. The possibility of switching off the luminescence suggests the cone-shell system for light storage.

7.2.3.2 Low F regime: QD and hybrid system

The low electric field regime has major differences with respect to the high field case. $E_{X,0}$, C_{eh} and l_h at low fixed electric field F are plotted in fig. 7.9d, e and f as function of electric field F. As before, the results are obtained for fixed $l_e = 0$ and l_h computed for the minimum exciton energy E_X including C_{eh}.

When $F = 0\,\mathrm{kV/cm}$, both the electron and the hole are at the tip of the cone-shell structure and a QD behaviour is observed for both the energy dispersion and the Coulomb interaction as function of magnetic field (black line in fig. 7.9d and e): l_h for which the ground state exciton energy $E_{X,0}$ is obtained has no variation, it remains 0 for the whole magnetic field range since no ring is formed. The Coulomb interaction C_{eh} shows a slight variation from $17.3\,\mathrm{meV}$ at $0\,\mathrm{T}$ to $20.3\,\mathrm{meV}$ at $20\,\mathrm{T}$, as a consequence of the magnetic field pushing the charge carriers closer to each other.

When a non-zero $F < 10.5\,\mathrm{kV/cm}$ is applied, the holes are pushed to the sides of the structure. However, in contrast to the high electric field regime, they are still bound to the electrons at the tip. Hence, a hybrid system between a QD and a quantum ring is formed. In this regime, the Stark-shift is reversed and the energy increases with increasing electric field, as opposed to the high field regime. The Stark-shift starts inverting to the high field behaviour above $F = 9\,\mathrm{kV/cm}$, starting from low magnetic field B.

Furthermore, the exciton energy dispersion as function of magnetic field B is fundamentally different from the energy in the high field regime. Below $8.5\,\mathrm{kV/cm}$, the energy first decreases and then starts increasing again. This is associated to an increasing Coulomb interaction C_{eh}.

As for the QD case at $F = 0\,\mathrm{kV/cm}$, the hole magnetic quantum number l_h remains 0 for the whole magnetic field range. When the electric field F is between $8.5\,\mathrm{kV/cm}$ and about $10\,\mathrm{kV/cm}$, the ground state exciton energy $E_{X,0}$ first increases, reaches a peak, decreases and then slowly increases again merging into the tail with the energy lines at other fixed

electric field F.

To analyse this trend in details, the ground state energy contributions are plotted separately in fig. 7.10b for $F = 10\,\mathrm{kV/cm}$, with an offset to have all the energy lines starting at $0\,\mathrm{meV}$ for $B = 0\,\mathrm{T}$. Studying the figure, it can be seen that initially (below about $6\,\mathrm{T}$), the change in the Coulomb interaction C_{eh} is very small (about $0.4\,\mathrm{meV}$) and the contribution given by $E_{0,h}$ is negligible. Hence the initial rise in the ground state exciton energy $E_{X,0}$ can be associated to the electron energy dispersion. At about $B = 8\,\mathrm{T}$, C_{eh} sharply increases as the magnetic field becomes strong enough to push back the holes towards the electrons. This causes $E_{X,0}$ to drop. At around $16\,\mathrm{T}$, the slope of C_{eh} gradually decreases, whilst $E_{e,0}$ continues to steadily increase and hence starts dominating over the Coulomb interaction C_{eh}, leading to an increase in the ground state exciton energy $E_{X,0}$. The hole ground state energy $E_{h,0}$ calculated in the exciton picture (i.e. with l_h computed for minimum exciton energy) is also shown (red line) including C_{eh}, to directly see the influence of the Coulomb interaction on the hole energy. A zoom-in of this line up to $8\,\mathrm{T}$, along with the $E_{h,0}$ in the single particle frame (violet line) and $E_{X,0}$ for comparison, are shown in the inset. It can be noted that $E_{h,0}$ lines in the two frames are close, although not perfectly overlapping, up to about $8\,\mathrm{T}$, when the Coulomb interaction C_{eh} is still low. Moreover, the zoom-in reveals AB oscillations in the hole as well as in the exciton energy, which are discussed in details later. Comparing the energy lines in the inset, it can be observed that the oscillations period is larger in the exciton frame than in the single particle frame. Considering that, for an ideal ring, the oscillations period is proportional to $1/R^2$, with R the ring radius, it could be inferred that the inclusion of the electron-hole interaction leads to a reduction of R.

Moving to the analysis of the PL intensity, and considering the overlap integral I'_{eh} discussed earlier, the following observations can be made analysing fig. 7.9f. Below $F = 8.5\,\mathrm{kV/cm}$, luminescence from the recombination of the ground state exciton in the hybrid quantum system is expected to be visible for any applied magnetic field, since $l_h = l_e = 0$ throughout the whole range of the magnetic field B. The lifetime is expected to increase as the magnetic field increases. The difference in lifetime at low and high magnetic field is larger for larger electric field F (plot not shown).

Different is the situation when an electric field between $8.5\,\mathrm{kV/cm} \lesssim F < 10.5\,\mathrm{kV/cm}$ is applied. Taking as an example the case for $F = 10\,\mathrm{kV/cm}$, the variation of the hole magnetic quantum number l_h associated to the minimum exciton energy E_X (including interaction, in red, and without interaction, in black) is shown in fig. 7.11 as function of magnetic field B. Whilst the minimum l_h gradually increases when the Coulomb interaction C_{eh} is not

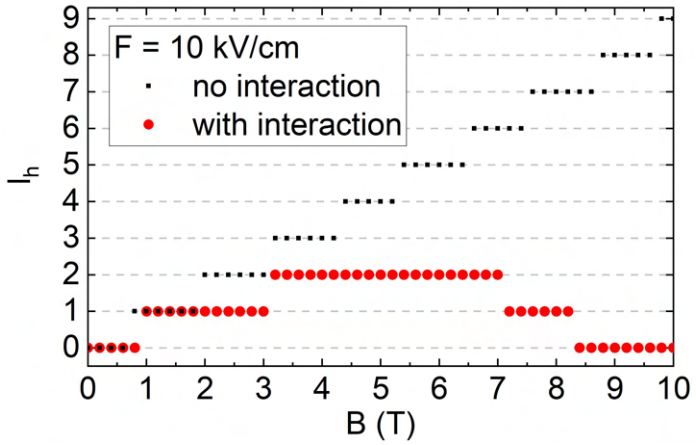

Figure 7.11: l_h number for minimum $E_{X,0}$ when including and not including the Coulomb interaction C_{eh} (red and black dots respectively). The hole magnetic quantum number l_h is plotted as function of magnetic field B and at fixed electric field $F = 10\,\mathrm{kV/cm}$.

considered, when the interaction is included l_h is first 0, rises to 1 at about $B \simeq 1\,\mathrm{T}$ and to 2 at about 3.2 T, then drops again to 1 at 7.2 T and back to 0 at 8.4 T. This means that, according to the $l_e = l_h$ selection rule, initially (below 1 T) luminescence is expected, this then disappears as $l_h \neq l_e$ but then re-occurs from 8.4 T onward. The value of the magnetic field at which the luminescence is switched off and on varies depending on the applied electric field F. For example, at $F = 9\,\mathrm{kV/cm}$ the luminescence is off between about 2.2 T and 5 T. Hence, by combining the electric and magnetic fields, the occurrence of the luminescence from the hybrid nanostructures can be precisely controlled, which again suggests the cone-shell QD systems for applications as light storage.

7.3 Aharonov-Bohm oscillations

When considering QDs in a magnetic field, a strong research interest is given to the possibility of observing excitonic AB oscillation. Since excitons are neutral particles, no AB oscillations would be expected, with the exception of faint oscillations caused by tunneling effects [101]. However, excitons are also polarisable composite particles and the area between hole and electron trajectories determines the excitonic phase. In a ringlike nanostructure, electrons and holes move over different trajectories, resulting in a non-zero electric dipole moment, which would result in AB oscillation in the exciton energy spectrum [140, 141].

In the cone-shell QDs, thanks to the strong lateral spatial separation induced by applying an external electric field F to the cone-shell nanostructure, the difference in trajectories is highly enhanced. In this section, the AB oscillations observed in the simulations of this structure is studied and compared to the literature.

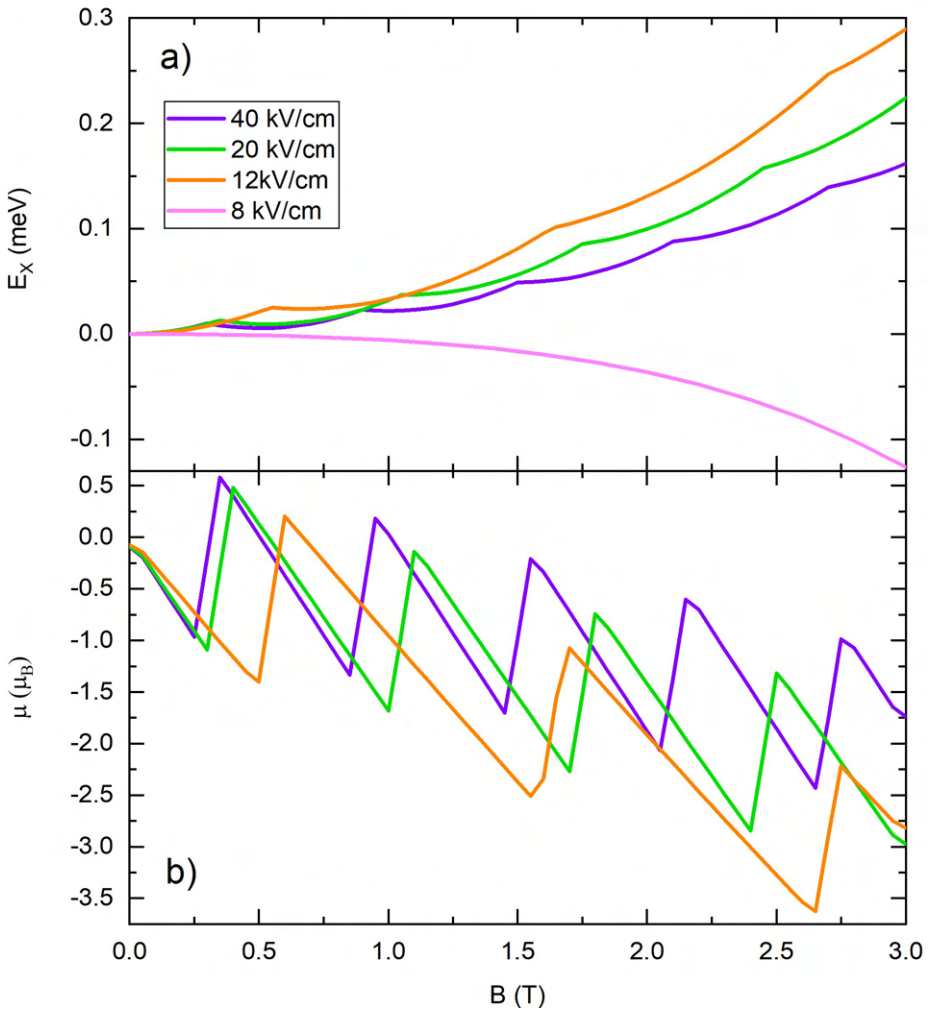

Figure 7.12: (a) Simulated exciton energy as function of magnetic field B at fixed electric field F as indicated; (b) first derivative (magnetic moment in units of Bohr magneton) of the energy with respect to B, with F as indicated in (a).

The ground state exciton energy $E_{X,0}$ is plotted as function of magnetic field B in fig. 7.12a for magnetic field B up to 3 T and for fixed electric field F as indicated. For better comparison, the energies have an offset such that $E_{X,0} = 0\,\text{eV}$ when $F = 0\,\text{kV/cm}$. The AB oscillations are clearly visible. The largest oscillation period is observed for the 12 kV/cm energy line, and it decreases with increasing electric field F. The amplitude of the oscillations, on the other hand, appears to slightly increase with increasing F. For 12 kV/cm, the oscillation amplitude is larger for lower magnetic field B and gradually decreases as the magnetic field increases (this is better visible in energy plots that consider a wider range of B, not shown here). This is caused by the fact that the magnetic field brings the hole closer to the tip, reducing the spatial separation with the electron. For very strong electric field F (see 40 kV/cm) the oscillations are almost constant in amplitude since the magnetic field

B is not strong enough to overcome the effect of the electric field, and hence the separation is almost unchanged.

The first derivative of $E_{X,0}$ with respect to magnetic field B is plotted in fig. 7.12b for fixed $F = 12\,\mathrm{kV/cm}$, $20\,\mathrm{kV/cm}$ and $40\,\mathrm{kV/cm}$. This is the magnetic moment μ induced by the ground state persistent current as a function of magnetic field B and is given by

$$\mu = -\frac{\partial E}{\partial B}. \tag{7.5}$$

In the plot, the sharp jumps of μ are caused by the transition of the ground state from $l_h = 0$ to higher angular momentum states. The behaviour described above is now evident, with the strongest variation for $12\,\mathrm{kV/cm}$. In an ideal case, the jumps in the magnetic moment μ should have infinite slope (vertical lines) as the sign should change instantaneously at each oscillation of E_X. The finite slope between the jumps observed in fig. 7.12b are caused by low numerical accuracy.

Although the ground state exciton energy E_X shows clear AB oscillations in the simulation results, the selection rules discussed in the previous section must be taken into account when considering the possibility of experimentally observing PL emissions. In fact, since l_h must be equal to l_e to obtain a bright state, only the first ground state oscillation period is expected to be visible.

It is nevertheless interesting to discuss the theoretically predicted oscillations, including the dark states, to gain further insight on the cone-shell system and how it compares to systems reported in the literature. Many theoretical studies of the AB oscillations have been reported on QDs with various shapes and compositions [141–143], however, most of the results obtained in the literature are for either single electrons [144] or two interacting electrons [145]. Among the few studies on excitonic AB oscillations, one reporting about volcano-shaped GaAs QDs in AlGaAs barrier [146], where a quantum ring is obtained also by applying an external electric field, is comparable to the present study, for the materials and the method used. As opposed to the AB oscillations reported for the volcano-shaped QDs, which are visible only with second derivative, the oscillations obtained in the simulations of the cone-shell QDs, albeit still weak, can be directly observed in the exciton energy spectrum (fig. 7.12a). Also, much lower magnetic field is needed to see the oscillations: for example, the first oscillation for the cone-shell structure at $F = 12\,\mathrm{kV/cm}$ is obtained already below $1\,\mathrm{T}$ whilst in the volcano-shaped QD the earliest oscillation is for $F = 250\,\mathrm{kV/cm}$ and needs more than $12\,\mathrm{T}$ [141]. It must be reminded that the present model does not include CI, which instead is considered in the model used for the computation of the energy in

the volcano-shaped structure. Further work needs to be done to include CI in the present model, which could cause a reduction of the AB oscillations. If the effect of the CI is shown to be negligible, the cone-shell structure is expected to show more prominent excitonic AB effect than the structure studied in the literature.

7.4 Summary

The influence of an external magnetic field B applied vertically on a cone-shell QD, alongside the application of an external electric field F, is studied in this chapter through simulations. Since the influence of the magnetic field is stronger on holes than on electrons, due to the larger effective mass of the holes, only positive electric fields, which cause the formation of hole quantum rings in the cone-shell nanostructures, are considered. An increasing magnetic field causes the transition of the hole magnetic quantum number associated to the lowest energy state from 0 to higher values. This leads to an oscillating behaviour in the exciton ground state energy (AB oscillations), with the first oscillation expected already at relatively low magnetic fields. For example, when an electric field of 12 kV/cm is applied, a magnetic field of less than 1 T gives rise to the first oscillation in the energy dispersion. However, due to selection rules, only the vanishing of the photoluminescence would be observed and, under some conditions, its recurrence at higher magnetic field. The recurrence is obtained for electric fields below 10 kV/cm, due to the formation of a hybrid system between QD and quantum ring, and it can be finely controlled by tuning electric and magnetic fields. The possibility of switching off the luminescence and, in the low field regime, also to switch it on again, suggests the cone-shell QDs for application in quantum technologies as quantum memory.

Chapter 8

Conclusion and outlook

In this thesis, the optical properties of GaAs QDs made by the LDE method in an AlGaAs barrier are studied at different temperatures and in electric as well as magnetic fields.

In ch. 5, ensemble PL emissions from QDs of different density are investigated at and close to room temperature. The results obtained show that samples containing only one layer of high density QDs have an only weak QD emission. A proper layer design can significantly improve the emission from the QDs and reduce the substrate PL. When the AlGaAs barrier on top of the GaAs substrate is thin, the substrate luminescence hinders the observation of the emission from the QDs. Hence, a design with an AlGaAs layer thicker than the penetration depth of the exciting laser is recommended and is shown to lead to a considerable improvement and clear observation of QD PL at room temperature T_R. An alternative way to reduce the GaAs background emission is to reduce the penetration depth by using an excitation laser with a shorter wavelength. In this work, a blue laser (405 nm), as opposed to an usual green laser (532 nm), is shown to lead to the observation at T_R of QD excited states also for samples with a thin AlGaAs barrier. However, on the other hand, when using a blue laser instead of a green one, the higher absorption causes a reduction of the excitation intensity and, consequently, also of the QD PL intensity.

The temperature dependence of the integrated QD PL intensity is analysed. The intensity is observed to be nearly temperature independent for measurements taken at temperatures below about 15 K, which indicates that the QD PL emission is caused only by the direct excitation of the QD by absorption due to the laser illumination. For temperatures between 15 K and 30 K, an increase in the PL intensity is observed. This is associated to exciton diffusion from the barrier material into the QD, contributing to the overall intensity. At about 30 K, the depth of the QD layer from the surface and the diffusion length are expected to be equal and a saturation point is reached at which no further excitons diffuse into the QD by further increasing the diffusion length. As the temperature exceeds 30 K, the intensity

decreases and, at room temperature, the intensity is four orders of magnitude less than the intensities for low temperature measurements.

To investigate the cause of the intensity loss above 30 K, a rate model, which assumes thermally activated loss channels, is used. The activation energies are fitted for two regimes (low and high temperatures). From the analysis, the intensity loss at temperatures below 100 K can be associated with thermally activated dissociation of excitons formed in the AlGaAs barrier by laser excitation. This would cause the formation of single electrons and holes which diffuse through the crystal separately. The dissociated excitons are more prone to non-radiative recombinations and thus the QD PL emission vanishes. Using a different pumping mechanism, such as electrical injection or resonant or quasi-resonant pumping into the QD, would avoid the exciton dissociation.

The intensity loss above 160 K is suggested to be caused by bound excitons escaping from the QD ground state into the AlGaAs barrier. It should be noted that, with increasing temperature, non-radiative recombination by Auger type processes also increase. Nonetheless, these processes are expected to be strong only at very high excitation densities [147], which is assumed not to be the case in the measurements performed in this work. To improve the PL emission in the high-temperature regime, it is advisable to increase the Al concentration of the AlGaAs barrier to raise the barrier height. It is shown that using the maximum Al content of 40%, allowed for having a direct band gap, the QD PL intensity at room temperature T_R increases by more than three orders of magnitude.

An inexpensive Peltier element can be used to moderately reduce the temperature by thermoelectric cooling and it is shown that this leads already to a considerable improvement of the QD PL emission. The GaAs emission linewidth becomes sharper, consequently reducing the background that obscures the QD emission. Furthermore, the thermal escape of excitons from the QD ground state is reduced, hence yielding a stronger QD emission.

The rest of the thesis focuses on the optical properties of the cone-shell QDs at low temperature. The influence of an external electric field F, applied in the growth direction on cone-shell QDs, is discussed in ch. 6. These nanostructures, for their exceptional geometry, are of particular interest because a large control via an electric field is expected despite the tight confinement, which is not the case for symmetric QDs [121–124], where a tight confinement leads to a small Stark-shift. Simulations using a model in effective mass approximation predict that an electric field induces a distinct charge carrier separation in the cone-shell QDs. Through the separation of electrons and holes, it is possible to form quantum rings with either one of the two charge carriers, whilst the other remains as a

QD. As opposed to existing self-assembled quantum rings, in the cone-shell structure the confinement as a quantum ring is not static and can be tuned by the gate voltage. A further important prediction deriving from the strong spatial separation of the charge carriers, and the consequently strong Stark-shift, is the elongation of the recombination lifetime up to milliseconds. The long lifetimes suggest the possible application of cone-shell QDs for information storage in the field of quantum technology.

Samples with different QD sizes are also examined experimentally. As expected, the Stark-shift is observed to increase with increasing QD size in the field direction. Furthermore, the change in exciton energy for positive electric fields F is stronger than the energy variation for negative F, which is in qualitative agreement with the simulations and is caused by the different effective masses of the charge carriers, together with the potential asymmetry in the growth direction. The QD PL intensity is also studied through field dependent PL measurements taken at different excitation powers. The expected relative behaviour of the X and XX peak as function of the laser power is observed. An unexpected outcome of the measurements as function of the electric field F is a sudden power-independent drop in the emission intensity and the presence of additional emission lines at high positive fields. It is speculated that this behaviour is caused by the sudden separation of charge carriers or by the injection of charge carriers into the QDs after the onset of leakage current and the consequent formation of charged excitons and other excitonic complexes.

The experimental Stark-shift data obtained with several simulation models are compared. The first model, widely used in this thesis, is based on effective mass approximation in rotational symmetry and includes Coulomb interaction. This model allows a very precise meshing of the QD shape and a very fast computation. The second model, which is also based on effective mass approximation and includes Coulomb interaction, uses a fully 3D geometry [98]. However, for the size of the structures studied here, limitations of the available computer memory yield an only rough meshing, which neglects details of the structures. The third model is an atomistic model, which includes Coulomb and exchange interaction, as well as configuration interaction (CI). The simulations with the atomistic model are performed by Geoffrey Pirard and Gabriel Bester. Since this model requires very long computation times, only a few simulation results are presented and are used mainly for comparison purpose. As a first step, the shape and size of the simulated QD is modified to reproduce more precisely the experimental Stark-shift results. The so obtained new structural parameters, when used for the atomistic model, lead to an almost perfect agreement with the experimental data. When used for the models with effective mass approximation,

an overestimation of the exciton energies, particularly at positive fields, is observed. This effect is stronger for the rotational-symmetric model. Further analysis of the models suggests that the assumption of rotational symmetry, the effective mass approximation and neglecting CI, in order of importance, all contribute to the overestimation of the energy. However, recent and on-going editing of the rotational symmetric model, for example changing the hole effective mass, are leading to promising results in good agreement with the more sophisticated models. Thus, the simple model used in this thesis, with further appropriate editing, could still give good predictions. Besides the work on the theoretical side, as a next step for the experimental investigation, lifetime measurements in an electric field are highly desirable to test the strong lifetime elongation predicted by the simple model as well as by more complex models, including the atomistic one.

Electric field dependent measurements are also performed with a sample, grown by Hans-Georg Babin and the author, embedded in a diode structure featuring a DBR, which increases the photon collection efficiency. This sample is shown to be charge tunable via Coulomb blockade. An analogous sample is used in the literature [134], where optical linewidths close to lifetime-limited and blinking-free single photon emission are achieved. The present sample is an improvement of the one used in the literature, as further work was done by Babin to improve the QD size uniformity as well as their symmetry and to optimise the material composition. Hence, further studies on this sample are suggested and, in particular, for an estimation of the linewidth, resonant excitation is advisable for creating low-noise photons. Thanks to the improvements performed in the sample, the expected narrow linewidth should be reproducible for a large number of QDs. Lifetime measurements under pulsed resonant excitation, as well as auto-correlation ($g^{(2)}$) measurements are also recommended. For their properties, these QDs are predicted to be excellent sources of low-noise single photons with wavelength coinciding with the rubidium D_2 wavelengths (780 nm) and could be used for the development of hybrid QD-rubidium quantum memories [134, 148].

The predicted formation of quantum rings in the cone-shell structures by means of an electric field, makes these structures interesting also for magnetic field dependent measurements. The influence of a magnetic field B applied in the growth direction, combined with an electric field F, is investigated through simulations in ch. 7. The main findings can be summarised as follows. Applying a magnetic field causes a switch of the magnetic quantum number l associated to the lowest energy state and the overall effect of the magnetic field B is to push the charge carriers closer to each other, counteracting the effect of the electric field F, although the direction in which the carriers are pushed is not the same. The effect

of the magnetic field is more evident for holes than for electrons due to the larger effective mass. Considering thus the case in which the holes are pushed to the sides of the cone-shell and the electrons stay at the tip (i.e. when positive electric fields are applied), two regimes are distinguished, one for high $F \geq 10.5\,\mathrm{kV/cm}$ and one for low positive $F < 10.5\,\mathrm{kV/cm}$. In the former regime, the hole wavefunction forms a well defined ring and luminescence is expected only for low magnetic fields B, because the electron stays in the $l_e = 0$ state while the hole ground state goes from $l_h = 0$ to higher l_h as the magnetic field increases. In the low positive electric field regime, a hybrid system between a QD and a quantum ring is expected. In this regime, it is predicted that a recurrence of the luminescence can be observed as a consequence of the hole ground state l_h dropping back to 0, thus satisfying the selection rule $l_h = l_e$. The recurrence can be precisely controlled by tuning electric and magnetic fields. This suggests cone-shell QDs for applications as quantum memory.

As excitonic AB oscillations are currently a major research interest [101, 137, 140, 141, 143, 146], it is interesting that the simulation results presented here predict the possibility of observing clear oscillations in the X ground state energy, with the strongest oscillations observed for $F = 12\,\mathrm{kV/cm}$, and, to observe the first oscillation, only less than 1 T is needed. These results are very promising but it is essential to take into account the above mentioned selection rules when considering the possibility of observing the oscillations experimentally. Furthermore, in light of the discussion on the simulation model precision reported in ch. 6, it is also important to note that the inclusion of CI may cause a reduction of the predicted excitonic AB oscillations. Hence, further improvement of the simple model used here is needed and, if possible, an atomistic model should be employed in order to get more reliable results, without assuming the simple mass approximation.

It is also absolutely necessary to test the predictions experimentally. For this, a collaboration was initiated with the group of P. Koenraad, in the University of Eindhoven. It would be of great interest to bring this collaboration forward and perform electric and magnetic field dependent measurements. Since the magnetic field is expected to strongly affect the exciton recombination lifetime, lifetime measurements are also strongly recommended.

Besides the already mentioned improvements to the simulation model and the suggested experiments, further advice is here briefly given to avoid issues encountered in this work and to optimise the results of future studies.

In the development of the simulation model, the initial approach for the determination of the QD size and shape was a combination of AFM images taken at different growth stages. As discussed in ch. 6, the structural parameters obtained in this way lead to theoretical

results that are in disagreement with the experiments, even when reliable theoretical models, like the atomistic model, are used. Hence, it is advisable to use an imaging technique that allows taking images after the entire growth process is concluded, such as transmission electron microscopy (TEM), cross-sectional scanning tunnelling microscopy (X-STM) or atom probe tomography (APT). If this is not possible, AFM images should be taken for a larger number of filled and unfilled nanoholes to have a better statistic of the morphological parameters and hence a combined AFM image that is a more realistic representation of the QDs in the considered sample.

The bonding process for the metal contacts discussed in app. A was particularly challenging for the AuGe back gates, due to sticking issues. On the contrary, when NiAuGe was used, the gates could be bonded easily. Hence, it is recommended to deposit the back gates with NiAuGe in 3 steps, one layer of AuGe, followed by Ni and a third layer of AuGe. Furthermore, it was observed that larger back gates give better wire adhesion and thus an editing in the mask design is also advisable. Care should also be taken to avoid mechanical stress during the bonding process, as they can lead to leakage current.

Moreover, during the gate fabrication, some samples underwent an HCl dip. This step was added to remove any surface oxide between the semiconductor and the metal layer, which could alter the Schottky contact [130]. However, no major improvement was observed in the experiments for the sample with HCl dip. Hence, this step needs to be either changed by, for example, extending the time in which the sample is immersed in the HCl, or fully removed, in order to reduce the number of fabrication processes and thus the chances of having further contaminants in the sample.

For the fabrication of new samples, the implementation of a DBR could be considered, as this was shown to lead to an increase in the PL emission intensity. Also, in the sample with the DBR it is possible to clearly distinguish charged excitonic complexes. In samples analogous to this, charge tuning is reported up to eight time negatively charged excitons [134]. The ultra-low charge noise is achieved by embedding the QDs in a n-i-p diode and hence this structure can also be tried as an alternative to the QDs being between a p-doped back gate and a metal top gate.

In conclusion, this thesis gives an overview of the optical properties of LDE QDs, and in particular it showed some promising features of cone-shell QDs under an electric and magnetic field. Major points are a shift of either hole or electron wavefunction from dot to ring, a strong elongation of the recombination lifetime and the possibility of switching on and off the QD luminescence by tuning the externally applied fields. The results and

understanding gained can be used as a ground for future experiments as well as theoretical investigations in the field of semiconductor quantum dots for applications in quantum information technology and for fundamental research.

Appendix A

Sample fabrication technical details

A general outline of the main characteristics of the samples studied in this thesis is given in ch. 4. In this appendix, more detailed technical details of the sample fabrication are presented for each sample.

Sample #1 (single layer of low density QDs in thin AlGaAs, nanoholes filled with 4 pulses, fig. 4.1a). The MBE growth includes the following steps. The surface oxide is removed by heating the wafer at 600 °C and an AlAs/GaAs superlattisce (SL) is grown to remove unwanted impurities from the surface and to make the surface smoother. A layer of $Al_{0.33}Ga_{0.77}As$ of thickness 50 nm is then deposited, followed by 100 nm of GaAs and 50 nm of n^+-doped (Si)GaAs layer, which acts as back contact layer for field dependent measurements[1]. After a subsequent growth of 120 nm of $Al_{0.33}Ga_{0.77}As$, the As valve is closed and 1 ML of Al is deposited at 600 °C and an AlAs flux of 0.4 ML/s. This process provides Al droplets with a density of $2 \times 10^7\,cm^{-2}$. During a post-growth annealing step of 180 s at 620 °C, these droplets transform into self-assembled nanoholes surrounded by AlAs walls. The holes are filled with GaAs with 4 pulses of 0.5 s each, with 10 s waiting time between each pulse, and every pulse represents the deposition of 0.11 ML of GaAs. The QDs are made optically active by capping with a layer of $Al_{0.33}Ga_{0.77}As$ (80 nm).

Sample #2 (single layer of high density QDs in AlAs/AlGaAs, nanoholes filled with 5 pulses; fig. 4.1b). Following the growth of a GaAs buffer layer, 50 nm of $Al_{0.37}Ga_{0.63}As$ are grown, followed by 100 nm of GaAs, 200 nm of $Al_{0.37}Ga_{0.63}As$ and 5 nm of AlAs. With the As valve closed, Al is deposited for 6 s at a flux of 0.47 ML/s at 650 °C. As a consequence of the AlAs layer and the etching parameters, a relatively high droplet density of $4 \times 10^8\,cm^{-2}$ is obtained. The nanoholes are then filled with GaAs in 5 pulses, with the same flux, duration and pause as for sample #1. A capping layer of $Al_{0.37}Ga_{0.63}As$ (120 nm) is then deposited.

[1] Despite having a back contact layer, sample #1 is not contacted and is not used for field-dependent measurements.

The steps from the growth of the AlAs layer to the nanohole filling is repeated for AFM analysis.

Sample #3 (stack of 5 layers of high-density QDs in AlAs/AlGaAs, with thick AlGaAs, nanoholes filled with 5 pulses; fig. 4.1c). After the growth of the GaAs buffer layer, a thick (1.3 µm) $Al_{0.31}Ga_{0.69}As$ layer is deposited, followed by 5 nm of AlAs. With the As valve closed, Al droplets are deposited with the same parameters as for sample #2, obtaining nanoholes with the same density. With a Ga flux of 0.88 ML/s, the nanoholes are filled with GaAs in 5 pulses of 0.5 s with a break of 10 s between each pulse, as for the previous samples. The surface is then covered by 20 nm of $Al_{0.23}Ga_{0.77}As$. The growth sequence, from the deposition of the AlAs layer to the capping of the QDs, is repeated 5 times, hence obtaining 5 layers of high-density QDs separated by 20 nm of $Al_{0.23}Ga_{0.77}As$. A final layer of AlGaAs (60 nm of $Al_{0.23}Ga_{0.77}As$ followed by 1.3 µm of $Al_{0.58}Ga_{0.42}As$) is then deposited.

Sample #4 (single layer of low density QDs in AlGaAs, nanoholes filled with 2 pulses; fig. 4.1d). The sample is grown with the same procedure and parameters as for sample #1. The only differences are that the AlAs/GaAs SL on the GaAs substrate is absent and that the nanoholes are filled with 2 pulses of GaAs instead of 4. Furthermore, metal top gates and back gate pads are grown on top of the sample for field-dependent measurements, with the procedure explained in sec. A.0.1.

Sample #5 (single layer of low density QDs in AlGaAs, nanoholes filled with 2.5 pulses; fig. 4.1e). After the growth of a GaAs buffer layer, 150 nm of $Al_{0.30}Ga_{0.70}As$ are grown, followed by 50 nm of GaAs and 100 nm of (Si)GaAs. An $Al_{0.30}Ga_{0.70}As$ spacer layer of thickness 120 nm is then grown. Following this, the LDE process is performed with 1.05 ML of Al deposited at 600 °C at an Al flux of 0.34 ML/s. The post-growth annealing takes place at 620 °C in 180 s. The so obtained nanoholes are filled with 2 pulses of 0.5 s each, with 10 s waiting time in between and 1 pulse of 0.75 s, for a total of 2.5 pulses of GaAs. A final 80 nm $Al_{0.30}Ga_{0.70}As$ capping layer is then deposited. Metal top gates and back gate pads are grown on top of the sample for field-dependent measurements, with the procedure explained in sec. A.0.1.

Sample #6 (single layer of low density QDs in AlGaAs, nanoholes filled with 4 pulses; fig. 4.1e). The sample is grown with the same procedure and parameters as for sample #5. The only difference is the number of pulses, which is 4 instead of 2.5.

Sample #7 (single layer of low density QDs in AlGaAs, nanoholes filled with 6 pulses; fig. 4.1d). The sample is grown with the same procedure and parameters as for sample #4.

The only difference is the number of pulses, which is 6 instead of 2.

Sample #8 (p-i-n sample with distributed Bragg reflector (DBR), single layer of low density QDs in AlGaAs; fig. 4.1f). Firstly, a 100 nm buffer layer of GaAs is grown on the GaAs substrate, to have a smoother surface. This is followed by a short period SL of GaAs/AlAs (2.8 nm/2.8 nm repeated 22 times), the DBR, made by repeating 10 times the deposition of 67.08 nm of AlAs and 59.54 nm of $Al_{0.33}Ga_{0.67}As$ and then a buffer layer of $Al_{0.30}Ga_{0.70}As$. An n^+ doped back gate (150 nm of Si doped $Al_{0.15}Ga_{0.85}As$), with doping concentration of about $2 \times 10^{18}\,cm^{-3}$, is grown, followed by the tunnel barrier. The tunnel barrier consists of 3 layers: firstly 5 nm of $Al_{0.15}Ga_{0.85}As$ grown at lower $T = 590\,°C$, then 15 nm of $Al_{0.15}Ga_{0.85}As$ grown at $T = 610\,°C$ and lastly 10 nm of $Al_{0.33}Ga_{0.67}As$ grown at $T = 566\,°C$. Nanoholes are then etched with the LDE method by depositing 1.1 ML Al droplets and etching for 2 min at 545 °C, thus obtaining nanoholes with a density of $3.7 \times 10^7\,cm^{-2}$. The nanoholes are filled with GaAs in pulsed mode. A blocking barrier consisting of 273.6 nm $Al_{0.33}Ga_{0.67}As$ is grown over the filled nanoholes. Lastly, a p-doped epitaxial gate is grown. This is composed of 65 nm (C)$Al_{0.15}Ga_{0.85}As$ with a carbon doping concentration of $2 \times 10^{18}\,cm^{-3}$ and 10 nm with a concentration of $8 \times 10^{18}\,cm^{-3}$ followed by 5 nm (C)GaAs, also with a carbon concentration of $8 \times 10^{18}\,cm^{-3}$.

A.0.1 Gate preparation and contacting

Samples #4 to #8 are contacted for electric field dependent measurements, as illustrated also in fig. 4.1. Before preparing the gates, a layer of photoresist (PR) is spin coated on the wafers and the wafers are cleaved. AZ 1518 resist is used but any other PR would be suitable, as its purpose is to protect the wafer and avoid contamination during cleaving. Next, the cleaved sample pieces are cleaned in acetone and isopropanol, removing the PR and any debris on it. The electrodes are then prepared with the following steps, which apply for samples #4 to #7.

Back contact pads. For contacting the n^+-doped back contact layer, first about 1.8 µm of AZ 1518 PR is deposited on the sample pieces (4000 rpm/s for 40 s, with 1000 rpm/s acceleration). The samples are then soft-baked at 100 °C to reduce the solvent concentration and they then undergo a lithography step using a mask aligner (Karl Süss MJB3). The back gate mask used for the exposure is shown in fig. 4.2a, top. The samples are then placed in a bath of undiluted AZ 726 MIF developer for 1 minute to remove the exposed PR, rinsed in deionised (DI) water, dried and hard-baked at 115 °C for 50 s.

After the lithography, the next step is the metal evaporation, where 80 nm of AuGe (88:12,

99.999% purity) are thermally evaporated through physical vapour deposition (PVD, Balzers Pfeiffer PLS 500). The unexposed PR, is stripped-off (along with the metal layer deposited on it) through a low-power ultrasonic bath in acetone for about 1 minute. The AuGe is then diffused into the back contact layer in an annealing oven with an Ar-rich atmosphere at 370 °C for about 170 seconds, of which 60 seconds are of ramping from room temperature. The resistance between two back contact pads is measured, where a maximum of a few kΩ would be considered acceptable. If the resistance exceeds this range, the annealing is repeated to obtain a good contact between the pads and the back contact. The final resistance values obtained for samples #4, #5, #6 and #7 are 268 Ω, 200 Ω, 230 Ω and 300 Ω.

Titanium window. The Ti window mask pattern (fig. 4.2a, middle) is transferred to a PR layer through a procedure analogous to the one used for the back contact. Samples #4 and #7, following the development of the PR, are dipped in HCl 32% for 10 and 12 seconds respectively, to remove the surface oxide between the semiconductor and the metal layer, which would otherwise alter the Schottky barrier. Since in the mask design the back gate pads are used for alignment, these are not protected by PR, hence it is important for the HCl to be diluted to at least 50% and for the dipping time to be short, in order not to damage the AuGe metal pads. The oxide layer removal step by HCl is blocked by DI water and the samples are then dried.
Following either the lithography step or the HCl dip, a 10 nm layer of Ti (99.995% purity) is deposited by PVD. The unexposed PR and the unwanted Ti lying on it are stripped-off in acetone and ultrasonic bath, as done for the back contact pads.

Gold frame. With the same method and parameters used for the back contact pads and the Ti windows, the Au frame mask pattern (fig. 4.2a, bottom) is transferred to a PR layer by photolithography. Following the PR development, the Au could be deposited. However, due to sticking issues of the Au on the Ti, a thin 8 nm layer of Cr (99.99% purity) is first deposited through the Au mask and, on this layer, 30 nm of Au (99.999% purity) are then deposited. The deposition of both Cr and Au is done by PVD as a single step. The lift-off process to remove the undesired metal is done in acetone and ultrasonic bath, as for the AuGe and Ti layers. Two examples of the resulting sample surface with gates are shown in fig. 4.2b and c.

Wiring. Once the gates are prepared, they are contacted to the chip carrier's pins via Au wires of thickness 25 µm. The wires are bonded by using the wedge bonder (Giessen Electronics bonder, with Leica Stereo Zoom4 microcope), which is equipped with a heatable

stage. Each chip carrier has 16 contacts and can carry two samples. Generally, 3 or 4 top contact pads are contacted. Due to the poor adhesion of the annealed AuGe, only one back contact pad is connected per sample, which is enough as all the back contacts are annealed into the same back gate layer. The force at which the wedge hits the sample, the ultrasonic power applied to the wedge and the sample temperature are regulated for each sample and can vary from back to top gate, due to the different materials. An example of a sample with contacted gates is shown in fig. 4.2b, where one back gate and two top gate wires are visible. It is important to avoid mechanical stress in the bonding procedure, which can cause damages in the crystal and and lead to leakage current[2]. A way to avoid mechanical stress is to use silver print or metal bridges over etched trenches that separate the back contact from the bond pads. One back gate of sample #7 is contacted with silver print whilst all the other gates for all the sample are contacted with the above described bonding process.

The p-i-n sample #8 is contacted with a different procedure compared to samples #4 - #7. In brief, the main steps are the following.
To contact the back gate layer, firstly the back gate mask is transferred to a PR layer by photolithography. The sample areas uncovered by the PR are then etched down by about 360 nm in H_2SO_4: 30% H_2O_2: H_2O = 1: 1: 50, so that the C doped epitaxial layer is locally removed. NiAuGe is then deposited by e-beam evaporation in 3 steps, 60 nm of AuGe (88:12), 10 nm Ni and 60 nm AuGe. Following the lift-off, the NiAuGe is annealed for 370 °C for 60 s and at 420 °C for 30 s to reach the (Si)$Al_{0.15}Ga_{0.85}As$ layer.
For contacting the C doped epitaxial layer (p-type top gate), the top gate mask is firstly transferred to a PR layer by lithography. On the uncovered areas of the surface, 3 nm of Ti followed by 7 nm of Au are evaporated through e-beam PVD. The unwanted material over the PR is then lifted-off. The resulting gates are shown in the microscopy image in fig. 4.2d. The back and top contact pads are then contacted with the wedge bonder using Au wires, in the same way as for the other samples.

[2]From private discussion with Arne Ludwig, Bochum.

Bibliography

[1] Z. Huang, M. Zimmer, S. Hepp, M. Jetter, and P. Michler, "Optical gain and lasing properties of InP/AlGaInP quantum-dot laser diode emitting at 660 nm," *IEEE J. Quantum Electron.*, vol. 55, p. 2000307, 2019.

[2] A. Martí, E. Antolín, C. R. Stanley, C. D. Farmer, N. López, P. Díaz, E. Cánovas, P. G. Linares, and A. Luque, "Production of photocurrent due to intermediate-to-conduction-band transitions: a demonstration of a key operating principle of the intermediate-band solar cell," *Phys. Rev. Lett.*, vol. 97, p. 247701, 2006.

[3] D. Zhou, G. Sharma, S. F. Thomassen, T. W. Reenaas, and B. O. Fimland, "Optimization towards high density quantum dots for intermediate band solar cells grown by molecular beam epitaxy," *Appl. Phys. Lett.*, vol. 96, p. 061913, 2010.

[4] M. Grudmann, *Nano-optoelectronics*. Berlin: Springer, 2002.

[5] A. Imamoglu and Y. Yamamoto, "Turnstile device for heralded single photons: Coulomb blockade of electron and hole tunneling in quantum confined p-i-n heterojunctions," *Phys. Rev. Lett.*, vol. 72, no. 2, p. 210, 1994.

[6] E. Knill, R. laflamme, and G. J. Milburn, "A scheme for efficient quantum computation with linear optics," *Nature*, vol. 409, p. 46, 2001.

[7] O. Benson, C. Santori, M. Pelton, and Y. Yamamoto, "Regulated and entangled photons from a single quantum dot," *Phys. Rev. Lett.*, vol. 84, p. 2513, 2000.

[8] C. Schimpf, S. Manna, S. F. C. da Silva, M. Aigner, and A. Rastelli, "Entanglement-based quantum key distribution with a blinking-free quantum dot operated at a temperature up to 20 k," *Adv. Photonics*, vol. 3, no. 6, p. 065001, 2021.

[9] P. Michler, A. Kiraz, C. Becher, W. V. Schoenfeld, P. M. Petroff, L. Zhang, E. Hu, and A. Imamoglu, "A quantum dot single-photon turnstile device," *Science*, vol. 290, p. 2282, 2000.

[10] C. Santori, M. Pelton, G. Solomon, Y. Dale, and Y. Yamamoto, "Triggered single photons from a quantum dot," *Phys. Rev. Lett.*, vol. 86, p. 1502, 2001.

[11] A. I. Ekimov, A. L. Efros, and A. A. Onushchenko, "Quantum size effect in semiconductor microcrystals," *Solid State Commun.*, vol. 56, pp. 921–924, 1985.

[12] L. E. Brus, "Electron–electron and electronhole interactions in small semiconductor crystallites: the size dependence of the lowest excited electronic state," *J. Chem. Phys.*, vol. 80, p. 4403, 1984.

[13] M. A. Reed, J. N. Randall, R. J. Aggarwal, R. J. Matyi, T. M. Moore, and A. E. Wetsel, "Observation of discrete electronic states in a zero-dimensional semiconductor nanostructure," *Phys. Rev. Lett.*, vol. 60, p. 535, 1988.

[14] J. S. Lee, "Growth of self-organized quantum dots," in *Semiconductor quantum dots: physics, spectroscopy and applications* (Y. Masumoto and T. Takagahara, eds.), vol. 1, pp. 1–55, Berlin: Springer Berlin Heidelberg, 2nd ed., 2010.

[15] H. Drexler, D. Leonard, W. Hansen, J. P. Kotthaus, and P. M. Petroff, "Spectroscopy of quantum levels in charge-tunable InGaAs quantum dots," *Phys. Rev. Lett.*, vol. 73, pp. 2252–2256, 1994.

[16] J. Y. Marzin, J. M. Gerard, A. Izrael, and D. Barrier, "Photoluminescence of single InAs quantum dots obtained by self-organized growth on GaAs," *Phys. Rev. Lett.*, vol. 73, pp. 716–719, 1994.

[17] H. F. Hess, E. Betzig, T. D. Harris, L. N. Pfeiffer, and K. W. West, "Near-field spectroscopy of the quantum constituents of a luminescent system," *Science*, vol. 264, p. 1740, 1994.

[18] D. Gammon, E. S. Snow, B. V. Shanabrook, D. S. Katzer, and D. Park, "Homogeneous linewidths in the optical spectrum of a single gallium arsenide quantum dot," *Science*, vol. 273, pp. 87–90, 1996.

[19] A. Zrenner, L. Y. Butov, M. Hagn, G. Abstreiter, G. Bohm, and G. Weimann, "Quantum dots formed by interface fluctuations in AlAs/GaAs coupled quantum well structures," *Phys. Rev. Lett.*, vol. 72, pp. 3382–3385, 1994.

[20] A. Zrenner, "A close look on single quantum dots," *J. Chem. Phys.*, vol. 112, pp. 7790–7798, 2000.

[21] G. Chen, N. H. Bonadeo, D. G. Steel, D. Gammon, D. S. Katzer, D. Park, and L. J. Sham, "Optically induced entanglement of excitons in a single quantum dot," *Science*, vol. 289, p. 1906, 2000.

[22] A. Rastelli, S. M. Ulrichb, E. M. Pavelescuc, T. Leinonenc, M. Pessac, P. Michler, and O. G. Schmidta, "Self-assembled quantum dots for single-dot optical investigations," *Superlattices Microstruct.*, vol. 36, pp. 181–191, 2004.

[23] M. Baier, F. Findeis, A. Zrenner, M. Bichler, and G. Abstreiter, "Optical spectroscopy of charged excitons in single quantum dot photodiodes," *Phys. Rev. B*, vol. 64, p. 195326, 2001.

[24] E. F. Duijs, F. Findeis, A. Zrenner, M. Bichler, and G. Abstreiter, "Photoluminescence and AFM studies on blue shifted InAs/$Al_yGa_{1-y}As$ quantum dots," *Phys. Stat. Sol.*, vol. 224, pp. 47–51, 2001.

[25] D. Leonard, S. Fafard, Y. H. Zhang, J. L. Merz, and P. M. Petroff, "Structural and optical properties of self-assembled InGaAs quantum dots," *J. Vac. Sci. Technol. B*, vol. 12, p. 2516, 1994.

[26] D. Leonard, M. Krishnamurthy, S. Fafard, J. L. Merz, and P. M. Petroff, "Molecular-beam epitaxy growth of quantum dots from strained coherent uniform islands of InGaAs on GaAs," *J. Vac. Sci. Technol. B*, vol. 12, p. 1063, 1994.

[27] J. M. Moison, F. Houzay, F. Barthe, L. Leprince, E. Andre, and O. Vatel, "Self-organized growth of regular nanometer-scale InAs dots on GaAs," *Appl. Phys. Lett.*, vol. 64, p. 196, 1994.

[28] A. Madhukar, Q. Xie, P. Chen, and A. Konkar, "Nature of strained InAs three-dimensional island formation and distribution on GaAs(100)," *Appl. Phys. Lett.*, vol. 64, p. 2727, 1994.

[29] V. Bressler-Hill, S. Varma, A. Lorke, B. Z. nosho, P. M. Petroff, and W. H. Weinberg, "Island scaling in strained heteroepitaxy: InAs/GaAs(001)," *Phys. Rev. Lett.*, vol. 74, p. 3209, 1995.

[30] F. T. Pedersen, Y. Wang, C. T. Olesen, S. Scholz, A. D. Wieck, A. Ludwig, M. C. Löbl, R. J. Warburton, L. Midolo, R. Uppu, and P. Lodahl, "Near transform-limited quantum dot linewidths in a broadband photonic crystal waveguide," *ACS Photonics*, vol. 7, no. 9, p. 2343, 2020.

[31] R. Uppu, F. T. Pedersen, Y. Wang, C. T. Olesen, C. Papon, X. Zhou, L. Midolo, S. Scholz, A. D. Wieck, A. Ludwig, and P. Lodahl, "Scalable integrated single-photon source," *Sci. Adv.*, vol. 6, p. eabc8268, 2020.

[32] R. Uppu, L. Midolo, X. Zhou, J. Carolan, and P. Lodahl, "Quantum-dot-based deterministic photon–emitter interfaces for scalable photonic quantum technology," *Nat. Nanotechnol.*, vol. 16, p. 1308, 2021.

[33] C. Schneider, S. Höfling, and A. Forchel, "Growth of III–V semiconductor quantum dots," in *Quantum dots: optics, electron transport and future applications* (A. I. Tartakovskii, ed.), pp. 3–20, Cambridge Univ. Press, 2012.

[34] S. Sanguinetti, M. Gurioli, E. Grilli, M. Guzzi, and M. Heninib, "Piezoelectric effects in InAs/GaAs(N11) self-assembled quantum dots," *Thin Solid Films*, vol. 380, pp. 198–200, 2000.

[35] G. Costantini, A. Rastelli, C. Manzano, R. Songmuang, O. G. Schmidt, K. Kern, and H. von Känel, "Universal shapes of self-organized semiconductor quantum dots: Striking similarities between InAs/GaAs(001) and Ge/Si(001)," *Appl. Phys. Lett.*, vol. 85, pp. 5673–5675, 2004.

[36] D. Leonard, M. Krishnamurthy, C. M. Reaves, S. P. Denbaars, and P. M. Petroff, "Direct formation of quantumsized dots from uniform coherent islands of InGaAs on GaAs surfaces," *Appl. Phys. Lett.*, vol. 63, pp. 3203–3205, 1993.

[37] A. Rastelli, M. Stoffel, A. Malachias, T. Merdzhanova, G. Katsaros, K. Kern, T. H. Metzger, and O. G. Schmidt, "Three-dimensional composition profiles of single quantum dots determined by scanning-probe-microscopy-based nanotomography," *Nano Lett.*, vol. 8, pp. 1404–1409, 2008.

[38] C. Heyn, A. Stemmann, and W. Hansen, "Self-assembly of quantum dots and rings on semiconductor surfaces," in *Quantum materials, lateral semiconductor nanostructures, hybrid systems and nanocrystals* (D. Heitmann, ed.), vol. 1, pp. 1–24, Berlin: Springer Berlin Heidelberg, 1st ed., 2010.

[39] C. Heyn, A. Bolz, T. Maltezopoulos, R. L. Johnson, and W. Hansen, "Intermixing in self-assembled InAs quantum dot formation," *J. Cryst. Growth*, vol. 278, pp. 46–50, 2005.

[40] M. Gurioli, Z. Wang, A. Rastelli, T. Kuroda, and S. Sanguinetti, "Droplet epitaxy of semiconductor nanostructures for quantum photonic devices," *Nat. mater.*, vol. 18, pp. 799–810, 2019.

[41] K. Watanabe, N. Koguchi, and Y. Gotoh, "Fabrication of GaAs quantum dots by modified droplet epitaxy," *Jpn. J. Appl. Phys.*, vol. 39, pp. L79–L81, 2000.

[42] K. Reyes, P. Smereka, D. Nothern, J. M. Millunchick, S. Bietti, C. Somaschini, S. Sanguinetti, and C. Frigeri, "Unified model of droplet epitaxy for compound semiconductor nanostructures: experiments and theory," *Phys. Rev B*, vol. 87, p. 165406, 2013.

[43] S. Bietti, C. Somaschini, and S. Sanguinetti, "Crystallization kinetics of Ga metallic nano-droplets under As flux," *Nanotechnology*, vol. 24, p. 205603, 2013.

[44] S. Sanguinetti, K. Watanabe, T. Tatenob, M. Gurioli, P. Werner, M. Wakaki, and N. Koguchi, "Modified droplet epitaxy GaAs/AlGaAs quantum dots grown on a variable thickness wetting layer," *J. Cryst. Growth*, vol. 253, pp. 71–76, 2003.

[45] S. Bietti, J. Bocquel, S. Adorno, T. Mano, J. G. Keizer, P. M. Koenraad, and S. Sanguinetti, "Precise shape engineering of epitaxial quantum dots by growth kinetics," *Phys. Rev. B*, vol. 92, p. 075425, 2015.

[46] N. Koguchi, S. Takhashi, and T. Chikyow, "New MBE growth method for InSb quantum well boxes," *J. Christ. Growth*, vol. 111, p. 688, 1991.

[47] T. Mano, K. Watanabe, S. Tsukamoto, H. Fujioka, M. Oshima, and N. Koguchi, "New self-organized growth method for InGaAs quantum dots on GaAs(001) using droplet epitaxy," *Jpn. J. Appl. Phys.*, vol. 38, pp. L1009–L1011, 1999.

[48] C. Somaschini, S. Bietti, N. Koguchi, F. Montalenti, C. Frigeri, and S. Sanguinetti, "Self-assembled GaAs islands on Si by droplet epitaxy," *Appl. Phys. Lett.*, vol. 97, p. 053101, 2010.

[49] T. Kawazu, T. Mano, T. Noda, and H. Sakaki, "Optical properties of GaSb/GaAs type-II quantum dots grown by droplet epitaxy," *Appl. Phys. Lett.*, vol. 94, p. 081911, 2009.

[50] T. Schupp, T. Meisch, B. Neuschl, M. Feneberg, K. Thonke, K. Lischka, and D. J. As, "Droplet epitaxy of zinc-blende GaN quantum dots," *J. Cryst. Growth*, vol. 312, pp. 3235–3237, 2010.

[51] V. Mantovani, S. Sanguinetti, M. Guzzi, E. Grilli, M. Gurioli, K. Watanabe, and N. Koguchi, "Low density GaAs/AlGaAs quantum dots grown by modified droplet epitaxy," *J. Appl. Phys.*, vol. 96, pp. 4416–4420, 2004.

[52] T. Mano, M. Abbarchi, T. Kuroda, C. A. Mastrandrea, A. Vinattieri, S. Sanguinetti, K. Sakoda, and M. Gurioli, "Ultra-narrow emission from single GaAs self-assembled quantum dots grown by droplet epitaxy," *Nanotechnology*, vol. 20, p. 395601, 2009.

[53] Z. M. Wang, K. Holmes, Y. I. Mazur, K. A. Ramsey, and G. J. Salamo, "Self-organization of quantum-dot pairs by high-temperature droplet epitaxy," *Nanoscale Res Lett.*, vol. 1, pp. 57–61, 2006.

[54] Z. M. Wang, B. L. Liang, K. A. Sablon, and G. J. Salamo, "Nanoholes fabricated by self-assembled gallium nanodrill on GaAs(100)," *Appl. Phys. Lett.*, vol. 90, p. 113120, 2007.

[55] C. Heyn, A. Stemmann, and W. Hansen, "Dynamics of self-assembled droplet etching," *Appl. Phys. Lett.*, vol. 95, p. 1731101, 2009.

[56] C. Heyn, T. Bartsch, S. Sanguinetti, D. E. Jesson, and W. Hansen, "Dynamics of mass transport during nanohole drilling by local droplet etching," *Nanoscale Res. Lett.*, vol. 10, p. 67, 2015.

[57] X. Li, J. Wu, Z. M. Wang, B. Liang, J. Lee, E. Kime, and G. J. Salamo, "Origin of nanohole formation by etching based on droplet epitaxy," *Nanoscale*, vol. 6, pp. 2675–81, 2014.

[58] C. Schimpf, M. Reindl, D. Huber, B. Lehner, S. F. C. D. Silva, S. Manna, M. Vyvlecka, P. Walther, and A. Rastelli, "Quantum cryptography with highly entangled photons from semiconductor quantum dots," *Sci. Adv.*, vol. 7, no. 16, p. 8905, 2021.

[59] M. Pfeiffer, K. Lindfors, H. Zhang, B. Fenk, F. Phillipp, P. Atkinson, A. Rastelli, O. G. Schmidt, H. Giessend, and M. Lippitz, "Eleven nanometer alignment precision of a plasmonic nanoantenna with a self-assembled GaAs quantum dot," *Nano Lett.*, vol. 14, pp. 197–201, 2014.

[60] P. Nikhil, "Molecular beam epitaxy," 2013.

[61] F. C. Frank and J. H. van der Merwe, "One-dimensional dislocations, static theory.," *Proc. R. Soc. A*, vol. 198, p. 205, 1949.

[62] A. Pimpinelli and J. Villain, *Physics of Crystal Growth.* Cambridge: Cambridge University Press, 1998.

[63] M. Volmer and A. Weber, "Nucleus formation in supersaturated systems," *Z. Phys. Chem.*, vol. 119, p. 277, 1926.

[64] I. N. Stranski and L. K. Sitzungsber, "Zur theorie der orientierten ausscheidung von ionenkristallen aufeinander," *Akad. Wiss. Wien. Math.- Naturwiss.*, vol. 146, no. 797, p. 810, 1938.

[65] M. Souaf, M. Baira, O. Nasr, M. H. H. Alouane, H. Maaref, L. Sfaxi, and B. Ilahi, "Investigation of the InAs/GaAs quantum dots' size: Dependence on the strain reducing layer's position," *Materials*, vol. 8, p. 4699, 2015.

[66] A. Stemmann, C. Heyn, T. Köppen, T. Kipp, and W. Hansen, "Local droplet etching of nanoholes and rings on GaAs and AlGaAs surfaces," *Appl. Phys. Lett.*, vol. 93, p. 123108, 2008.

[67] C. Heyn, A. Stemmann, and W. Hansen, "Nanohole formation on algaas surfaces by local droplet etching with gallium," *J. Cryst. Growth*, vol. 311, pp. 1839–1842, 2009.

[68] C. Heyn, A. Stemmann, T. Köppen, C. Strelow, T. Kipp, M. Grave, S. Mendach, and W. Hansen, "Highly uniform and strain-free GaAs quantum dots fabricated by filling of self-assembled nanoholes," *Appl. Phys. Lett.*, vol. 94, p. 183113, 2009.

[69] C. Heyn, A. Stemmann, R. Eiselt, and W. Hansen, "Influence of ga coverage and as pressure on local droplet etching of nanoholes and quantum rings," *J. Appl. Phys.*, vol. 105, p. 054316, 2009.

[70] A. Stemmann, C. Heyn, and W. Hansen, "Local etching of nanoholes and quantum rings with In_xGa_{1-x} droplets," *J. Appl. Phys.*, vol. 106, p. 064315, 2009.

[71] C. Heyn, A. Stemmann, A. Schramm, H. Welsch, and W. Hansen, "Regimes of GaAs quantum dot self-assembly by droplet epitaxy," *Phys. Rev. B*, vol. 76, p. 075317, 2007.

[72] C. Heyn, M. Zocher, S. Schnüll, and W. Hansen, "Role of arsenic during aluminium droplet etching of nanoholes in AlGaAs," *Nanoscale Res. Lett.*, vol. 11, p. 428, 2016.

[73] C. Heyn, M. Zocher, and W. Hansen, "Functionalization of droplet etching for quantum rings," in *Physics of Quantum Rings* (V. Fomin, ed.), Springer, Cham, 2018.

[74] D. Fuster, Y. Gonzalez, and L. Gonzalez, "Fundamental role of arsenic flux in nanohole formation by Ga droplet etching on GaAs(001)," *Nanoscale Res. Lett*, vol. 9, p. 309, 2014.

[75] C. Heyn, S. Schnüll, and W. Hansen, "Scaling of the structural characteristics of nanoholes created by local droplet etching," *J. Appl. Phys.*, vol. 115, p. 024309, 2014.

[76] C. Heyn, A. Küster, M. Zocher, and W. Hansen, "Field-controlled quantum dot to ring transformation in wave-function tunable cone-shell quantum structures," *Phys. Status Solid RRL*, vol. 13, p. 1800245, 2018.

[77] A. Nemcsics, C. Heyn, L. Toth, L. Dobos, A. Stemmann, and W. Hansen, "Cross-sectional transmission electron microscopy of GaAs quantum dots fabricated by filling of droplet-etched nanoholes," *J. Cryst. Growth*, vol. 335, pp. 58–61, 2011.

[78] C. Heyn, M. Zocher, A. Küster, and W. Hansen, "Droplet etching during semiconductor epitaxy for single and coupled quantum structures," in *Quantum dots and nanostructures: growth, characterization, and modeling XV* (D. L. Huffaker and H. Eisele, eds.), p. 105430K, SPIE, 2018.

[79] G. Bastard, *Wave mechanics applied to semiconductor heterostructures*. Les Ulis Cedex, France: Wiley-Interscience, 1991.

[80] R. Seguin, A. Schliwa, S. Rodt, K. Pötschke, U. W. Pohl, and D. Bimberg, "Size-dependent fine-structure splitting in self-organized InAs/GaAs quantum dots," *Phys. Rev. Lett.*, vol. 95, p. 257402, 2005.

[81] P. Michler, *Single semiconductor quantum dots*. Berlin: Springer, 2009.

[82] H. Fu, L. Wang, and A. Zunger, "Excitonic exchange splitting in bulk semiconductors," *Phys Rev B*, vol. 59, no. 8, p. 5568, 1998.

[83] A. Schliwa, *Electronic properties of self-organized quantum dots*. PhD thesis, Technische Universität Berlin, 2007.

[84] M. Bayer, G. Ortner, O. Stern, A. Kuther, A. A. Gorbunov, and A. Forchel, "Fine structure of neutral and charged excitons in self-assembled In(Ga)As/(Al)GaAs quantum dots," *Phys. Rev. B*, vol. 65, p. 195315, 2002.

[85] D. Gammon, E. S. Snow, B. V. Shanabrook, D. S. Katzer, and D. Park, "Fine structure splitting in the optical spectra of single GaAs quantum dots," *Phys. Rev. Lett.*, vol. 76, no. 16, p. 3005, 1996.

[86] V. D. Kulakovskii, G. Bacher, R. Weigand, T. Kuṁmell, A. Forchel, E. Borovitskaya, K. Leonardi, and D. Hommel, "Fine structure of biexciton emission in symmetric and asymmetric CdSe/ZnSe single quantum dots," *Phys. Rev. Lett.*, vol. 82, p. 1780, 1999.

[87] A. Kuther, M. Bayer, A. Forchel, A. Gorbunov, V. B. Timofeev, F. Schäfer, and J. P. Reithmaier, "Zeeman splitting of excitons and biexcitons in single $In_{0.60}Ga_{0.40}As$/GaAs self-assembled quantum dots," *Phys. Rev. B*, vol. 58, p. R7508(R), 1998.

[88] L. Besombes, K. Kheng, and D. Martrou, "Exciton and biexciton fine structure in single elongated islands grown on a vicinal surface," *Phys. Rev. Lett.*, vol. 85, p. 425, 2000.

[89] C. Heyn, C. Strelow, and W. Hansen, "Excitonic lifetimes in single GaAs quantum dots fabricated by local droplet etching," *New J. Phys.*, vol. 14, p. 053004, 2012.

[90] A. Graf, D. Sonnenberg, V. Paulava, A. Schliwa, C. Heyn, and W. Hansen, "Excitonic states in GaAs quantum dots fabricated by local droplet etching," *Phys. Rev. B*, vol. 89, p. 155314, 2014.

[91] M. Fox, *Optical properties of solids.* Oxford: Oxford University Press, 2001.

[92] Y. P. Varshni, "Temperature dependence of the energy gap in semiconductors," *Physica*, vol. 34, p. 149, 1967.

[93] S. A. Lourenco, I. F. L. Dias, J. L. Duarte, and E. Laureto, "Temperature dependence of optical transitions in AlGaAs," *J. Appl. Phys.*, vol. 89, no. 11, p. 6159, 2001.

[94] M. Benyoucef, A. Rastelli, O. G. Schmidt, S. M. Ulrich, and P. Michler, "Temperature dependent optical properties of single, hierarchically self-assembled GaAs/AlGaAs quantum dots," *Nanoscale Res. Lett.*, vol. 1, p. 172, 2006.

[95] L. Besombes and K. Kheng, "Acoustic phonon broadening mechanism in single quantum dot emission," *Phys. Rev. B*, vol. 63, p. 155307, 2001.

[96] K. Matsuda, K. Ikeda, and T. Saiki, "Homogeneous linewidth broadening in a $In_{0.5}Ga_{0.5}As$/GaAs single quantum dot at room temperature investigated using a highly sensitive near-field scanning optical microscope," *Phys. Rev. B*, vol. 63, p. 121304, 2001.

[97] S. Moehl, F. Tinjod, K. Kheng, and H. Mariette, "Reduction of exciton-phonon interaction due to stronger confinement in single quantum dots," *Phys. Rev. B*, vol. 69, p. 245318, 2004.

[98] C. Heyn, L. Ranasinghe, M. Zocher, and W. Hansen, "Shape-dependent Stark shift and emission-line broadening of quantum dots and rings," *J. Phys. Chem. C*, vol. 124, no. 36, pp. 19809–19816, 2020.

[99] S. A. Empedocles and M. G. Bawendi, "Quantum-confined Stark effect in single CdSe nanocrystallite quantum dots," *Science*, vol. 278, p. 2114, 1997.

[100] V. Fock, "Bemerkung zur quantelung des harmonischen oszillators im magnetfeld," *Z. Phys.*, vol. 47, p. 446, 1928.

[101] A. V. Chaplik, "Aharonov–Bohm effect for composite particles and collective excitations," *JETP Letters*, vol. 75, no. 6, p. 292, 2002.

[102] C. Heyn, "Design and operation of a portable micro-photoluminescence spectrometer for education on semiconductor quantum structures and graphene sheets," *Rev. Sci. Instrum.*, vol. 92, p. 053905, 2021.

[103] T. Skauli, P. S. Kuo, K. L. Vodopyanov, T. J. Pinguet, O. Levi, L. A. Eyres, J. S. Harris, M. M. Fejer, B. Gerard, L. Becouarn, and E. Lallier., "Improved dispersion relations for GaAs and applications to nonlinear optics," *J. Appl. Phys.*, vol. 94, p. 6447, 2003.

[104] P. A. Dalgarno, J. M. Smith, J. McFarlane, B. D. Gerardot, K. Karrai, A. Badolato, P. M. Petroff, and R. J. Warburton, "Coulomb interactions in single charged self-assembled quantum dots: radiative lifetime and recombination energy," *Phys. Rev. B*, vol. 77, p. 245311, 2008.

[105] S. Adachi, *Properties of semiconductor alloys: group-IV, III-V and II-VI semiconductor*. Southampton, UK: John Wiley and Sons, 2009.

[106] A. Küster, C. Heyn, A. Ungeheuer, G. Juska, S. T. Moroni, E. Pelucchi, and W. Hansen, "Droplet etching of deep nanoholes for filling with self-aligned complex quantum structures," *Nanoscale Res. Lett.*, vol. 11, p. 282, 2016.

[107] E. Grilli, M. Guzzi, R. Zamboni, and L. Pavesi, "High-precision determination of the temperature dependence of the fundamental energy gap in gallium arsenide," *Phys. Rev. B*, vol. 45, p. 1638, 1992.

[108] L. Pavesi and M. Guzzi, "Photoluminescence of $Al_xGa_{1-x}As$ alloys," *J. Appl. Phys.*, vol. 75, p. 4779, 1994.

[109] J. H. Lambert, "Bestimmung der Absorption des rothen Lichts in farbigen Flüssigkeiten," *Annalen der Physik und Chemie*, vol. 162, no. 5, p. 78, 1852.

[110] D. S. Jiang, H. Jung, and K. Ploog, "Temperature dependence of photoluminescence from GaAs single and multiple quantum-well heterostructures grown by molecular-beam epitaxy," *J. Appl. Phys.*, vol. 64, p. 1371, 1988.

[111] C. Heyn, A. Stemmann, T. Köppen, C. Strelow, T. Kipp, M. Grave, S. Mendach, and W. Hansen, "Optical properties of GaAs quantum dots fabricated by filling of self-assembled nanoholes," *Nanoscale Res. Lett.*, vol. 5, pp. 576–580, 2010.

[112] Y. Weidong, R. L. W. Roger, L. Hao, and C. S. Peter, "Effect of carrier emission and retrapping on luminescence time decays in InAs/GaAs quantum dots," *Phys. Rev. B*, vol. 56, no. 20, p. 13314, 1997.

[113] P. Michler, A. Hangleiter, M. Moser, M. Geiger, and F. Scholz, "Influence of barrier height on carrier lifetime in $Ga_{1-y}In_yP/(Al_xGa_{1-x})_{1-y}In_yP$ single quantum wells," *Phys. Rev. B*, vol. 46, p. 7280, 1992.

[114] D. E. Aspnes, S. M. Kelso, R. A. Logan, and R. Bhat, "Optical properties of $Al_xGa_{1-x}As$," *J. Appl. Phys.*, vol. 60, p. 754, 1986.

[115] S. S. Li and J. B. Xia, "Quantum-confined Stark effects of InAs/GaAs self-assembled quantum dot," *J. Appl. Phys.*, vol. 88, p. 7171, 2000.

[116] P. W. Fry, I. E. Itskevich, D. J. Mowbray, M. S. Skolnick, J. J. Finley, J. A. Barker, E. P. O'Reilly, L. R. Wilson, I. A. Larkin, P. A. Maksym, M. Hopkinson, M. Al-Khafaji, J. P. R. David, A. G. Cullis, G. Hill, and J. C. Clark, "Inverted electron-hole alignment in InAs-GaAs self-assembled quantum dots," *Phys. Rev. Lett.*, vol. 84, p. 733, 2000.

[117] J. J. Finley, M. Sabathil, P. Vogl, G. Abstreiter, R. Oulton, A. I. Tartakovskii, D. J. Mowbray, M. S. Skolnick, S. L. Liew, A. G. Cullis, and M. Hopkinson, "Quantum-confined Stark shifts of charged exciton complexes in quantum dots," *Phys. Rev. B*, vol. 70, p. 201308(R), 2004.

[118] J. A. Osorio, D. Caicedo-Paredes, J. A. Vinasco, A. L. Morales, A. Radu, R. L. Restrepo, J. C. Martínez-Orozco, A. Tiutiunnyk, D. Laroze, N. N. Hieu, H. V. Phuc,

M. E. Mora-Ramos, and C. A. Duque, "Pyramidal core-shell quantum dot under applied electric and magnetic fields," *Sci. Rep.*, no. 10, p. 8961, 2020.

[119] G. J. Vázquez, M. Castillo-Mussot, C. I. Mendoza, and H. N. Spector, "Spherical quantum dot under an electric field," *Phys. Stat. Sol.*, vol. 1, p. 54, 2004.

[120] D. A. B. Miller, D. S. Chemla, T. C. Damen, A. C. Gossard, W. Wiegmann, T. H. Wood, and C. A. Burrus, "Band-edge electroabsorption in quantum well structures: the quantum-confined Stark effect," *Phys. Rev. Lett.*, vol. 53, p. 2173, 1984.

[121] K. Hasanirokh, A. Asgari, and S. Mohammadi, "Fabrication of a light-emitting device based on the CdS/ZnS spherical quantum dots," *J. Eur. Opt. Soc: Rapid Publ.*, vol. 17, no. 26, p. 1, 2021.

[122] Z. Marvia, T. J. M. Donders, M. Hasani, G. Klaassen, and J. Beckers, "Quantum dot photoluminescence as a versatile probe to visualize the interaction between plasma and nanoparticles on a surface," *Appl. Phys. Lett.*, vol. 119, p. 254104, 2021.

[123] E. Marino, D. M. Balazs, R. W. Crisp, D. H. M. Merino, M. A. Loi, T. E. Kodger, and P. Schall, "Simultaneous photonic and excitonic coupling in spherical quantum dot supercrystals," *ACS Nano*, vol. 14, no. 10, p. 13806, 2020.

[124] V. M. Fomin, V. N. Gladilin, J. T. Devreese, E. P. Pokatilov, S. N. Balaban, and S. N. Klimin, "Photoluminescence of spherical quantum dots," *Phys. Rev. B*, vol. 57, p. 2415, 1998.

[125] G. Snider, "Poisson-solver," https://www3.nd.edu/∼gsnider/ [Last update: 28.01.2022].

[126] J. S. Best, "The Schottky-barrier height of Au on n-$Al_xGa_{1-x}As$ as a function of AlAs content," *Appl. Phys. Lett.*, vol. 34, no. 8, p. 522, 1979.

[127] M. Missous, W. S. Truscott, and K. E. Singer, "Insitu, near-ideal epitaxial $Al/Al_xGa_{1-x}As$ Schottky barriers formed by molecular beam epitaxy," *J. Appl. Phys.*, vol. 68, no. 5, p. 2239, 1990.

[128] K. Okamoto, C. E. C. Wood, and L. F. Eastman, "Schottky barrier heights of molecular beam epitaxial metal AlGaAs structures," *Appl. Phys. Lett.*, vol. 38, no. 8, p. 636, 1981.

[129] M. Eizenberg, M. Heiblum, M. I. Nathan, N. Braslau, and P. M. Mooney, "Barrier heights and electrical properties of intimate metal-AlGaAs junctions," *J. Appl. Phys.*, vol. 61, no. 4, p. 1516, 1987.

[130] A. Küster, *Photoluminescence of nanostructures in droplet-etched nanoholes.* PhD thesis, Universität Hamburg, Fakultät für Mathematik, Informatik und Naturwissenschaften, 2017.

[131] G. Myburg, F. D. Auret, W. E. Meyer, and C. W. L. M. J. van Staden, "Summary of Schottky barrier height data on epitaxially grown n- and p-GaAs," *Thin Solid Films*, vol. 325, p. 181, 1998.

[132] M. Abbarchi, C. Mastrandrea, T. Kuroda, T. Mano, and A. Vinattieri, "Poissonian statistics of excitonic complexes in quantum dots," *J. Appl. Phys.*, vol. 106, p. 053504, 2009.

[133] A. J. Bennett, R. B. Patel, J. Skiba-Szymanska, C. A. Nicoll, I. Farrer, D. A. Ritchie, and A. J. Shields, "Giant Stark effect in the emission of single semiconductor quantum dots," *Appl. Phys. Lett.*, vol. 97, p. 31104, 2010.

[134] L. Zhai, M. C. Löbl, G. N. Nguyen, J. Ritzmann, A. Javadi, C. Spinnler, A. D. Wieck, A. Ludwig, and R. J. Warburton, "Low-noise GaAs quantum dots for quantum photonics," *Nat. Commun.*, vol. 11, p. 4745, 2020.

[135] R. J. Warburton, C. Schäflein, D. Haft, F. Bickel, A. Lorke, K. Karrai, J. M. Garcia, W. Schoenfeld, and P. M. Petroff, "Optical emission from a charge-tunable quantum ring," *Nature*, vol. 405, p. 226, 2000.

[136] Y. Aharonov and D. Bohm, "Significance of electromagnetic potentials in the quantum theory," *Phys. Rev.*, vol. 115, p. 485, 1959.

[137] V. M. Fomin, *Physics of quantum rings.* Dresden: Springer, 2018.

[138] T. Ihn, A. Fuhrer, L. Meier, M. Sigrist, and K. Ensslin, "Quantum physics in quantum rings," *Europhysics news*, vol. 36, p. 78, 2005.

[139] S. L. Ren, J. J. Heremans, C. K. Gaspe, S. Vijeyaragunathan, T. D. Mishima, and M. B. Santos, "Aharonov-Bohm oscillations, quantum decoherence and amplitude modulation in mesoscopic InGaAs/InAlAs rings," *Condens. Matter*, vol. 25, p. 435301, 2013.

[140] I. R. Sellers, V. R. Whiteside, I. L. Kuskovsky, A. O. Govorov, and B. D. McCombe, "Aharonov-Bohm excitons at elevated temperatures in type-II ZnTe/ZnSe quantum dots," *Phys. Rev. Lett.*, vol. 100, p. 136405, 2008.

[141] N. A. J. M. Kleemans, J. H. Blockland, A. G. Taboada, H. C. M. van Genuchten, M. Bozkurt, V. M. Fomin, V. N. Gladilin, D. Granados, J. M. Garcia, P. C. M. Christianen, J. C. Maan, J. T. Devreese, and P. M. Koenraad, "Excitonic behaviour in self-assembled InAs/GaAs quantum rings in high magnetic fields," *Phys. Rev. B*, vol. 80, p. 155318, 2009.

[142] V. M. Fomin, V. N. Gladilin, and J. T. Devreese, "Energy spectra and oscillatory magnetization of two-electron self-assembled $In_xGa_{1-x}As$ quantum rings in GaAs," *Phys. Rev. B*, vol. 77, p. 205326, 2008.

[143] A. M. Fischer, V. L. C. Jr, M. E. Portnoi, and R. A. Römer, "Exciton storage in a nanoscale Aharonov-Bohm ring with electric field tuning," *Phys. Rev. Lett.*, vol. 102, p. 096405, 2009.

[144] N. A. J. M. Kleemans, I. M. A. Bominaar-Silkens, V. M. Fomin, V. N. Gladilin, D. Granados, A. G. Taboada, J. M. Garcia, P. Offermans, U. Zeitler, P. C. M. Christianen, J. C. Maan, J. T. Devreese, and P. M. Koenraad, "Oscillatory persistent currents in self-assembled quantum rings," *Phys. Rev. Lett.*, vol. 99, p. 146808, 2007.

[145] V. M. Fomin, V. N. Gladilin, S. N. Klimin, and J. T. Devreese, "Theory of electron energy spectrum and Aharonov-Bohm effect in self-assembled $In_xGa_{1-x}As$ quantum rings in GaAs," *Phys. Rev. B*, vol. 76, p. 235320, 2007.

[146] B. Li and F. M. Peeters, "Tunable optical Aharonov-Bohm effect in a semiconductor quantum ring," *Phys. Rev. B*, vol. 83, p. 115448, 2011.

[147] I. Y. Solov'ev and G. G. Zegrya, "Nonradiative recombination in quantum dots via Coulomb interaction with carriers in the barrier region," *Appl. Phys. Lett.*, vol. 82, p. 2571, 2003.

[148] J. Wolters, G. Buser, A. Horsley, L. Béguin, A. Jöckel, J. Jahn, R. J. Warburton, and P. Treutlein, "Simple atomic quantum memory suitable for semiconductor quantum dot single photons," *Phys. Rev. Lett.*, vol. 119, p. 060502, 2017.

Appendix B

List of acronyms

AB Aharonov-Bohm

AFM atomic force microscope

CI configuration interaction

DE droplet epitaxy

DI deionised

DBR distributed Bragg reflector

EMCCD electron multiplying charged coupled device

FD Fock-Darwin

FEM finite element method

FSS fine structure splitting

LDE local droplet etching

MBE molecular beam epitaxy

ML mono-layer

ND neutral density

PL photoluminescence

PR photoresist

PVD physical vapour deposition

QD quantum dot

QW quantum well

RHEED reflection high-energy electron diffraction

SK Stranski-Krastanov

SL superlattice

TEM transmission electron microscopy

T_R room temperature

UHV ultra-high-vacuum

WL wetting layer

X exciton

XX biexciton

Acknowledgements

I would like to thank Prof. Dr. Wolfgang Hansen for giving me the opportunity of joining his group and for the excellent supervision and constant availability to clarify my doubts and to give advice. I thank him for the constructive feedback, stimulating and inspiring discussions and for always giving value and consideration to ideas of those who are less experienced and expert. He gave me the best example of how physics research should be performed and how a group leader should be.

I thank Dr. Christian Heyn also for the great supervision and for the extensive explanations and enormous support given. The knowledge he shared, his passion for the field and the willingness to clarify for me topics time and time again, have been invaluable. I thank him for the constant optimism and his certainty in great results, which gave me motivation and enthusiasm and led our progresses and the exploration of very interesting physics. Also, thanks for the many Python codes and for the countless research ideas.

I am also thankful to my former and current colleagues, Michael Zocher, Ahmed Alshaikh, Kristian Deneke, Stefan Feddersen, Roman Korneev, Katrin Groth, Sandra Schnüll and Birgit Stelljes, for all the help, knowledge sharing, technical support, interesting conversations and fun time. Each of them has in different ways contributed to the realisation of this thesis. Being part of this group has been a great pleasure.

I also wish to thank the 4Photon network members and collaborators, in particular, Sergio Bietti, Alexey Fedorov, Shiro Tsukamoto, Andreas Fognini, Paul Koenraad, Arne Ludwig, Hans-Georg Babin, Gabriel Bester, Sandrine Soubes and my fellow PhD students in the ITN, in particular Geoffrey Pirard, for the helpful discussions and insights, the fruitful collaborations, the creative ideas and for making conferences and secondments very enjoyable.

Thanks also to the financial supporters; this research has received financial support from Deutsche Forschungsgemeinschaft via HE 2466/2-1 and HA 2042/8-1, from the European Union's Horizon 2020 Research and Innovation Programme under the Marie Skłodowska-Curie grant agreement No. 721394 (4PHOTON) and from BMBF Forschungslabor Mikroelektronik Deutschland "ForLab".

My thanks also go to all my friends and my girlfriend for making my stay in Hamburg such an amazing experience, full of meaningful and pleasant moments, and for making me truly feel at home. Also, thanks for supporting me during challenges and cheering with me for my accomplishments.

The biggest thanks go to my family: my dad, my mum, and my brother. Throughout the years, they have always been there for me, supporting me and encouraging me. They advised me during difficult times and shared my happiness for my successes; they have always believed in me and they gave everything they could for me to be where I am now. Thank you.